

Simultaneous Multi-Spectral Imaging System: Application in Real-Time, Unsupervised Spectral Classification in Endometrial Endoscopy

Vassilis Kavvadias

Master Thesis

TECHNICAL UNIVERSITY OF CRETE

DEPT. OF ELECTRONICS AND COMPUTER ENGINEERING

Supervising committee:

Costas Balas, Associate Professor (supervisor)

Michalis Zervakis, Professor

Mattias Bucher, Assistant Professor



Chania 2013

Abstract

We report the first real-time spectral mapper based on the combination of snap-shot spectral imaging and spectral classification algorithms. High accuracy is accompanied with much faster, by 3 orders of magnitude, spectral mapping, as compared with scanning spectral systems. This new technology is intended to enable spectral mapping at nearly video rates in all kinds of dynamic bio-optical effects as well as in applications where the target-probe relative position is randomly and fast changing. With this system adapted to a thin hysteroscope for imaging of the endometrial tissue, we also report, for the first time, spectral analysis of the endometrium and unsupervised/objective clustering of the spectra. We have implemented a method combining the k-means algorithm with the silhouette criterion for estimating the number of the distinguishable spectral classes that may correspond to different medical conditions of the tissue. It was found that there are five-well defined clusters of spectra, while preliminary clinical data seem to correlate well with the tissue pathology.

Acknowledgements

This Master Thesis would not have been completed without the presence of many people to support me all the way.

First of all, I am deeply grateful to my supervising professor, Constantinos Balas, who trusted and shared his insight with me, for a revolutionary new approach in present healthcare practices. His integrous scientific guidance and vast experience in biomedical devices design, is invaluable.

I would also like to thank all my fellow students in the Optoelectronics team of Electronics and Computer Engineering Department, who have always been there for me, especially Mr. George Epitropou.

Thanks also to Dr. Minas Paschopoulos and Dr. Fani Grozou, from the Department of Obstetrics and Gynecology University Hospital, Ioannina, for their cooperation throughout the clinical evaluation of the multispectral hysteroscopic platform.

Finally, I am most indebted to my friends and companions who have supported and encouraged me in times of enthusiasm and in times of crisis.

To my beloved parents,

Damianos and Toulia

Contents

Abstract	2
Acknowledgements	3
List of Figures.....	7
List of Tables	9
Introduction	10
Chapter 1 - Electromagnetic wave theory	13
1.1 Electromagnetic radiation	13
1.2 Fluorescence – Phosphorescence.....	16
Chapter 2 – Light Tissue interaction	18
2.1 Tissue optics.....	18
2.2 Optical properties of human tissues.....	19
2.3 Propagation of continuous-wave light in tissues - Basic principles.....	19
2.4 Major absorbers and scatterers	21
2.5 Optical window in biological tissue	22
Chapter 3 – Endometrial physiology and pathology	24
3.1 Endometrial Physiology	24
3.2 Endometrial Pathology	28
Chapter 4 - Endometrial Imaging techniques	33
4.1 Classical Methods	33
4.2 Novel diagnostic Advances in Endoscopy.....	35
Chapter 5 - A Novel Endoscopic Spectral Imaging Platform Integrating K-Means Clustering for Early and non-Invasive Diagnosis of Endometrial Pathology	44
Introduction.....	44
5.1 Materials and methods.....	45
5.1.1 SPECL System Design and Set-Up	45
5.1.2 SPECL System Operation-Spectral and Color Image Acquisition	48
5.2 Clinical Evaluation.....	48
Chapter 6 – Simultaneous spectral imaging using multiple band-pass filters	54
Introduction.....	54
6.1. Hyperspectral Imaging using Multiple Band - pass Filters (MBPFs)	54
6.1.1 Capturing color information with imaging sensors	54
6.1.2 Measuring the spectral sensitivity of a color camera manually	58
6.1.3 Camera parameters – Maximizing the image quality.....	60

6.2 Multi bandpass filters combined with color cameras	65
6.2.1 Channel unmixing algorithm.....	66
6.3 Results.....	69
Chapter 7 - Clustering of Spectra Obtained from the Endometrium	75
Introduction	75
7.1 Processing workflow of endometrium spectra.....	76
Results and discussion	109
7.2 Identification of endometrial physiology and pathology with the use of multispectral hysteroscopy.....	111
7.2.1 Identification of the menstrual cycle healthy endometrium conditions.....	111
7.2.2 Identification of the AUB conditions, with the use of hyperspectral hysteroscopy.....	114
Conclusions.....	118
Discussion.....	118
References.....	120

List of Figures

<i>Figure 1 The electromagnetic waves that compose electromagnetic radiation can be imagined as a self-propagating transverse oscillating wave of electric and magnetic fields.....</i>	13
<i>Figure 2. Artist's impression, inspired by the work of the artist Maurits Cornelis Escher, of the continuous morphing between particle- and wave-like behaviour of light. Credit: Nicolas Brunner and Jamie Simmonds.....</i>	14
<i>Figure 3 Electromagnetic spectrum with visible light highlighted.....</i>	15
<i>Figure 4. Jablonski diagram. Energy levels and the possible pathways following light absorption by an absorbing molecule (chromophore).....</i>	16
<i>Figure 5. Stimulated emission. The electron in the excited state falls into the lower state emitting a photon.....</i>	17
<i>Figure 6. Light tissue interaction mechanisms.....</i>	18
<i>Figure 7. Major organelles and inclusions of the cell.....</i>	20
<i>Figure 8. Absorption spectrum of major tissue chromophores.....</i>	21
<i>Figure 9. Absorption spectra of some important chromophores in human skin tissue, as function of wavelength. Adapted from Ref [18].</i>	23
<i>Figure 10. The uterus. Cutaway views show regions of the uterus and cervix and its relationship to the uterine (fallopian) tubes and vagina.</i>	24
<i>Figure 11. Anatomy of the female reproductive system. The organs in the female reproductive system include the uterus, ovaries, fallopian tubes, cervix, and vagina. The uterus has a muscular outer layer called the myometrium and an inner lining called the endometrium.....</i>	25
<i>Figure 12. Endometrial polyp seen in a saline infusion sonohysterogram [45]......</i>	33
<i>Figure 13. Groosy thickened endometrium detected by transvaginal sonography of the uterus [46].</i>	34
<i>Figure 14. MRI depiction of endometrial hyperplasia. (A) Axial and (B) sagittal T2-weighted images of the uterus show cystic thickening of the endometrial canal (arrows) in a patient on tamoxifen for breast cancer [47].</i>	34
<i>Figure 15. View of a submucous fibroid by hysteroscopy.</i>	35
<i>Figure 16. A, Colonoscopic view of hyperplastic polyp. B, Colonoscopic view of adenomatous polyp. In both cases tissue was stained with 0.9% indigo carmine by [48].</i>	37
<i>Figure 17. image of colon polyps. Upper left is white light image. Upper right is AFI pseudo color image. Both right is the green channel reflectance image and bottom left the fluorescence image.</i>	38
<i>Figure 18. NBI image acquisition process (left) and NBI optical filter properties (right bottom).</i>	39
<i>Figure 19. Irregular mucosa with high-grade neoplasia in a patient with long-standing ulcerative colitis. A, viewed with white light endoscopy and B, by NBI, revealing a Kudo type IV pit pattern.</i>	40
<i>Figure 20. Early gastric cancer as seen with white light (left) and with FICE (right).</i>	41
<i>Figure 21. Esophageal cancer as captured with an i-Scan system. A, the conventional white light image. B, SE + CE modes enabled captured image. C, TE mode captured image.</i>	42
<i>Figure 22. Tubular adenoma with low grade intraepithelial neoplasia (A) Analysis of a colonic polyp with white-light endoscopy, (B) chromoendoscopy, (C, D) fluorescein-based confocal endomicroscopy in different imaging depths and (E) final histology. Chromoendoscopy highlights surface architecture with tubular staining pattern. Endomicroscopy of the surface shows characteristic tubular cellular and tissue architecture (C, blue arrow). At a depth of around 150 μm, subepithelial capillaries become visible (D, red arrow). Final histology (E) confirms the presence of tubular adenoma (blue arrow) with low-grade intraepithelial neoplasia (red arrow).</i>	43
<i>Figure 23. VOF's transmission spectrum.....</i>	46
<i>Figure 24 The block diagram of the spectral clustering endoscope.....</i>	47

Figure 25. Spectral and Color images acquired from the endometrium. Numbers at the bottom right of the images represent the central wavelength. Clinical Image: endometrial polyp.	49
Figure 26. Spectral and Color images acquired from the endometrium. Numbers at the bottom right of the images represent the central wavelength. Clinical Image: Endometritis.	49
Figure 27. Spectral and Color images acquired from the endometrium. Numbers at the bottom right of the images represent the central wavelength. In Clinical image: hyperplastic tissue.	50
Figure 28. Color (left) and Spectral Image @ 675nm (right)	50
Figure 29. Color (left) and Spectral Image @ 575nm (right)	51
Figure 30. Color (left) and Spectral Image @ 575nm (right)	51
Figure 31. Color (left) and Spectral Image @ 550nm (right)	52
Figure 32. Color (left) and Spectral Image @700nm (right)	52
Figure 33Figure 5.8. Color (left) and Spectral Image @470nm (right)	53
Figure 48.a: The Bayer color filter mosaic. Each two-by-two submosaic contains 2 green, 1 blue and 1 red filter, each covering one pixel sensor, placed on a square grid. 6.1.b: Each color microfilter transmits specific spectral bands.	55
Figure 49. Relative spectral response of a Sony, ICX445 CCD imaging sensor. A Bayer CFA is used.	56
Figure 50. Relative spectral response of a Sony, ICX419 CCD imaging sensor. A CMYG CFA is used.	56
Figure 51. Sample output optical signals from a tunable diffraction grating monochromator, measured with a spectrometer.	59
Figure 52. Sample output optical signals from a tunable diffraction grating monochromator, captured with a digital camera.	59
Figure 53. Experimentally measured spectral sensitivity of a Sony ICX204AK CCD sensor for RGB channels respectively. Camera settings were set at the default values.	60
Figure 54. IR cut-off filter. edmund optics ltd, www.edmundoptics.eu	60
Figure 55. White balance operation by adjusting the light source's intensity level to a low level (a) and gradually increasing it and by adjusting the light source's intensity level to a high level (b) and gradually decreasing it. Notice that in second case, RGB values are not affected by the variations of the light source's intensities.	63
Figure 56. Indicative illumination spectra of a halogen lamp (a), a white light led (b) and a xenon lamp (c).	64
Figure 57. Modified spectral sensitivity of a Sony ICX204AK CCD sensor by the white balance operation. The illuminating source was a halogen lamp.	65
Figure 58. Transmission spectra for products FF01 422/503/572 (a) and FF01 464/542/639 (b), Semrock, Rochester, NY, www.semrock.com	66
Figure 59 The MacBeth colorchecker chart.	70
Figure 60. Measurements of reflectance of the checkerboard samples (asterisk) and reflectance spectra (solid curve). Each graph corresponds to a different color sample	73
Figure 61. Snapshot multispectral imaging device, capturing 6 narrow spectral bands simultaneously, at video rates. (a) Fingertips tissue inspection. (b) Lips tissue inspection.	74
Figure 34. SPECL SYSTEM DATA WORKFLOW	76
Figure 35. LEFT – UNREGISTERED / RIGHT - REGISTERED.....	83
Figure 36. Spectral and color-coded images of the endometrium. Different artificial colors correspond to different medical conditions.	110
Figure 37. Early proliferative phase. Hysteroscopic image (left)and Pseudocolor map (right).	112
Figure 38 . Late proliferative phase. Left column: Hysteroscopic image (left)and Pseudocolor map (right).	112
Figure 39 . Ovulatory phase. Left column Hysteroscopic image (left)and Pseudocolor map (right).	113
Figure 40 . Early secretory phase. Hysteroscopic image (left)and Pseudocolor map (right).	113

<i>Figure 41 . Late secretory phase. Hysteroscopic image (left) and Pseudocolor map (right).</i>	113
<i>Figure 42 . Nonfunctional endometrial polyp located at the left side wall. Hysteroscopic image (left) and Pseudocolor map (right).</i>	115
<i>Figure 43. Functional endometrial polyp located at the uterus fundus. Hysteroscopic image (left)and Pseudocolor map (right).</i>	115
<i>Figure 44. Submucosal fibromyoma. Hysteroscopic image (left)and Pseudocolor map (right)</i>	115
<i>Figure 45. Endometritis. Hysteroscopic image (left)and Pseudocolor map (right).</i>	116
<i>Figure 46. Complex atypical hyperplasia. Hysteroscopic image (left)and Pseudocolor map (right).</i>	116
<i>Figure 47. Endometrial adenocarcinoma. Left column Hysteroscopic image (left)and Pseudocolor map (right).</i> ..	116

List of Tables

<i>Table 1. Identifying the phase of the menstrual cycle by observing histological differences.</i>	27
<i>Table 2 List of color filter arrays.</i>	57
<i>Table 3 Basic camera setting parameters and their definitions.</i>	61
<i>Table 4. Processing times for several downsampling techniques.</i>	78
<i>Table 5. Processing times for several image registration algorithms.</i>	84
<i>Table 6. Typical execution times for several parameter sets.</i>	92
<i>Table 7. Identification of the menstrual cycle. Color sequence follows descending order of color appearance.</i> ..	114
<i>Table 8. Identification of the endometrial pathology with correlated clustering pseudocolors</i>	117
<i>Table 9. Pseudocolors correlated with particular endometrial tissue conditions</i>	117

Introduction

Spectral Imaging (SI) has the unique advantage of combining the advantages of both imaging and spectroscopy (high spatial and spectral resolution) in a single instrument. In SI, light intensity is recorded as a function of both wavelength and location. In the image domain, the data set includes a full image at each individual wavelength. In the spectroscopy domain, a fully resolved spectrum at each individual pixel can be recorded. Multiple images of the same scene at different wavelengths are acquired in time sequence for obtaining the spectra.

Unlike images taken with standard color (RGB) cameras, SI information is not discernible to the human eye. In SI, a series of images is acquired at many wavelengths, producing the so-called spectral cube. Each pixel in the spectral cube, therefore, represents the spectrum of the scene at that point. The nature of imagery data is typically multidimensional, spanning spatial and spectral dimensions (x, y, λ).

Over the last decade SI development and applications was increasingly migrating from defense domain towards prevalently civilian uses, mainly being driven by biomedical applications. SI is the first choice analytical technology for these applications due to the high heterogeneity of the biological tissues and due to the need for disentangling the spectral information from multiple, spatially and spectrally overlapping biomarkers. It should be noted however that the traditional spectral imaging cameras based on spatial or spectral scanning techniques have limited applicability in several biomedical applications.

With the today's SI technological solutions and concepts, the capturing and post-processing of the spectral cube (composed by tens of images or millions of pixel spectra) is a computational intensive and time consuming procedure. Indicatively, typical capturing and post-capturing processing times are in the range of several minutes, which restricts the applicability of SI to time invariant and stationary targets. There are several biomedical and non-biomedical applications, in which the steps of capturing, processing and of displaying the spectral patterns/classes corresponding to millions of spectra, need to be available in real-time. In endoscopy, for example, stationary imaging conditions can never be achieved due to unavoidable organ or endoscopic tip motions during the examination time. Another example referring to both in vivo and in vitro imaging is the case where the spectral or color characteristics of the target change as a result of biomarker-tissue interaction. Here, it is very

difficult to monitor the uptake kinetics separately for each biomarker because color changes are in several times occurring it times shorter than the typical scanning time of SI devices.

Another typical example relates with the need for simultaneous monitoring the uptake kinetics of multiple biomarkers, administered to the same biological sample and exhibiting different excitation/emission spectral characteristics. There are numerous other biomedical and non-biomedical applications requiring spectral imaging and analysis of transient or moving scenes such as combustion studies, imaging from aerial platforms, where scanning time needs to be very short or, in the best case, zero. This need motivates the development of “single shot” or “single exposure” spectral imagers capable of recording the information required for constructing the spectral cube without spectral or spatial scanning.

Attempts to address this need are limited to suboptimal and rather trivial approaches based mainly on image replication, filtering and image projection optics [1]. With these set-ups, the number of spectral images acquired equals to the number of imaging sensors or, alternatively, all spectral images are projected onto a single sensor. With these configurations, 4-6 images can be captured simultaneously at a reasonable spatial resolution. However, most applications dealing with complex materials require the simultaneous capturing of more than 8-10 spectral bands for enabling meaningful spectral unmixing and classification. Very recently, more advanced optoelectronic set ups have been reported, capable of capturing more than 15 spectral images [2]. The basic disadvantage of these methods is that they require significant post-processing time for reconstructing the spectral images. Another disadvantage is that the reconstructed images are of much lesser than the sensor's resolution. These drawbacks together with lack of fast, specialized and integrated platforms for data processing and analysis set serious obstacles to their clinical/laboratory implementation.

SI platforms integrating reconfigurable single exposure SI with advanced computational methods capable of providing real time spectral mapping remain still an open, demanding and high impact problem. More specifically, there is a clear and unmet need for alternative SI methods, designs and devices, allowing for the real-time calculation and live display of the thematic/diagnostic maps. The ability of displaying a diagnostic map in nearly video rates is expected to substantially advance analytical sciences and change biomedical practices. The availability of the thematic map in real time will, for example, guide medical actions, such as biopsy sampling and/or treatment, during the diagnostic scanning/interrogation of the tissue.

Chapter 1 describes the basic principles of electromagnetic wave theory, fluorescence and phosphorescence.

Chapter 2 analyzes the phenomena occurred by light - tissue interaction, including tissue optics fundamentals, optical reaction of basic chromophores and scatterers, as well as the diagnostic value of the “optical window” in visible and near-infrared tissue spectroscopy.

In **Chapter 3** the endometrial physiology and pathology is outlined, with emphasis given to histological compositional and structural changes.

In **Chapter 4**, all endometrium imaging techniques are depicted, including classical and state of the art methods.

Chapter 5 reports all steps of the development of a scanning multispectral hysteroscope, including its clinical evaluation results.

Chapter 6 presents the clustering methods used on spectra obtained from the endometrium, along with K-Means modifications, validation procedures and correlation of the extracted clusters with endometrial tissue conditions.

Chapter 7 describes explicitly a method for simultaneous spectral imaging using multiple bandpass filters using standard color digital cameras. Also, a device able of previewing 6 spectral bands in real time is presented.

Finally, the results and conclusions of this project are discussed.

Chapter 1 - Electromagnetic wave theory

1.1 Electromagnetic radiation

Electromagnetic radiation (EM radiation or EMR) is one of the fundamental phenomena of electromagnetism, behaving as waves and also as photon particles propagating through space, carrying radiant energy (figure 1). In a vacuum, it propagates at a characteristic speed, the speed of light, normally in straight lines. EMR is emitted and absorbed by charged particles. As an electromagnetic wave, it has both electric and magnetic field components, which oscillate in a fixed relationship to one another, perpendicular to each other and perpendicular to the direction of energy and wave propagation.

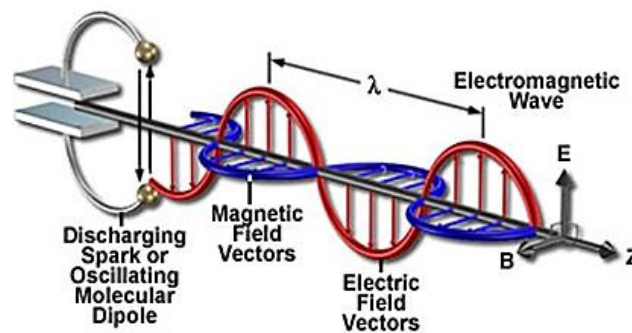


FIGURE 1 THE ELECTROMAGNETIC WAVES THAT COMPOSE ELECTROMAGNETIC RADIATION CAN BE IMAGINED AS A SELF-PROPAGATING TRANSVERSE OSCILLATING WAVE OF ELECTRIC AND MAGNETIC FIELDS.

The modern theory that explains the nature of light includes the notion of wave–particle duality (figure 2). More generally, the theory states that everything has both a particle nature and a wave nature, and various experiments can be done to bring out one or the other. The particle nature is more easily discerned if an object has a large mass, and it was not until a bold proposition by Louis de Broglie in 1924 that the scientific community realized that electrons also exhibited wave–particle duality.

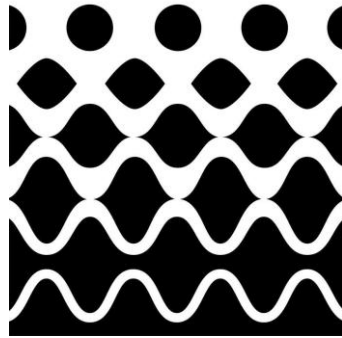


FIGURE 2. ARTIST'S IMPRESSION, INSPIRED BY THE WORK OF THE ARTIST MAURITS CORNELIS ESCHER, OF THE CONTINUOUS MORPHING BETWEEN PARTICLE- AND WAVE-LIKE BEHAVIOUR OF LIGHT. CREDIT: NICOLAS BRUNNER AND JAMIE SIMMONDS

EMR is characterized by the frequency or wavelength of its wave. The electromagnetic spectrum, in order of increasing frequency and decreasing wavelength, consists of radio waves, microwaves, infrared radiation, visible light, ultraviolet radiation, X-rays and gamma rays (figure 3). The eyes of various organisms sense a somewhat variable but relatively small range of frequencies of EMR called the visible spectrum or light. Higher frequencies correspond to proportionately more energy carried by each photon; for instance, a single gamma ray photon carries far more energy than a single photon of visible light.

Electromagnetic radiation is associated with EM fields that are free to propagate themselves without the continuing influence of the moving charges that produced them, because they have achieved sufficient distance from those charges. Thus, EMR is sometimes referred to as the far field. In this language, the near field refers to EM fields near the charges and current that directly produced them, as for example with simple magnets and static electricity phenomena. In EMR, the magnetic and electric fields are each induced by changes in the other type of field, thus propagating itself as a wave. This close relationship assures that both types of fields in EMR stand in phase and in a fixed ratio of intensity to each other, with maxima and nodes in each found at the same places in space.

Electric and magnetic fields obey the properties of superposition, so fields due to particular particles or time-varying electric or magnetic fields contribute to the fields due to other causes. (As these fields are vector fields, all magnetic and electric field vectors add together according to vector addition.) These properties cause various phenomena including refraction and diffraction. For instance, a travelling EM wave incident on an atomic structure induces oscillation in the atoms, thereby causing them to emit their own EM waves. These emissions then alter the impinging wave through interference.

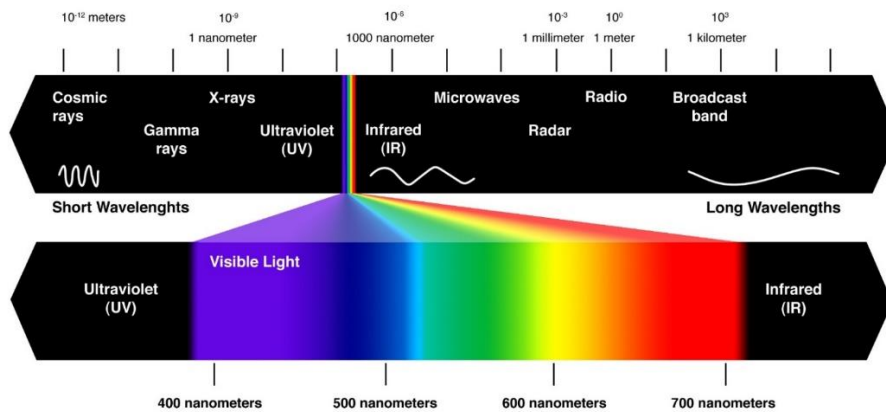


FIGURE 3 ELECTROMAGNETIC SPECTRUM WITH VISIBLE LIGHT HIGHLIGHTED

EMR carries energy—sometimes called radiant energy—through space continuously away from the source (this is not true of the near-field part of the EM field). EMR also carries both momentum and angular momentum. These properties may all be imparted to matter with which it interacts. EMR is produced from other types of energy when created, and it is converted to other types of energy when it is destroyed. The photon is the quantum of the electromagnetic interaction, and is the basic "unit" or constituent of all forms of EMR. The quantum nature of light becomes more apparent at high frequencies (thus high photon energy). Such photons behave more like particles than lower-frequency photons do.

In classical physics, EMR is considered to be produced when charged particles are accelerated by forces acting on them. Electrons are responsible for emission of most EMR because they have low mass, and therefore are easily accelerated by a variety of mechanisms. Rapidly moving electrons are most sharply accelerated when they encounter a region of force, so they are responsible for producing much of the highest frequency electromagnetic radiation observed in nature. Quantum processes can also produce EMR, such as when atomic nuclei undergo gamma decay, and processes such as neutral pion decay.

The effects of EMR upon biological systems (and also to many other chemical systems, under standard conditions) depends both upon the radiation's power and frequency. For lower frequencies of EMR up to those of visible light (i.e., radio, microwave, infrared), the damage done to cells and also to many ordinary materials under such conditions is determined mainly by heating effects, and thus by the radiation power. By contrast, for higher frequency radiations at ultraviolet frequencies and above (i.e., X-rays and gamma rays) the damage to chemical materials and living cells by EMR is far larger than that done by simple heating, due to the ability of single photons in such high frequency EMR to damage individual molecules chemically.

1.2 Fluorescence – Phosphorescence

From the microscopic point of view and according to the quantum theory, the energy levels in atoms and molecules are quantized. If the energy of the incident photon ($h\nu$) matches the gap between two energy levels in the molecule, it can be absorbed by the molecule, otherwise the molecule will be transparent to that radiation, and it will pass through. When a photon is absorbed by the molecule, the transitions between the specific energy levels can be divided into high energy electronic transitions (UV and VIS regions) and low energy vibrational or rotational transitions (NIR and IR regions) [NY 3-4]. As it is shown in Jablonski diagram, Figure 4, after the absorption of a photon and the subsequent excitation to the higher energy level ($S_0 \rightarrow S_n$), the molecule relaxes down to the lowest excited energy level; then relaxation from the lowest excited state to the ground state may happen through different processes. If the spin state of the initial and the final energy levels be the same ($S_1 \rightarrow S_0$), the relaxation is called fluorescence.

If the spin state of the initial and the final energy levels are different ($T_1 \rightarrow S_0$), the relaxation is called phosphorescence. Fluorescence and phosphorescence are radiative processes. Transitions between the same spin states are called internal conversion (IC), while such transitions between different spin states are called intersystem crossing (ISC).

Usually the stable ground state in most molecules is the singlet state (S_0 in Figure 1.4), while the triplet states ($T_1, 2$ in Figure 1.4) are unstable excited states with an increased internal energy. Oxygen is one of the rare molecules for which the lowest triplet state is the ground state. Excited molecular oxygen is in the singlet state. This is important in the photodynamical reaction occurring during photodynamic therapy (PDT) [5]. There is another type of photon-electron transition called stimulated emission, which happens in atoms.

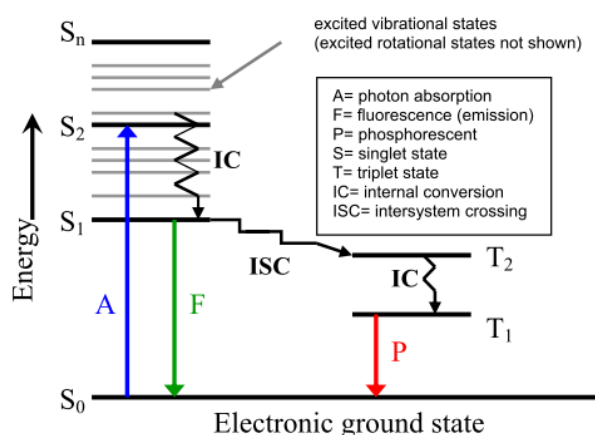


FIGURE 4. JABLONSKI DIAGRAM. ENERGY LEVELS AND THE POSSIBLE PATHWAYS FOLLOWING LIGHT ABSORPTION BY AN ABSORBING MOLECULE (CHROMOPHORE).

When an atom or molecule already is in an excited state, then an incoming photon with quantum energy equal to the excess internal energy of that atom or molecule, can produce a second photon of the same energy by stimulating the atom or molecule to fall down to its lower energy state, shown in Figure 5. This is the principle of the light amplification happens in lasers (Light Amplification by Stimulated Emission of Radiation). Photons produced by stimulated emission have the same phase and frequency, resulting in very intense and coherent light (laser).

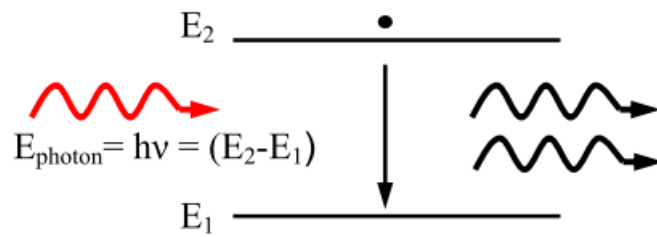


FIGURE 5. STIMULATED EMISSION. THE ELECTRON IN THE EXCITED STATE FALLS INTO THE LOWER STATE EMITTING A PHOTON.

Chapter 2 – Light Tissue interaction

2.1 Tissue optics

Once a light beam is produced and aimed at a tissue, as the energy reaches the biological interface, one of the following four interactions will occur: a) **absorption** - specific molecules in the tissue, known as chromophores, absorb the optical energy of the photons and convert it into other forms, b) **reflection** - the light beam bounces off the surface with no penetration or interaction at all, c) **transmission** - the light beam can pass through superficial tissues to interact with deeper areas, or d) **scattering** - once the light beam enters the target tissue it will scatter in various directions (figure 6).

Additionally, various interaction mechanisms between light and tissue are identified in the following major categories of interactions that lead to alterations of the tissue structure or composition: a) **Photochemical**: absorption of light by molecules present in or added to tissue (basis for Photodynamic Therapy - PDT), b) **Thermal**: biological effects due to deposition of thermal energy in tissue (basis for in laser surgery), c) **Photoablative**: in the ultra violet (UV) wavelength range photons possess sufficient energy to cause photo-dissociation of biopolymers and subsequent desorption of the fragments (basis for sterilization / purification processes) and d) **Electromechanical**: occurs at very high fluence rates where dielectric breakdown of tissue is induced which can lead to the formation of plasma. The rapid expansion of such plasma generates a shock wave which can rupture the tissue.

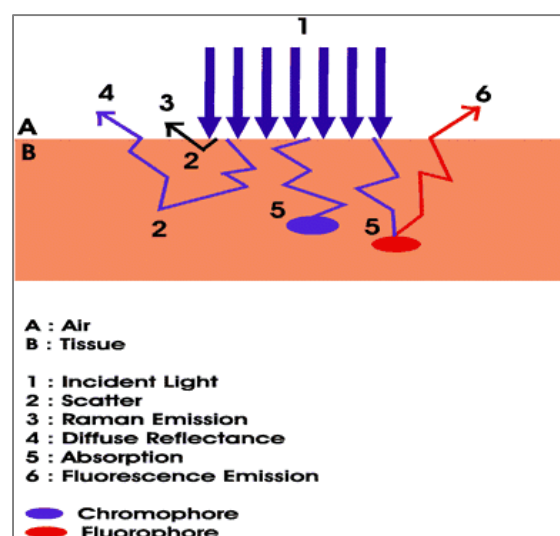


FIGURE 6. LIGHT TISSUE INTERACTION MECHANISMS

2.2 Optical properties of human tissues

In general, three photophysical processes affect light propagation in biological tissues: refraction, scattering and absorption [6]. These are defined in terms of refractive index (n), scattering coefficient (μ_s) and absorption coefficient (μ_a), respectively. Scattering of light occurs in media that contains fluctuations in the refractive index (n), whether such fluctuations are discrete particles or more continuous variations in (n).

In biomedical optics, scattering of photons is an important event. Scattering provides feedback during therapeutic procedures, and has diagnostic values as well. It depends on the ultrastructure of a tissue, e.g., the density of lipid membranes in the cells, the size of nuclei, the presence of collagen fibers, the status of hydration in the tissue, etc [7].

Another important event in biomedical optics is absorption of photons. Absorption is the primary event that allows a laser or other light source to cause a potentially therapeutic (or damaging) effect on a tissue. Without absorption, there is no energy transfer to the tissue and the tissue is left unaffected by the light. It also provides a diagnostic role, as well. Absorption can provide a clue as to the chemical composition of a tissue, and serve as a mechanism of optical contrast during imaging [7].

As stated earlier, scattering and absorption are defined by their coefficients. These coefficients are used and investigated as fingerprints in biological optics. While absorption coefficient (μ_a) provides information on the concentration of various chromophores [8], the scattering properties provide information on the form, size, and concentration of the scattering components in the medium [9-10].

The scattering properties are divided to scattering coefficient (μ_s), the reduced scattering coefficient (μ_s'), and anisotropy factor (g). There are other terms of concerns in tissue optical properties, such as: the total attenuation coefficient (μ_t), and the effective attenuation coefficient (μ_{eff}).

2.3 Propagation of continuous-wave light in tissues - Basic principles

Biological tissues are multi composite and inhomogeneous media. Each type of fiber structure or cell, including its specific organelles, may vary in terms of shape, size, refractive index, etc (figure 7). Therefore, light propagation within a tissue may be followed, at the same time, by multiple scattering, absorption, reflection,

transmission and depends on the scattering and absorbing parameters of the above-mentioned biological matter parameters.

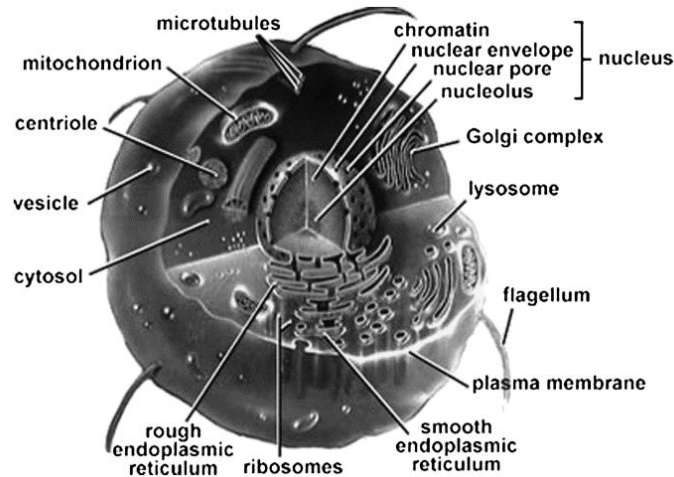


FIGURE 7. MAJOR ORGANELLES AND INCLUSIONS OF THE CELL.

A system of noninteracting spherical particles is the simplest tissue model. Mie theory rigorously describes the diffraction of light in a spherical particle. The development of this model involves taking into account the structures of the spherical particles, namely, the multilayered spheres and the spheres with radial nonhomogeneity, anisotropy, and optical activity.

Because connective tissue consists of fiber structures, a system of long cylinders is the most appropriate model for it. Muscular tissue, skin dermis, dura mater, eye cornea, and sclera belong to this type of tissue formed essentially by collagen fibrils. The solution of the problem of light diffraction in a single homogeneous or multilayered cylinder is also well understood.

Phase contrast microscopy has been used in particular to show that the structure of the refraction index inhomogeneities in mammalian tissues is similar to the structure of frozen turbulence in a number of cases [11]. This fact is of fundamental importance for understanding the peculiarities of light propagation in tissue, and it may be a key to the solution of the inverse problem of tissue structure reconstruction.

Currently, two approaches are followed in tissue light propagation modelling. The first one models tissues as a medium with a continuous random spatial distribution of optical parameters [11-12], where the second one considers tissue as a discrete ensemble of scatterers [13-14]. The choice of the approach is dictated by both the structural specificity of the tissue under study and the kind of light scattering characteristics that are to be

obtained. For example, blood is the most important biological example of a disperse system that entirely corresponds to the model of discrete particles.

Biological media are often modeled as ensembles of homogeneous spherical particles, since many cells and microorganisms, particularly blood cells, are close in shape to spheres or ellipsoids (figure 7). The sizes of cells and tissue structure elements vary in size from a few tenths of nanometers to hundreds of micrometers [15].

2.4 Major absorbers and scatterers

Molecules that absorb light are called chromophores (figure 8). Depending how light is absorbed, these molecules are divided to two types: those that absorb light through electric transitions and those that absorb light through vibrational transitions. Electronic transitions are relatively energetic and hence are associated with absorption of UV, VIS, and NIR wavelengths. Porphyrins are effective chromophores for absorbing photons. Hemoglobin and vitamin B12 are examples of porphyrins in biology. Protoporphyrin IX (PpIX) is one of the important factors in PDT. The field of infrared spectroscopy, studies the variety of bonds, which can resonantly vibrate or twist in response to IR wavelengths and thereby absorb such photons. Perhaps the most dominant chromophore in biology, which absorbs via vibrational transitions, is water. In the IR region, the absorption of water is the strongest contributor to tissue absorption.

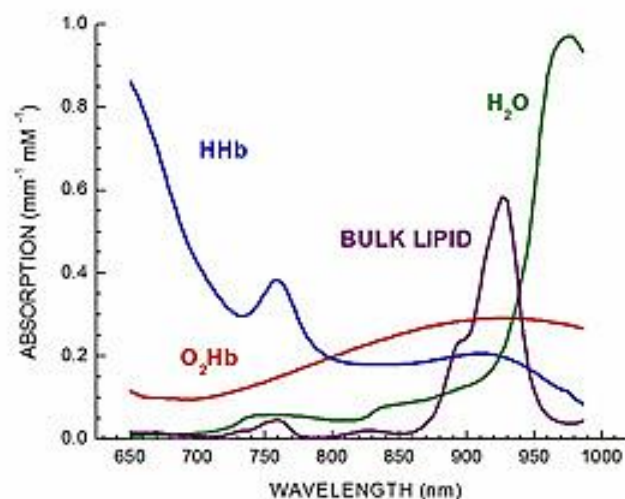


FIGURE 8. ABSORPTION SPECTRUM OF MAJOR TISSUE CHROMOPHORES

About the biological scatterers, it can be said that the light scattered by a tissue has interacted with the ultrastructure of the tissue. Tissue ultrastructure extends from membranes to membrane aggregates, collagen fibers, nuclei, and cells. Photons are most strongly scattered by those structures whose size matches the photon wavelength. Scattering of light by structures on the same size scale as the photon wavelength is described by Mie theory. Scattering of light by structures much smaller than the photon wavelength is called the Rayleigh limit of Mie scattering, or simply Rayleigh scattering.

Mitochondria, collagen fibers, and fibrils are examples of structures which scatter light in biology. Mitochondria are intracellular organelles about 1 μm in length (variable) which are composed of many folded internal lipid membranes called cristae. The basic lipid bilayer membrane is about 9 nm in width. The refractive index mismatch between lipid and the surrounding aqueous medium causes strong scattering of light. Folding of lipid membranes presents larger size lipid structures, which affect longer wavelengths of light. The density of lipid/water interfaces within the mitochondria make them especially strong scatterers of light. Collagen fibers (about 2-3 μm in diameter) are composed of bundles of smaller collagen fibrils about 0.3 μm in diameter (variable). Mie scattering from collagen fibers dominates scattering in the infrared wavelength range. About fibrils, it must be said that the periodic fluctuations in refractive index on this ultrastructural level, appear to contribute a Rayleigh scattering component that dominates the visible and ultraviolet wavelength ranges.

2.5 Optical window in biological tissue

The Optical window (also known as therapeutic window) defines the range of wavelengths where light has its maximum depth of penetration in tissue. Within the NIR window, scattering is the most dominant light-tissue interaction, and therefore the propagating light becomes diffuse rapidly. Since scattering increases the distance travelled by photons within tissue, the probability of photon absorption also increases. Because scattering has weak dependence on wavelength, the optical window is primarily limited by absorption, due to either blood at short wavelengths or water at long wavelengths.

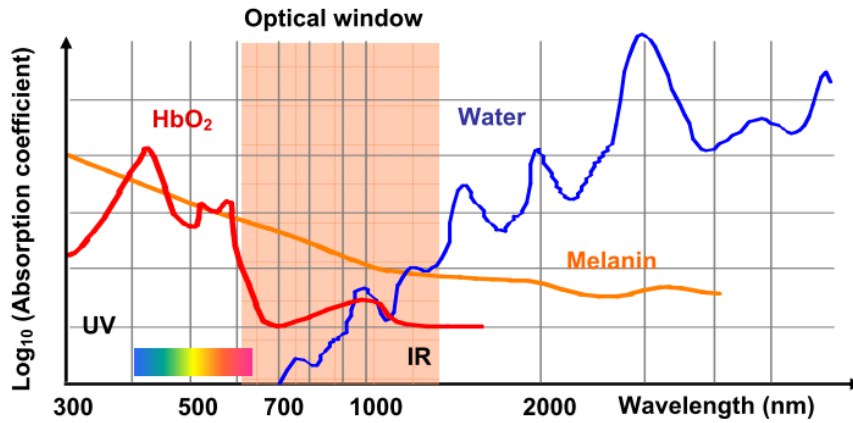


FIGURE 9. ABSORPTION SPECTRA OF SOME IMPORTANT CHROMOPHORES IN HUMAN SKIN TISSUE, AS FUNCTION OF WAVELENGTH. ADAPTED FROM REF [18].

Constituting 75 % of the tissue, water is the most important absorber in tissue, dominating in the UV ($\lambda < 200$ nm), and IR ($\lambda > 1300$ nm) region [NY 28]. Other important chromophores in tissue are hemoglobin and melanin. The absorption of light by blood depends on the oxygenated (HbO_2) and deoxygenated (Hb) haemoglobin. The absorption spectra shows one sharp peak at about 430 nm for HbO_2 , while dropping off until 530 nm, the spectra picks up at 540 nm and 576 nm, and finally its lowest absorption takes place for wavelengths above 600 nm (Figure 9). Melanin is a pigment in hair, skin and eye. Protecting the organism from UV radiation is the main function of melanin in the skin. Melanin absorption decreases with increasing wavelength. The low-absorbing region between approximately 630 nm and 1300 nm is referred to as the tissue optical window. In this range, the penetration of light into biological tissue is at its deepest.

Chapter 3 – Endometrial physiology and pathology

The uterus is the site of many physiological processes related to pregnancy, starting at implantation. It is the endometrium that is invaded by the trophoblast and the endometrium that in part determines the degree of maternal-fetal contact. Human female reproductive physiology and behavior have evolved to handle substantial energy demands and determine not only the viability of conception, but also 9-month gestation and often several years of lactation, with babies that are larger and larger-brained than all other primates. Only humans have such invasive fetal burrowing to maximize the transfer of glucose and oxygen from mother to fetus.

3.1 Endometrial Physiology

3.1.1 Uterus

The uterus is a major female hormone-responsive reproductive sex organ of most mammals including humans. On the one end, the cervix opens into the vagina, while the other is connected to the fallopian tubes. It is within the uterus that the fetus develops during gestation. The uterus consists of a body and a cervix. The cervix protrudes into the vagina. The uterus is held in position within the pelvis by condensations of endopelvic fascia, which are called ligaments. These ligaments include the pubocervical, transverse cervical ligaments, cardinal ligaments and the uterosacral ligaments. It is covered by a sheet-like fold of peritoneum, the broad ligament [19].

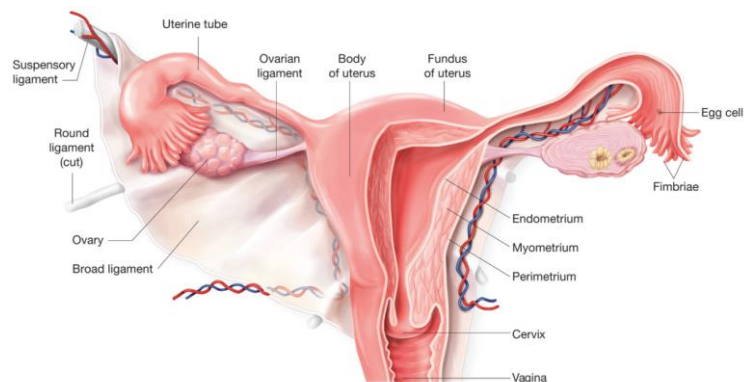


FIGURE 10. THE UTERUS. CUTAWAY VIEWS SHOW REGIONS OF THE UTERUS AND CERVIX AND ITS RELATIONSHIP TO THE UTERINE (FALLOPIAN) TUBES AND VAGINA.

The uterus is essential in sexual response by directing blood flow to the pelvis and to the external genitalia, including the ovaries, vagina, labia, and clitoris. The reproductive function of the uterus is to accept a fertilized ovum which passes through the utero-tubal junction from the fallopian tube. It implants into the endometrium, and derives nourishment from blood vessels which develop exclusively for this purpose. The fertilized ovum becomes an embryo, attaches to a wall of the uterus, creates a placenta, and develops into a fetus (gestates) until childbirth. Due to anatomical barriers such as the pelvis, the uterus is pushed partially into the abdomen due to its expansion during pregnancy. Even during pregnancy the mass of a human uterus amounts to only about a kilogram.

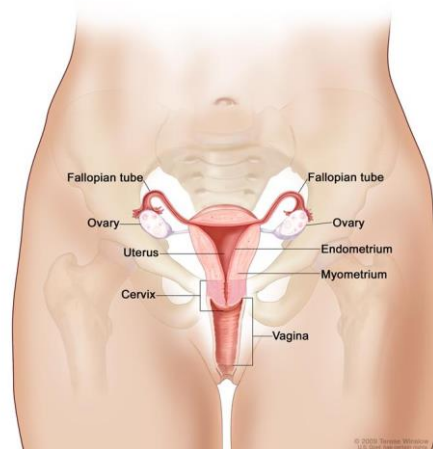


FIGURE 11. ANATOMY OF THE FEMALE REPRODUCTIVE SYSTEM. THE ORGANS IN THE FEMALE REPRODUCTIVE SYSTEM INCLUDE THE UTERUS, OVARIES, FALLOPIAN TUBES, CERVIX, AND VAGINA. THE UTERUS HAS A MUSCULAR OUTER LAYER CALLED THE MYOMETRIUM AND AN INNER LINING CALLED THE ENDOMETRIUM.

The uterus is essential in sexual response by directing blood flow to the pelvis and to the external genitalia, including the ovaries, vagina, labia, and clitoris. The reproductive function of the uterus is to accept a fertilized ovum which passes through the utero-tubal junction from the fallopian tube. It implants into the endometrium, and derives nourishment from blood vessels which develop exclusively for this purpose. The fertilized ovum becomes an embryo, attaches to a wall of the uterus, creates a placenta, and develops into a fetus (gestates) until childbirth. Due to anatomical barriers such as the pelvis, the uterus is pushed partially into the abdomen due to its expansion during pregnancy. Even during pregnancy the mass of a human uterus amounts to only about a kilogram.

The uterus is located inside the pelvis immediately dorsal (and usually somewhat rostral) to the urinary bladder and ventral to the rectum. The human uterus is pear-shaped and about 7.5 cm long. The uterus can be divided anatomically into four segments: The fundus, corpus, cervix and the internal orifice. Uterus is consisted of three layers, the endometrium, the myometrium and the perimetrium, from innermost to outermost.

3.1.2 Endometrium

The endometrium is the inner mucous membrane of the mammalian uterus. During the follicular phase of the menstrual cycle, the endometrium thickens in preparation to accept an embryo should conception occur. If pregnancy occurs, the endometrium undergoes a process called decidualization. The placenta, which is fetal derived, invades the endometrium to allow for the transport of nutrients and oxygen from the mother to the fetus. If conception does not occur, the endometrial lining begins to breakdown and sheds through menstruation.

Function

The endometrium is the innermost glandular layer and functions as a lining for the uterus, preventing adhesions between the opposed walls of the myometrium, thereby maintaining the patency of the uterine cavity. During the menstrual cycle or estrous cycle, the endometrium grows to a thick, blood vessel-rich, glandular tissue layer. This represents an optimal environment for the implantation of a blastocyst upon its arrival in the uterus. The endometrium is central, echogenic (detectable using ultrasound scanners), and has an average thickness of 6.7 mm. During pregnancy, the glands and blood vessels in the endometrium further increase in size and number. Vascular spaces fuse and become interconnected, forming the placenta, which supplies oxygen and nutrition to the embryo and foetus.

Cycle

The endometrial lining undergoes cyclic regeneration. The endometrium initially proliferates under the influence of estrogen. However, once ovulation occurs, in addition to estrogen, the ovary will also start to produce progesterone. This changes the proliferative pattern of the endometrium to a secretory lining. Eventually, the secretory lining provides a hospitable environment for one or more blastocysts. If a blastocyst implants, then the lining remains as decidua. The decidua becomes part of the placenta; it provides support and protection for the gestation. In humans, the cycle of building and shedding the endometrial lining lasts an average of 28 days. The endometrium itself produces certain hormones at different points along the cycle. This affects other portions of the reproductive system.

Histology

The endometrium consists of a single layer of columnar epithelium resting on the stroma, a layer of connective tissue that varies in thickness according to hormonal influences. Simple tubular uterine glands reach from the endometrial surface through to the base of the stroma, which also carries a rich blood supply of spiral arteries. In a woman of reproductive age, two layers of endometrium can be distinguished. These two layers occur only in endometrium lining the cavity of the uterus, not in the lining of the Fallopian tubes [20].

The functional layer is adjacent to the uterine cavity. This layer is built up after the end of menstruation during the first part of the previous menstrual cycle. Proliferation is induced by estrogen (follicular phase of menstrual cycle), and later changes in this layer are engendered by progesterone from the corpus luteum (luteal phase). It is adapted to provide an optimum environment for the implantation and growth of the embryo. This layer is completely shed during menstruation. The basal layer, adjacent to the myometrium and below the functional layer, is not shed at any time during the menstrual cycle, and from it the functional layer develops.

In the absence of progesterone, the arteries supplying blood to the functional layer constrict, so that cells in that layer become ischaemic and die, leading to menstruation. It is possible to identify the phase of the menstrual cycle by observing histological differences at each phase:

PHASE	DAYS	THICKNESS	EPITHELIUM
MENSTRUAL PHASE	1–4	Thin	Absent
PROLIFERATIVE PHASE	4–14	Intermediate	Columnar
SECRETORY PHASE	15–28	Thick	Columnar. Also visible are helicine branches of uterine artery

TABLE 1. IDENTIFYING THE PHASE OF THE MENSTRUAL CYCLE BY OBSERVING HISTOLOGICAL DIFFERENCES.

Chorionic tissue can result in marked endometrial changes, known as an Arias-Stella reaction, that have an appearance similar to cancer [21]. Historically, this change was diagnosed as endometrial cancer and it is important only in so far as it should not be misdiagnosed as cancer.

3.2 Endometrial Pathology

Endometrial pathology refers to any condition that affects the endometrium. Some of the more familiar endometrial conditions include fibroids, cysts, endometriosis and endometrial cancer.

3.2.1 Adenomyosis

Adenomyosis is a medical condition characterized by the presence of ectopic glandular tissue found in muscle [22]. Previously named as endometriosis interna, adenomyosis actually differs from endometriosis and these two disease entities are found together in only 10% of the case. It usually refers to ectopic endometrial tissue (the inner lining of the uterus) within the myometrium (the thick, muscular layer of the uterus). The term "adenomyometritis" specifically implies involvement of the uterus [24-24]. The condition is typically found in women between the ages of 35 and 50. Patients with adenomyosis can have painful and/or profuse menses (dysmenorrhea & menorrhagia, respectively). However, because the endometrial glands can be trapped in the myometrium, it is possible to have increased pain without increased blood. (This can be used to distinguish adenomyosis from endometrial hyperplasia; in the latter condition, increased bleeding is more common). In adenomyosis, basal endometrium penetrates into hyperplastic myometrial fibers. Therefore, unlike functional layer, basal layer does not undergo typical cyclic changes with menstrual cycle [23]. Adenomyosis may involve the uterus focally, creating an adenomyoma. With diffuse involvement, the uterus becomes bulky and heavier.

3.2.2 Endometritis

Endometritis refers to inflammation of the endometrium [24], the inner lining of the uterus. Pathologists have traditionally classified endometritis as either acute or chronic: acute endometritis is characterized by the presence of microabscesses or neutrophils within the endometrial glands, while chronic endometritis is distinguished by variable numbers of plasma cells within the endometrial stroma. The most common cause of endometritis is infection. Symptoms include lower abdominal pain, fever and abnormal vaginal bleeding or discharge. Caesarean section, prolonged rupture of membranes and long labor with multiple vaginal

examinations are important risk factors. Treatment is usually with broad-spectrum antibiotics. The term "endomyometritis" is sometimes used to specify inflammation of the endometrium and the myometrium [25].

3.2.3 Endometriosis

Endometriosis is a gynecological condition in which cells from the lining of the uterus (endometrium) appear and flourish outside the uterine cavity, most commonly on the membrane which lines the abdominal cavity, the peritoneum. The uterine cavity is lined with endometrial cells, which are under the influence of female hormones. Endometrial cells in areas outside the uterus are also influenced by hormonal changes and respond in a way that is similar to the cells found inside the uterus. Symptoms of endometriosis are pain and infertility. The pain often is worse with the menstrual cycle and is the most common cause of secondary dysmenorrhea. Endometriosis was first identified by Baron Carl von Rokitansky in 1860 [26]. Endometriosis is typically seen during the reproductive years; it has been estimated that endometriosis occurs in roughly 6–10% of women. Symptoms may depend on the site of active endometriosis. Its main but not universal symptom is pelvic pain in various manifestations. Endometriosis is a common finding in women with infertility [27]. Endometriosis has a significant social and psychological impact [28]. There is no cure for endometriosis, but it can be treated in a variety of ways, including pain medication, hormonal treatments, and surgery [29].

An **endometrioma**, **endometrioid cyst**, **endometrial cyst**, or chocolate cyst of ovary is a condition related to endometriosis. It is caused by endometriosis [26], and formed when a tiny patch of endometrial tissue (the mucous membrane that makes up the inner layer of the uterine wall) bleeds, sloughs off, becomes transplanted, and grows and enlarges inside the ovaries. As the blood builds up over months and years, it turns brown. When it ruptures, the material spills over into the pelvis and onto the surface of the uterus, bladder, bowel, and the corresponding spaces between.

3.2.4 Uterine fibroid

A uterine fibroid is a leiomyoma (benign (non-cancerous) tumor from smooth muscle tissue) that originates from the smooth muscle layer (myometrium) of the uterus. Fibroids are often multiple and if the uterus contains too many leiomyomata to count, it is referred to as diffuse uterine leiomyomatosis. The malignant version of a fibroid is extremely uncommon and termed a leiomyosarcoma. Other common names are uterine leiomyoma [30], myoma, fibromyoma, fibroleiomyoma. Fibroids are the most common benign tumors in females and typically found during the middle and later reproductive years. While most fibroids are asymptomatic, they can grow and cause heavy and painful menstruation, painful sexual intercourse, and

urinary frequency and urgency. Some fibroids may interfere with pregnancy although this appears to be very rare [31]. In the United States, symptoms caused by uterine fibroids are a very frequent indication for hysterectomy [32].

3.2.5 Endometrial Hyperplasia

Most cases of endometrial hyperplasia result from high levels of estrogens, combined with insufficient levels of the progesterone-like hormones which ordinarily counteract estrogen's proliferative effects on this tissue. This may occur in a number of settings, including obesity, polycystic ovary syndrome, estrogen producing tumours (e.g. granulosa cell tumour) and certain formulations of estrogen replacement therapy. Endometrial hyperplasia is a significant risk factor for the development or even co-existence of endometrial cancer, so careful monitoring and treatment of women with this disorder is essential. Like other hyperplastic disorders, endometrial hyperplasia initially represents a physiological response of endometrial tissue to the growth-promoting actions of estrogen. However, the gland-forming cells of a hyperplastic endometrium may also undergo changes over time which predispose them to cancerous transformation. Several histopathology subtypes of endometrial hyperplasia are recognisable to the pathologist, with different therapeutic and prognostic implications [33].

3.2.6 Endometrial Cancer

Endometrial cancer is any of several types of malignancies that arise from the endometrium, or lining, of the uterus. Endometrial cancers are the most common gynecologic cancers in developed countries [34], with over 142,200 women diagnosed each year. The incidence is on a slow rise secondary to an increasing population age and an increasing body mass index, with 39% of cases attributed to obesity [35]. The most common subtype, endometrioid adenocarcinoma, typically occurs within a few decades of menopause, is associated with obesity, excessive estrogen exposure, often develops in the setting of endometrial hyperplasia, and presents most often with vaginal bleeding. Endometrial carcinoma is the third most common cause of gynecologic cancer death (behind ovarian and cervical cancer). A total abdominal hysterectomy (surgical removal of the uterus) with bilateral salpingo-oophorectomy is the most common therapeutic approach. Endometrial cancer may sometimes be referred to as uterine cancer. However, different cancers may develop not only from the endometrium itself but also from other tissues of the uterus, including cervical cancer, sarcoma of the myometrium, and trophoblastic disease.

Most endometrial cancers are carcinomas (usually adenocarcinomas), meaning that they originate from the single layer of epithelial cells that line the endometrium and form the endometrial glands. There are many microscopic subtypes of endometrial carcinoma, but they are broadly organized into two categories, type I and type II, based on clinical features and pathogenesis [36].

The first type, **type I** endometrial cancers occur most commonly in pre- and peri-menopausal women, are more common in white women, often with a history of excessive thickening of the inner lining of the uterus (endometrial hyperplasia) and exposure to elevated levels of estrogen that are not counterbalanced by progesterone (unopposed estrogen exposure). Type I endometrial cancers are often low-grade, minimally invasive into the underlying uterine wall (myometrium), and are of the endometrioid type, and carry a good prognosis [36]. In endometrioid cancer, the cancer cells grow in patterns reminiscent of normal endometrium.

The second type, **type II** endometrial cancers usually occur in older, post-menopausal women, are more common in African-Americans, and are not associated with increased exposure to estrogen. Type II endometrial cancers are often high-grade, with deep invasion into the underlying uterine wall (myometrium), and are of the serous or clear cell type, and carry a poorer prognosis [36].

3.2.7 Asherman's syndrome

Asherman's syndrome (AS) or Fritsch syndrome, is a condition characterized by adhesions and/or fibrosis of the endometrium most often associated with dilation and curettage of the intrauterine cavity [37]. A number of other terms have been used to describe the condition and related conditions including: injurious intrauterine adhesions, uterine/cervical atresia, traumatic uterine atrophy, sclerotic endometrium, endometrial sclerosis, and intrauterine synechiae [38].

3.2.8 Endometrial Polyp

An endometrial polyp or uterine polyp is a mass in the inner lining of the uterus [40]. They may have a large flat base (sessile) or be attached to the uterus by an elongated pedicle (pedunculated) [40-41]. Pedunculated polyps are more common than sessile ones [42]. They range in size from a few millimeters to several centimeters [41]. If pedunculated, they can protrude through the cervix into the vagina [43] Small blood vessels may be present, particularly in large polyps [40].

No definitive cause of endometrial polyps is known, but they appear to be affected by hormone levels and grow in response to circulating estrogen.[41] They often cause no symptoms [42]. Where they occur,

symptoms include irregular menstrual bleeding, bleeding between menstrual periods, excessively heavy menstrual bleeding (menorrhagia), and vaginal bleeding after menopause [44]. Bleeding from the blood vessels of the polyp contributes to an increase of blood loss during menstruation and blood "spotting" between menstrual periods, or after menopause [44] If the polyp protrudes through the cervix into the vagina, pain (dysmenorrhea) may result [42].

Chapter 4 - Endometrial Imaging techniques

4.1 Classical Methods

4.1.1 Saline Infusion sonohysterography

Saline infusion sonohysterography refers to a procedure in which fluid is instilled into the uterine cavity transcervically to provide enhanced endometrial visualization during transvaginal ultrasound examination. The technique improves sonographic detection of endometrial pathology, such as polyps, hyperplasia, cancer, leiomyomas, and adhesions. In addition, it can help avoid invasive diagnostic procedures in some patients as well as optimize the preoperative triage process for those women who require therapeutic intervention. It is easily and rapidly performed at minimal cost, well-tolerated by patients, and is virtually devoid of complications.

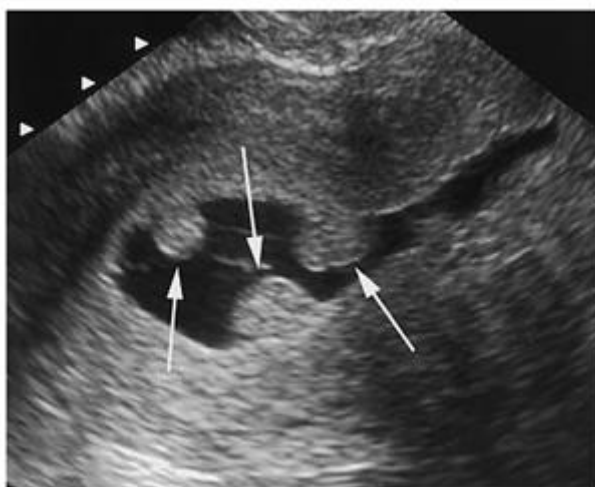


FIGURE 12. ENDOMETRIAL POLYP SEEN IN A SALINE INFUSION SONOHYTEROGRAM [45].

4.1.2 Transvaginal ultrasound

Transvaginal ultrasound is a imaging technique used to create a picture of the genital tract in women. The hand-held device that produces the ultrasound waves is inserted directly into the vagina, close to the pelvic structures, thus often producing a clearer and less distorted image than obtained through transabdominal ultrasound technology, where the probe is located externally on the skin of the abdomen. Transvaginal

ultrasound can be used to evaluate problems or abnormalities of the female genital tract. It may provide more accurate information than transabdominal ultrasound for women who are obese, for women who are being evaluated or treated for infertility, or for women who have difficulty keeping a full bladder. However, it does provide a view of a smaller area than the transabdominal ultrasound.

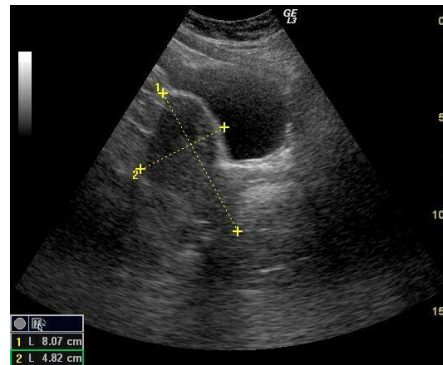


FIGURE 13. GROSSY THICKENED ENDOMETRIUM DETECTED BY TRANSVAGINAL SONOGRAPHY OF THE UTERUS [46].

4.1.3 MRI

Magnetic resonance imaging (MRI) is a commonly used technique in the workup of obstetric and gynecologic abnormalities and in the pre- and postprocedural evaluation for uterine artery embolization. Optimal MRI of the female pelvis and uterus should be performed on a high-field-strength MRI system that uses local phased-array coils. The increased signal-to-noise ratio provided by the surface coils allows for small field-of-view imaging that results in higher spatial resolution [47]. Contrast enhancement is used to document the extent of endometrial carcinoma invasion or to detect the presence of necrosis in uterine leiomyomas. Dynamic contrast injection can be used in women who are considering uterine artery embolization (UAE) in order to evaluate the uterine arteries and the potential collateral gonadal arterial supply.

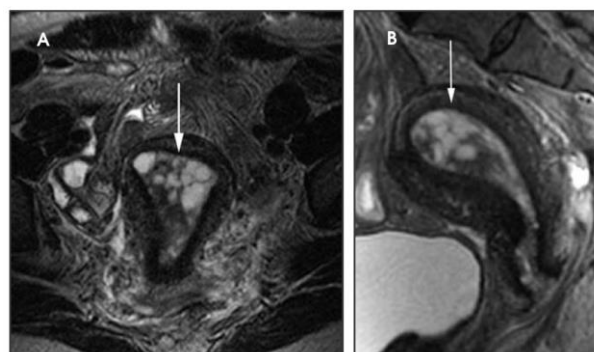


FIGURE 14. MRI DEPICTION OF ENDOMETRIAL HYPERPLASIA. (A) AXIAL AND (B) SAGITTAL T2-WEIGHTED IMAGES OF THE UTERUS SHOW CYSTIC THICKENING OF THE ENDOMETRIAL CANAL (ARROWS) IN A PATIENT ON TAMOXIFEN FOR BREAST CANCER [47].

4.1.4 Diagnostic hysteroscopy

Hysteroscopy is the examination of the internal cavity of the uterus (endometrium) with the use of a fine endoscope (hysteroscope) which is inserted into the uterus through the vagina and cervix. With hysteroscopy the endometrium is examined and treated more reliably than with any other method (transvaginal ultrasound, hysterosalpingogram, dilatation & Curettage, etc). Hysteroscopy is performed for a variety of gynecological problems such as abnormal uterine bleeding (menorrhagia), infertility, polyps, fibroids, endometrial adhesions, uterine diaphragm, endometrial hyperplasia, cancer etc. Diagnostic and micro-invasive hysteroscopy is performed under local anesthesia while invasive hysteroscopy is performed either under local, general or epidural anesthesia, depending on medical settings and patient's characteristics. Hospital stay ranges from a one hour to one day depending on the case. As a diagnostic and therapeutic tool hysteroscopy is essential in modern gynecology and is performed with great safety and accuracy.



FIGURE 15. VIEW OF A SUBMUCOUS FIBROID BY HYSTEROSCOPY.

4.2 Novel diagnostic Advances in Endoscopy

Conventional white light endoscopy is associated with a disproportionate miss rate for subtle lesions (e.g. flat adenomas). Numerous studies have demonstrated that experienced gastroenterologists miss up to 6% of advanced adenomas and 24% of all adenomas. Certain endoscopic techniques are associated highly with missed lesions. Therefore, the present and future directions of endoscopy are to improve the diagnostic techniques through monitoring adenoma detection rates, withdrawal time with better education and practice improvement interventions. However, subtle dysplastic and early neoplastic lesions remain often too small, flat or depressed to be detected during regular standard white-light endoscopy even with ideal

(improved) techniques. This has led to intensified efforts to develop other alternative, optically based techniques as well as other diagnostic modalities that would compete with and/or be complementary to existing conventional endoscopic

Imaging enhanced technologies that are currently available in endoscopy include field enhancement techniques such as chromoendoscopy, auto fluorescence imaging (AFI) narrow band imaging (NBI) and digital image processing (like FICE and i-Scan), as well as point enhancement techniques, such as high definition television (HDTV) endoscopy and confocal laser endomicroscopy (CLE). These enhancements offer improved visualization of lesions and/or abnormalities, which, in turn, may provide guidance in determining optimal treatment. Currently, endoscopes with integrated zoom lenses and probe microscopes small enough to be passed through the accessory endoscopic channel are available. With these add-ons, intestinal tissue can be visualized at a cellular or sub cellular level and may be able to provide in vivo optical histology. Endoscopic systems that are equipped with field enhancement modes accommodate high resolution optical sensors and provide high-magnification capabilities and improved image quality. High resolution endoscopes with high-density charge coupled device (CCD) provided resolutions from 0.6 up to 2 megapixels (HDTV systems) and produce high magnification images for the detection of microscopic abnormalities in tissue. They provide image enlargement up to 120 times compared with 30 times with standard endoscopes. In this thesis the above mentioned novel endoscopic imaging enhancement technologies will be reviewed and a new approach for enhanced image in hysteroscopy will be presented.

4.2.1 Chromoendoscopy

Chromoendoscopy involves the topical application of stains or pigments to impose tissue localization, characterization or diagnosis during endoscopy. This image enhancement method has been applied in a variety of clinical settings and throughout all gastrointestinal tract segments that are accessible to an endoscope, as the equipment needed is widely available and the staining techniques are simple, inexpensive and safe. Examples of stained tissues are in Figure 16. Interest has been renewed in recent years in part because of the development of new technologies such as endoscopic mucosal resection and photodynamic therapy, which require precise visual tissue characterization. However, staining of the entire mucosa is a time consuming process. Thus, efforts have been made to develop so-called virtual chromoendoscopy with the use of narrow band imaging or the Fujinon intelligent color enhancement system (FICE) to enhance mucosal contrast with no requirements for the use of topical stains. Like many endoscopic techniques, the impact of chromoendoscopy on clinical outcomes relative to standard endoscopic and histological methods has not been established in large controlled trials.

4.2.2 Auto fluorescence Imaging (AFI) Endoscopy

Living tissues contains proteins that emit auto fluorescence when exposed to proper wavelength of light (ultraviolet and blue). Many devices have been manufactured and patented for auto fluorescence endoscopy, initially for bronchoscopy. The principle of operation is simple: a powerful ultraviolet or blue light source is used to excite the living tissue and a video camera module, featuring one very sensitive optics sensor (e.g. a CCD) filtered to observe only the excitation spectrum and another for conventional endoscopic images. Deuterium lamps were initially utilized as excitation sources but soon were replaced by lasers coupled with a conventional white light source. Lasers have numerous advantages as they offer very high intensity, narrow monochromatic illumination and a variety of wavelength available.

The recent advances in semiconductor technologies have provided small size powerful blue lasers (at 405nm wavelength) that have allowed the designers of the endoscopes to integrate the laser at the tip of the endoscope. Also CMOS image sensors have been manufactured especially for endoscopic applications with dimensions that enable the placement of two image sensors at the end tip of many endoscopes.

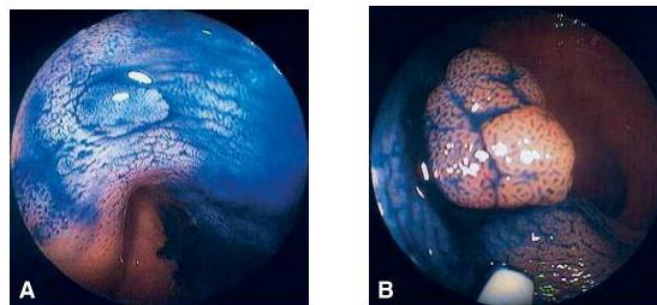


FIGURE 16. A, COLONOSCOPIC VIEW OF HYPERPLASTIC POLYP. B, COLONOSCOPIC VIEW OF ADENOMATOUS POLYP. IN BOTH CASES TISSUE WAS STAINED WITH 0.9% INDIGO CARMINE BYE [48].

Olympus, in order to provide better image enhancement in its endoscopic high range systems “EVIS LUCERA SPECTRUM”, utilizes a 540-560nm reflectance image along with the 390-470nm excitation image. The pseudo color AFI image displayed to the user is created by assigning the auto fluorescence image to the Green Color plane of the pseudo color image and the reflectance image to the Red and Blue Color planes (Figure 17). Other companies use similar concepts for better visualization of the fluorescent tissue.

The common fluorescence substances in the living tissue include amino acids like NADH, flavin, and collagen richly found in the connective tissue. Several investigators have reported studies of auto fluorescence from living tissue. Although efforts in such studies, relationship between the auto fluorescence and the malignancy of the lesion is not still unclear in several tissue types. Gono K. et al. also investigated auto fluorescence spectra of the living tissue. A spectroscope was used and attached to it was an optical fiber probe

compatible for an instrumental channel of the endoscope body. Several auto fluorescence spectra from normal colon tissues and adenomas were selected.

A recent multi-centre study by Curvers et al investigated the diagnostic potential of endoscopic tri-modal imaging including autofluorescence imaging (AFI) as well as high resolution endoscopy , and narrow band imaging (NBI) for the detection of early neoplasia in Barrett’s esophagus. The investigators noted that the addition of AFI to high resolution endoscopy increased the detection of both the number of patients and the number of lesions with early neoplasia in patients with Barrett’s esophagus.

Furthermore, the initial false positive rate of AFI was reduced after detailed inspection with NBI. The results of this study demonstrate the promising role of prototype endoscopic systems combining the use of AFI and NBI technologies in one endoscope.

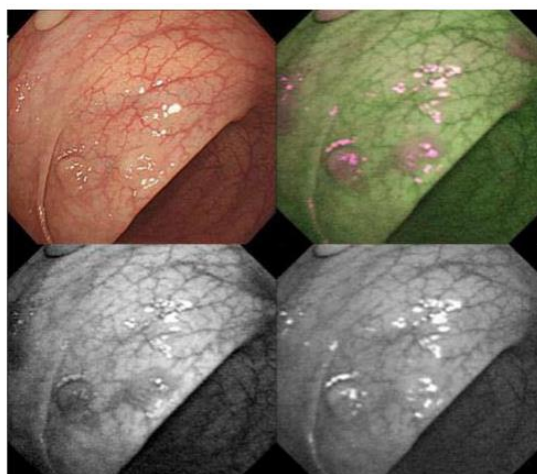


FIGURE 17. IMAGE OF COLON POLYPS. UPPER LEFT IS WHITE LIGHT IMAGE. UPPER RIGHT IS AFI PSEUDO COLOR IMAGE. BOTH RIGHT IS THE GREEN CHANNEL REFLECTANCE IMAGE AND BOTTOM LEFT THE FLUORESCENCE IMAGE.

Moreover, colonic autofluorescence has also been described both at glandular and cellular level and appears to be promising. In the studies by DaCosta et al dysplastic and adenomatous epithelial cells had much higher autofluorescence and contained numerous highly auto fluorescent lysosomal granules. Epithelial autofluorescence may be helpful in distinguishing hyperplastic and adenomatous lesions.

4.2.3 Narrow band Imaging (NBI) Endoscopy

Narrow Band Imaging was developed by Olympus as an optical image improvement technology that enhances vessels in the surface of the mucosa. In the NBI endoscopic system, RGB and bandpass filters are rotated in

front of a Xenon lamp to provide illumination to generate either a traditional RGB image or a narrow band wavelength pseudo color image. As the illumination changes sequentially with the rotating filters, a CCD detects each image. Next, an image processor produces color images by composing the images acquired. If the filters are the common RGB filters, the image produced is equivalent with that captured by a color (RGB) CCD camera.

However, it is difficult to see information that appears in a specific wavelength. For that reason, the narrow band pass filters used in NBI systems are selected in the blue filter wavelength and designed to correspond to the absorption spectrum of the hemoglobin. Also, because blue light penetrates into the superficial-most layers, the mucosal pattern is highlighted, whereas the deeper layers are not seen.

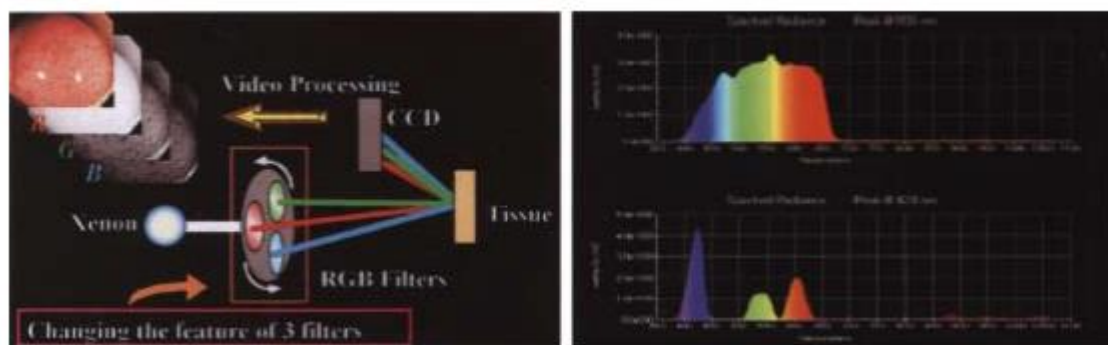


FIGURE 18. NBI IMAGE ACQUISITION PROCESS (LEFT) AND NBI OPTICAL FILTER PROPERTIES (RIGHT BOTTOM).

The initial designs of the NBI systems incorporated three bandpass filters, one at 415nm, the second one at 540nm and a third at 600nm. Each image captured was assigned to the responding channel of the pseudo color NBI image (Figure 18). In another initial NBI system (EVIS 240; Olympus Co Ltd) a xenon lamp and rotation disk with 3 broadband filters and three NBI filters at 415nm, 445nm and 500nm were selected to obtain images of the micro-vascular structure. Because 415nm is the hemoglobin absorption band, the thin blood vessels such as capillaries on the mucosal surface can be seen most clearly on this wavelength. The latest designs though use only the first two bandpass filters at 415nm and 540nm. Early studies have demonstrated the value of this technology in the evaluation of patients with upper GI lesions including Barrett's esophagus dysplasia. NBI technology is also useful in the classification of colorectal lesions as many researchers have demonstrated. However, a few recent studies have revealed conflicting results with no improvement in adenoma detection rates with the use of this novel technique. The results of Gross et al prospective randomized back-to-back trial comparing narrow band imaging to conventional colonoscopy for adenoma detection shows that the miss rate for polyps, and for adenomas, may be lower

with high definition NBI than for standard colonoscopy. East et al also demonstrated that NBI could play a role in adenoma detection in high risk groups as they found that a second additional examination with NBI doubled the total number of adenomas detected in 62 patients with hereditary non-polyposis colorectal cancer.

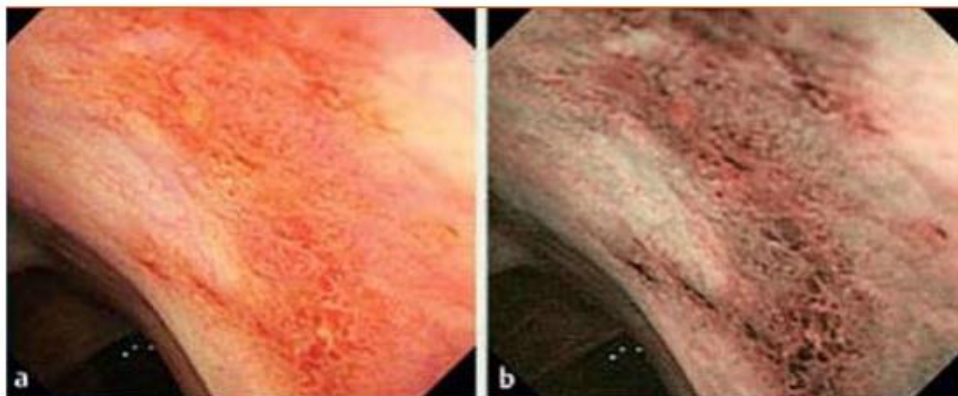


FIGURE 19. IRREGULAR MUCOSA WITH HIGH-GRADE NEOPLASIA IN A PATIENT WITH LONG-STANDING ULCERATIVE COLITIS. **A**, VIEWED WITH WHITE LIGHT ENDOSCOPY AND **B**, BY NBI, REVEALING A KUDO TYPE IV PIT PATTERN.

4.2.4 Fujinon intelligent color enhancement (FICE) and i-Scan endoscopic systems

Eager to provide endoscopic systems with image enhancement technologies, Fujinon and most recently Pentax Medical Company developed all-digital endoscopic systems to provide diagnostic assistance to the physicians. To many researchers these systems are known as computed virtual chromoendoscopy imaging systems, as their aim is to provide similar visual results without staining. While the NBI system depends on optical filters within the light source, the FICE system is based on a computed spectral estimation technology that processes the reflected photons to reconstruct virtual images with a choice of different wavelengths. An RGB image is captured and disintegrated into each color component. Then, and in real time, a digital signal processor performs matrix calculations for each pixel using stored coefficients corresponding to a desired wavelength. After that a pseudo color image is reconstructed featuring one to three selected wavelengths. Various combinations of wavelengths are preset for the user that provide image enhancement for specific areas of interest. This leads to enhancement of the tissue microvasculature as a result of the differential optical absorption of light by hemoglobin in the mucosa. These abnormal areas can be defined by the magnification.

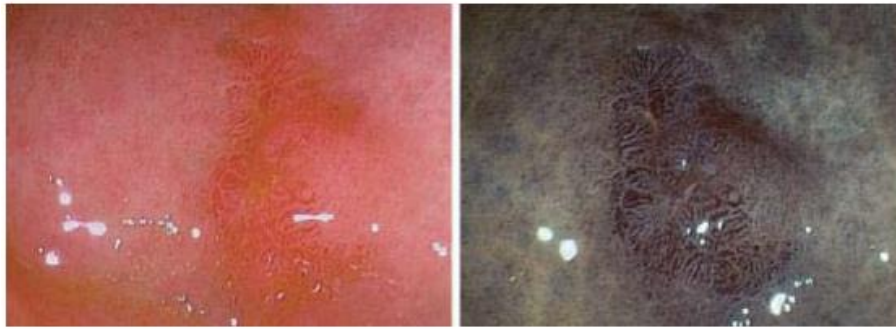


FIGURE 20. EARLY GASTRIC CANCER AS SEEN WITH WHITE LIGHT (LEFT) AND WITH FICE (RIGHT).

The i-Scan system is considered as a digital contrast method, with three modes of image enhancement: surface enhancement (SE), contrast enhancement (CE) and tone enhancement (TE). In SE mode, the structure is enhanced through the detection of the edges and their enhancement. In common endoscopic image sensor systems, minor changes in structure are perceived as noise, and the area that shows such changes is smoothed out from their image processing algorithms. With SE, on the other hand, adjustment of the noise erasure function allows more evident enhancement of the edges, which corresponds to minor changes in structure, making it easier to check changes on the basis of structural differences. With CE mode, areas lower in luminance intensity compared to surrounding pixels are identified from the luminance intensity data of each pixel, followed by relative enhancement of the Blue color channel through the slight suppression of Red and Green color channels in this low luminance area, resulting in slightly a bluish white color of the area applied. Finally, with TE mode the RGB color channels of an ordinary endoscope image are split into each color channel (Red, Green and Blue), and each channel is converted independently along the tone curve, followed by a re-synthesis of the three components to yield a pseudo color image. The tone curve is changed according to the need of the user and provides various modes, depending in the area of application. Sample images can be seen in figure 20.

The FICE system used in esophageal neoplasia demonstrated improvement in the detection of early neoplasia. The application of FICE technology in the detection and classification of colorectal lesions is also being currently investigated. Pohl et al in their prospective trial compared computed virtual chromoendoscopy system (FICE) with other modalities such as standard colonoscopy, conventional chromoendoscopy with indigo carmine in low and high magnification modes for determination of colonic lesion histology. Based on this study, the FICE system was able to identify morphological details that efficiently predicted adenomatous histology and was superior to standard colonoscopy and equivalent to conventional chromoendoscopy. As far as i-Scan endoscopic system is concerned, similar studies are yet available.



FIGURE 21. ESOPHAGEAL CANCER AS CAPTURED WITH AN I-SCAN SYSTEM. **A,** THE CONVENTIONAL WHITE LIGHT IMAGE. **B,** SE + CE MODES ENABLED CAPTURED IMAGE. **C,** TE MODE CAPTURED IMAGE.

4.2.5 Confocal laser endomicroscopy (CLE)

Confocal laser endomicroscopy (CLE) is one of the newest advancements in diagnostic endoscopy. Recent technologic advances allowed for a confocal imaging microscope to be integrated into the tip of a conventional endoscope (Pentax Medical Company), or in a probe, which can be passed through the working channel of the endoscope (Mauna Kea Technologies). The aim of this technology is to provide real-time in vivo histologic images, or so-called “virtual biopsy specimens,” of the GI mucosa during endoscopy. Confocal endomicroscopy allows high resolution imaging of cellular and sub cellular tissue when optical slices of the mucosal surface created by detecting reflected light and tissue autofluorescence enhances through the administration of IV or topical contrast fluorescent contrast agents, like IV fluorescein sodium. Sample images are available in figure 22.

The first report on the use of confocal endomicroscopy was made from Kiesslich et al in 42 patients during ongoing colonoscopy in diagnosing intraepithelial neoplasia and colorectal cancer. A total of 134 small lesions (mean size 4 mm) were identified during colonoscopy after staining with methylene blue. According to the study, intraepithelial neoplasia was predicted with the help of the confocal endoscope with a sensitivity of 97% and a specificity of 99% (accuracy, 99%). The potential applications of this technology extends beyond the discrimination of neoplastic and non-neoplastic (hyperplastic) polyps, to detection of other pathologies such as Barrett’s esophagus, esophagitis, gastritis, coeliac disease, etc. In a study of 63 patients with Barrett’s esophagus using fluorescein-aided endomicroscopy, Kiesslich et al predicted Barrett’s esophagus with a sensitivity of 98% and specificity of 94%. A limitation of the confocal system used in the above studies includes its reliance on a single integrated confocal endoscope. Recently, a miniature probe confocal laser endomicroscopy was developed to overcome that difficulty. At this moment is the world smallest microscope, available through the integration of numerous technological advances in miniature optics, nanomaterials, high speed scanning and advanced real time image processing. This probe can be passed through the accessory channel of almost any endoscope and be used as needed in any endoscopy case.

Becker et al studied 7 patients with various GI pathologies and confirmed that mini probe-based confocal microscopy in conjunction with video mosaicing can provide images similar to standard histopathology. Another concern regarding confocal endomicroscopy is the learning curve of the physicians and the reliable interpretation of the images. Very good knowledge of histopathology is needed for the endoscopist. According to Buchner et al, the interpretation of images is highly reliable among physicians, while the learning curve appears to be rapid among new users, achieving accuracy greater than 80% after 60 cases.

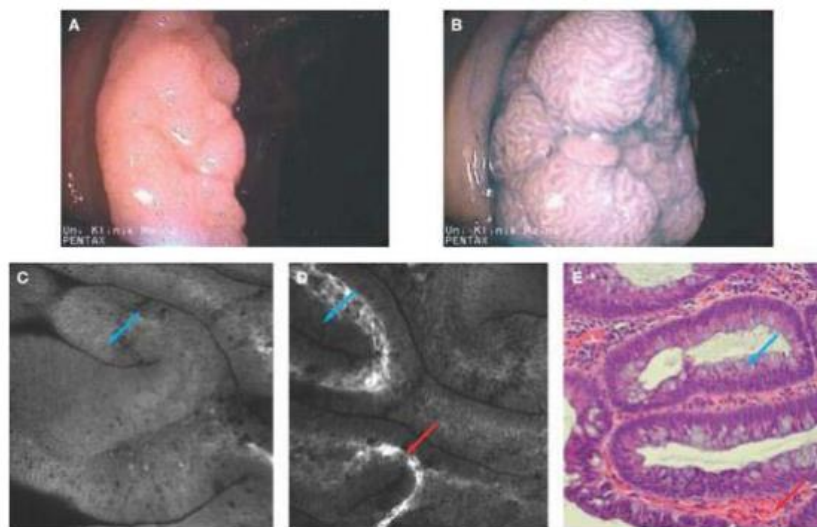


FIGURE 22. TUBULAR ADENOMA WITH LOW GRADE INTRAEPITHELIAL NEOPLASIA (A) ANALYSIS OF A COLONIC POLYP WITH WHITE-LIGHT ENDOSCOPY, (B) CHROMOENDOSCOPY, (C, D) FLUORESCIN-BASED CONFOCAL ENDOMICROSCOPY IN DIFFERENT IMAGING DEPTHS AND (E) FINAL HISTOLOGY. CHROMOENDOSCOPY HIGHLIGHTS SURFACE ARCHITECTURE WITH TUBULAR STAINING PATTERN. ENDOMICROSCOPY OF THE SURFACE SHOWS CHARACTERISTIC TUBULAR CELLULAR AND TISSUE ARCHITECTURE (C, BLUE ARROW). AT A DEPTH OF AROUND 150 MM, SUBEPITHELIAL CAPILLARIES BECOME VISIBLE (D, RED ARROW). FINAL HISTOLOGY (E) CONFIRMS THE PRESENCE OF TUBULAR ADENOMA (BLUE ARROW) WITH LOW-GRADE INTRAEPITHELIAL NEOPLASIA (RED ARROW).

Chapter 5 - A Novel Endoscopic Spectral Imaging Platform Integrating K-Means Clustering for Early and non-Invasive Diagnosis of Endometrial Pathology

Introduction

As discussed in chapter 4, after several decades of technology and application development, endoscopy has been established as an indispensable diagnostic tool to a variety of internal medicine fields. However it has been widely recognized that there is significant room for improvement mainly through the merging of endoscopy with novel and advanced optical imaging methods and technologies. These include confocal imaging (CI), optical coherence tomography (OCT) and spectral imaging (SI) [49]. CI and OCT with or without contrast enhancing agents, provide histological information in vivo for the very small tissue area. Spectral imaging provides, in principle, information for a much larger tissue area, which is essential in the clinical practice. Integrated to endoscopy, this imaging modality provides enhanced visualization of several invisible features of diagnostic importance.

There has been a considerable effort towards the integration of general purpose tunable filter technologies for enabling endoscopic spectral imaging. These include revolving discrete filter arrangements known as NBI, liquid crystal tunable filters (LCTFs), acousto-optical tunable filters (AOTFs) and Michelson interferometers [50]. Although the last three approaches can provide complete spectrum, they suffer from several limitations, which make them suboptimal solutions for endoscopy. Particularly, LCTFs are polarization dependent electro-optic devices with a poor light throughput being approximately 30%. AOTFs produce blurry images due to second order harmonics from the acoustic driver. The operating wavelength range of both AOTFs and LCTFs is limited to either the visible or to the NIR spectral range, requiring the interchange of different modules if one wants to cover the entire sensitivity spectral range of the silicon based imaging sensors (CCD and CMOS). Additionally, the full width half maximum (FWHM) of these tunable filters varies significantly together with the light throughput across the operating wavelength range, which makes their calibration cumbersome. These technical shortcomings of tunable filter technologies together with their relatively high cost comprise a barrier to their adoption in the clinical research and diagnosis. This barrier becomes even higher when their integration to endoscopy is attempted with the main problems, being the very low light throughput of endoscopes and especially of the thin ones (2-4 mm). For this reason, simplified and rather trivial solutions have been employed instead, which allows for only a partial exploitation of the diagnostic potential of SI. The basic representative of this class of instruments is the so-called Narrow Band Imaging (NBI) endoscopy. NBI

was developed primarily for enhancing the visualization of mucosal microvasculature and to identify vascular alterations indicative of pathologic conditions [51]. It is based on the simple interchange of two (415nm, 540nm) or three band-pass filters in front of a white-light source, which is coupled with the illumination path of the endoscope. This discrete, band-pass light-filtering arrangement produces a higher contrast between vascular structures and the surrounding mucosa [52]. Higher contrast is obtained by exploiting the existing light-absorption differences between these tissues, which are maximized within predetermined wavelength ranges. However, the provided enhancement, although useful in some cases, it is of limited diagnostic importance. This is because the development of consensus regarding the predictive value of the various vascular patterns is still pending [53]. The collection of a full spectral cube remains much more valuable than simply inspecting discrete spectral bands. This is because two-dimensional spectroscopy can provide NBI and on top of it “spectral signatures” of tissue lesions. The latter correspond to quantitative information with regard to biochemical and structural changes associated with several clinical conditions. This would enable the non-invasive, early detection and grading, while, at the same time, providing guidance for biopsy sampling, surgical treatment and follow up.

In an attempt to address this demand we present in this report an affordable, high-throughput and fast SI system that can be integrated to existing endoscopic workstations without changing significantly routine practices. This is because it provides both live color imaging and pixel by pixel spectral analysis. The system has been successfully adapted to a thin (3.5 mm) endoscope, which was used for inspecting the endometrium (hysteroscope). We also report our findings from the spectral measurement and analysis of the endometrium, which, to the best of our knowledge, are both presented for the first time. Particularly, the obtained millions of spectra were automatically clustered on the basis of their distinct spectral characteristics. This process revealed objectively that there are 5 to 6 distinguishable spectral clusters that may correspond to different medical conditions. The pilot clinical use of developed “Spectral Clustering” (SpeCL) endoscope in identifying and mapping pathologic conditions of the endometrium are finally presented and discussed.

5.1 Materials and methods

5.1.1 SPECL System Design and Set-Up

The SPECL hardware design was based upon a tunable wavelength light source and a camera operating in both color and monochrome modes. The tunable light source was built around a variable optical filter (VOF), which

has the property of transmitting a narrow spectral band of the incident light while all the other frequencies are blocked (figure 23). The center wavelength of the transmitted band changes continuously along its longitudinal axis and therefore it can act as a tunable filter when it is translated along this axis in front of a focused light source.

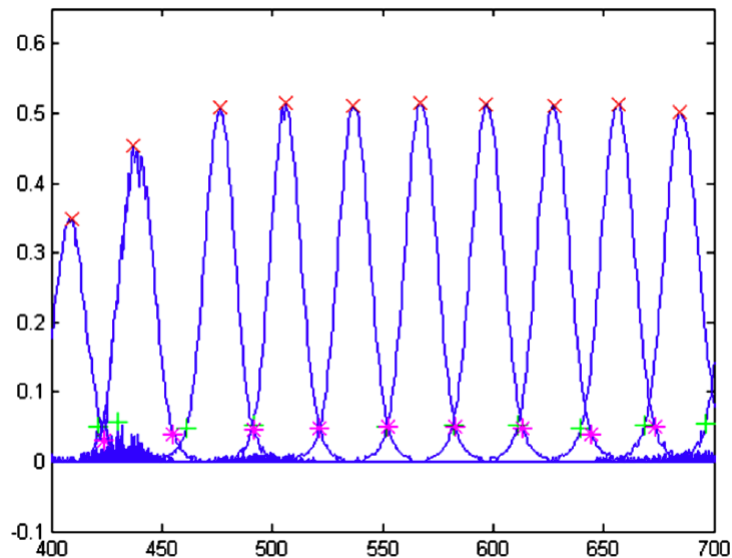


FIGURE 23. VOF'S TRANSMISSION SPECTRUM

The VOF operates in the spectral range 400-1000nm (Schott Veril) covering both the visible and the near infrared bands. It is quite convenient that this wavelength range matches the sensitivity range of the silicon-based imaging sensors. As discussed in the introduction, the wide operation spectral range of VOF improves its competitiveness as compared with the AOTFs and LCTF. Fig. 24 illustrates the block diagram of the SPECL endoscope. The VOF was mounted onto a motorized linear translation stage with about 160 mm stroke. A unipolar stepper motor was used, which is a robust closed loop control system for ensuring high positioning accuracy. The linear motion of the filter is controlled with the aid of an in-house built electronic unit, which is interfaced with a personal computer via USB 2.0 port. The unit has been built around the AT mega 162 (Atmel), low-power 8-bit microcontroller, which is based on the AVR enhanced RISC architecture. The light source is a Xenon bulb (150 W), which is focused onto the VOF's surface with the aid of a parabolic mirror. An electronically controllable mechanical iris and a cold mirror system are interposed in the light path, both filtering the beam before it reaches the VOF. This is done for minimizing the risk of thermal damaging. Actually, the dichroic mirror system combines two dichroic mirrors placed between the VOF and the iris, each one forming approximately at 45o angle with the VOF. The first dichroic mirror (Thorlabs DMSP805R), which transmits >90% in the spectral range 380-790nm and reflects > 90% in the spectral range 820-1300nm was

used to “cover” UV-visible part of the VOF. The second dichroic mirror (Thorlabs DMSP 1000R), transmits >90% in the spectral range 520-985nm and reflects > 90% in the spectral range 1020-1550 nm and it was used for protecting the red-NIR part of the VOF. The mirror set is moved together with the VOF and ensures that a great amount of the out of band energy of the light source is rejected (reflected), while at the same time the transmitted in band energy to the VOF remains substantially unchanged. The filter is removed away from the light spot when the user selects to switch the system to the color imaging mode. In this way, when the SPECL system operates in the color imaging mode, the VOF is cooled down to ambient temperatures. A color camera (Sony ICX674) with its infrared IR-cut filter removed, is used for capturing both color and monochrome (visible and near infrared) spectral images. The role of the camera’s IR-cut filter in ensuring correct, IR-free color reproduction and imaging is substituted by the extending part of first dichroic mirror, in the right side of the VOF (fig 24). Switching between spectral and color imaging is performed rapidly, through computer control, which toggles the camera’s output between the monochrome/color states. It also rotates the multihole-type iris so that more light passed through the iris holes when it is switched to operate in the SI mode.

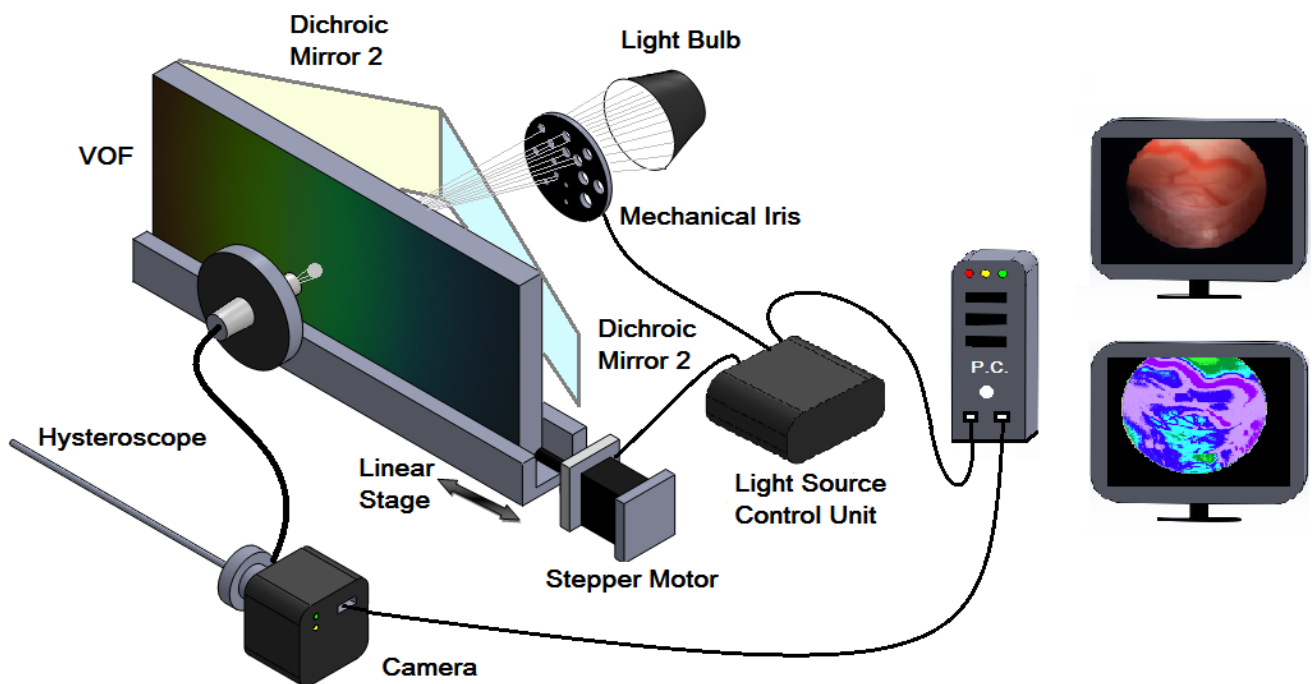


FIGURE 24 THE BLOCK DIAGRAM OF THE SPECTRAL CLUSTERING ENDSCOPE

5.1.2 SPECL System Operation-Spectral and Color Image Acquisition

Before acquiring spectral or color images, the SPECL system is calibrated. Calibration refers to both color and spectral imaging and it is performed by utilizing a reference sample with unity reflectance across the entire 400-1000nm spectral range. The system scans the sample step by step and the gray values of the sample serve as a feedback for the system to automatically regulate the sensor's exposure time and/or the light source's iris. Calibration process ends when the gray values reach a certain value for all spectral bands. When the user activates e.g. the spectral imaging procedure the VOF is moved to the corresponding position and the camera captures the image in a synchronized manner. Then, the filter is moved to the next position and the procedure continues until the entire set of the predetermined set of images is collected. Image capturing is performed with the exposure/iris settings as they have been determined during calibration and have been stored in a look-up-table for every tuning step.

With the SPECL system calibrated and switched to the color imaging mode, the operator inserts the endoscope into the hollow organ, while inspecting a color or a monochrome spectral image onto one of the two monitors of the system. Monochrome spectral image offers a similar to the NBI operations as it can be used for enhancing the observed contrast. The SPECL system integrates a fast spectral scanning procedure which operates as follows: With either real time color or spectral imaging, the operator locates a suspicious area to be analyzed. The system is then switched to the spectral scanning mode and ten seconds are given to the operator and to the patient to prepare and remain still. Next, and within two seconds, fifteen full resolution spectral images and one color image are collected and stored in system's hard drive. Upon completing the scanning procedure, the system switches back automatically to the real time color imaging mode. This stack of images (spectral cube) is then processed for detecting and correcting image misregistration problems and for calculating the cluster map image (CMI), based on the algorithms that will be described below. Calculations last for approximately two seconds and upon completing this second task, an artificial image is displayed on the second monitor. Each cluster in this image is represented with an artificial color for facilitating localization and identification of abnormal areas.

5.2 Clinical Evaluation

A set of 50 random patients were examined with our SIES in collaboration with the University Hospital of Ioannina. The patients were referred for hysteroscopy after previous ultrasonic check and/or prior doctor advice. During the examination, only doctors and medically trained personnel were present. The users of the

SIES were trained previously ex-vivo. In all cases spectral cubes were acquired from various areas of interest according to the physician's opinion. A total of 88 spectral cubes of diagnostic importance were finally selected. Inside that set, 5 spectral cubes were of undeveloped endometrium, 20 of polyps, 6 of hyperplastic endometrium, 6 of endometriosis, 2 of dysfunctional uterus bleeding (DUB) and 14 of various pathologies. The remaining spectral cubes were of normal endometrium. The total amount of data was more than 150 GB. Examples of acquired spectral cubes follow.

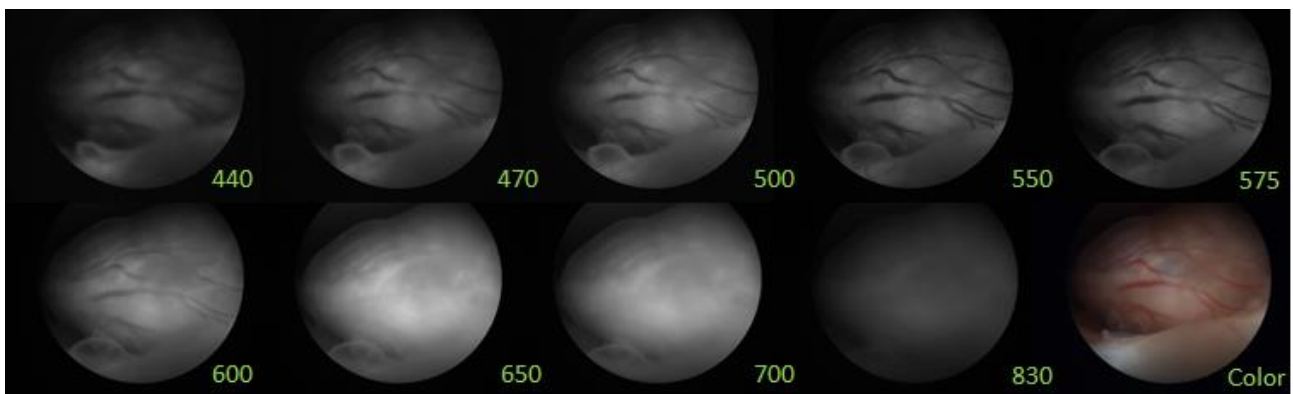


FIGURE 25. SPECTRAL AND COLOR IMAGES ACQUIRED FROM THE ENDOMETRIUM. NUMBERS AT THE BOTTOM RIGHT OF THE IMAGES REPRESENT THE CENTRAL WAVELENGTH. CLINICAL IMAGE: ENDOMETRIAL POLYP.

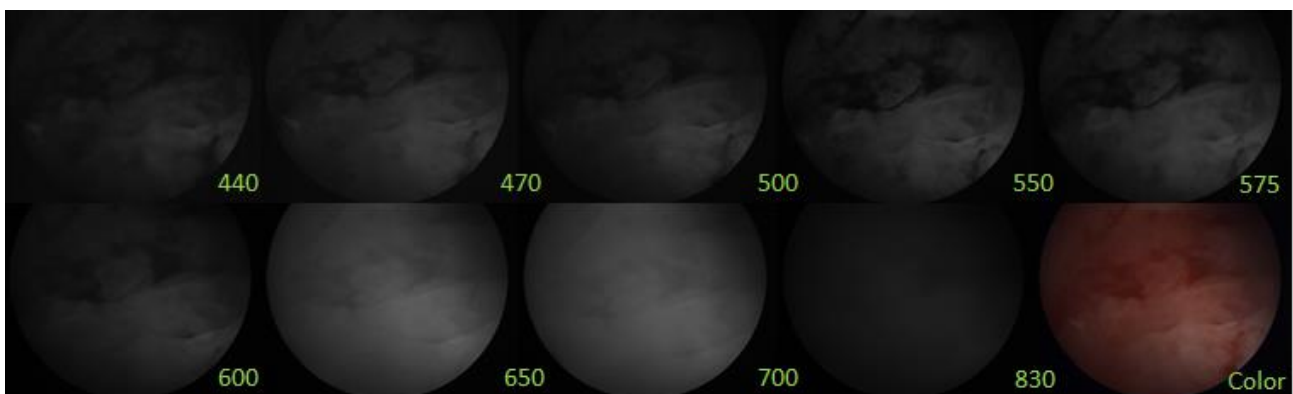


FIGURE 26. SPECTRAL AND COLOR IMAGES ACQUIRED FROM THE ENDOMETRIUM. NUMBERS AT THE BOTTOM RIGHT OF THE IMAGES REPRESENT THE CENTRAL WAVELENGTH. CLINICAL IMAGE: ENDOMETRITIS.

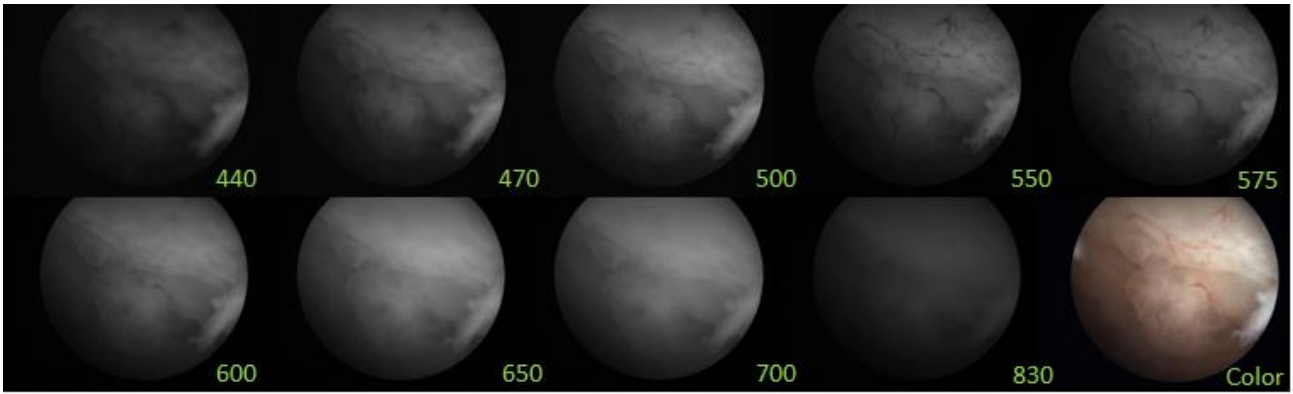


FIGURE 27. SPECTRAL AND COLOR IMAGES ACQUIRED FROM THE ENDOMETRIUM. NUMBERS AT THE BOTTOM RIGHT OF THE IMAGES REPRESENT THE CENTRAL WAVELENGTH. IN CLINICAL IMAGE: HYPERPLASTIC TISSUE.

5.2.1 Invisible Features observed with SPECL system

Invisible cyst

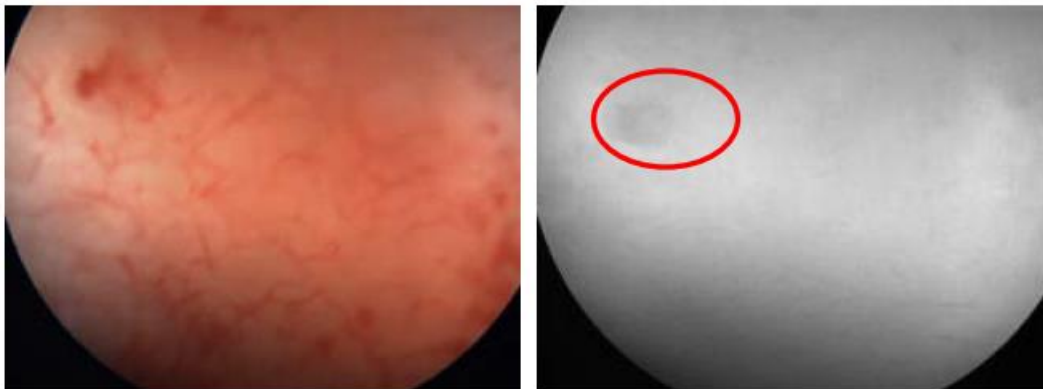


FIGURE 28. COLOR (LEFT) AND SPECTRAL IMAGE @ 675NM (RIGHT)

On the top left of the 675nm band image (marked) there can be seen a cyst which is invisible in the color image.

Micro vascular pattern

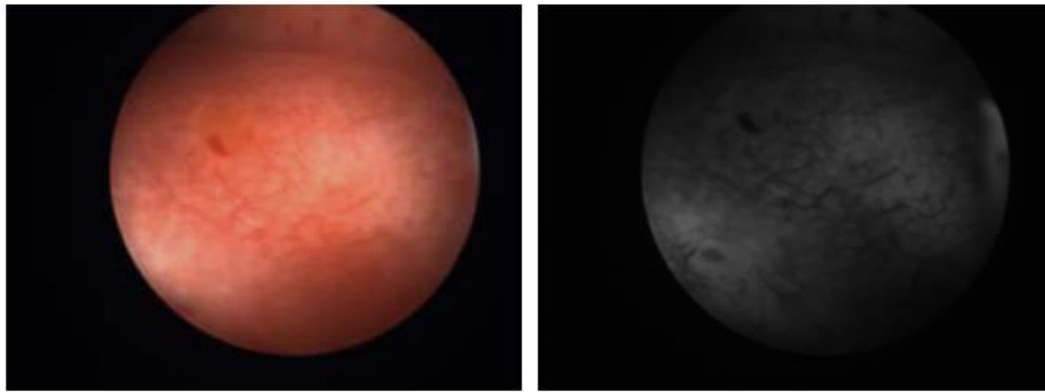


FIGURE 29. COLOR (LEFT) AND SPECTRAL IMAGE @ 575NM (RIGHT)

On the 575nm band image (right), the micro vascular pattern is very clearly distinguished, allowing the physician of better visualization of atypical blood vessel patterns, suspicious of neoplastic tumors growth.

Polyp's blood vessels



FIGURE 30. COLOR (LEFT) AND SPECTRAL IMAGE @ 575NM (RIGHT)

On the 575nm band image (right), the micro vascular pattern on the polyp can be clearly seen.

Deep Vessel



FIGURE 31. COLOR (LEFT) AND SPECTRAL IMAGE @ 550NM (RIGHT)

On the 550nm band image (marked), blood vessels are seen that are not visible on the color image.

Deep Vessel

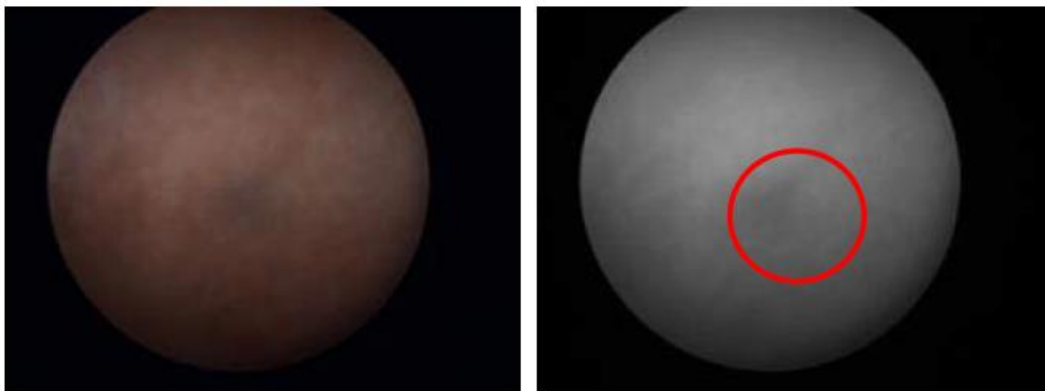


FIGURE 32. COLOR (LEFT) AND SPECTRAL IMAGE @ 700NM (RIGHT)

On the 700nm band image (markes), a shadow on its center can be seen, featuring probably a deeper vessel.

Vascular pattern

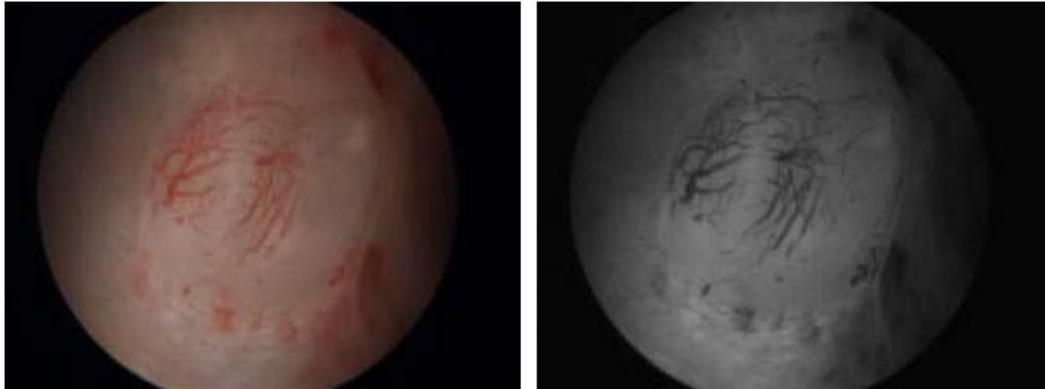


FIGURE 33 *FIGURE 5.8. COLOR (LEFT) AND SPECTRAL IMAGE @470NM (RIGHT)*

On the 470nm band image (right), the vascular pattern can be seen with greater contrast than in the color image and at the same time, the edges of the endometrium surface are enhanced.

Chapter 6 – Simultaneous spectral imaging using multiple band-pass filters

Introduction

In this chapter, it is described explicitly a method for simultaneous spectral imaging using multiple bandpass filters and standard color digital cameras. Also, a device able of previewing 6 spectral bands in real time is presented. This device will be miniaturized and integrated to a thin hysteroscope, able of performing real time, non-invasive diagnosis for pathological conditions in endometrium.

6.1. Hyperspectral Imaging using Multiple Band - pass Filters (MBPFs)

6.1.1 Capturing color information with imaging sensors

In most cases, color information is captured by standard digital cameras through color filter arrays (CFA), or color filter mosaic (CFM), i.e. a mosaic of tiny color filters placed over the pixel sensors of an imaging sensor. Color filters are needed because the typical photosensors detect light intensity with little or no wavelength specificity, and therefore cannot separate color information. Since sensors are made of semiconductors they obey to solid-state physics.

The color filters filter the light by wavelength range, such that the separated filtered intensities include information about the color of light. For example, the Bayer filter (figure 48), which is used in most single chip digital image sensors, gives information about the intensity of light in red, green, and blue (RGB) wavelength regions. The raw image data captured by the image sensor is then converted to a full-color image (with intensities of all three primary colors represented at each pixel) by a demosaicing algorithm which is tailored for each type of color filter. The spectral transmittance of the CFA elements along with the demosaicing algorithm jointly determine the color rendition. The sensor's passband quantum efficiency and span of the CFA's spectral responses are typically wider than the visible spectrum, thus all visible colors can be

distinguished. The responses of the filters do not generally correspond to the CIE color matching functions, so a color translation is required to convert the tristimulus values into a common, absolute color space.

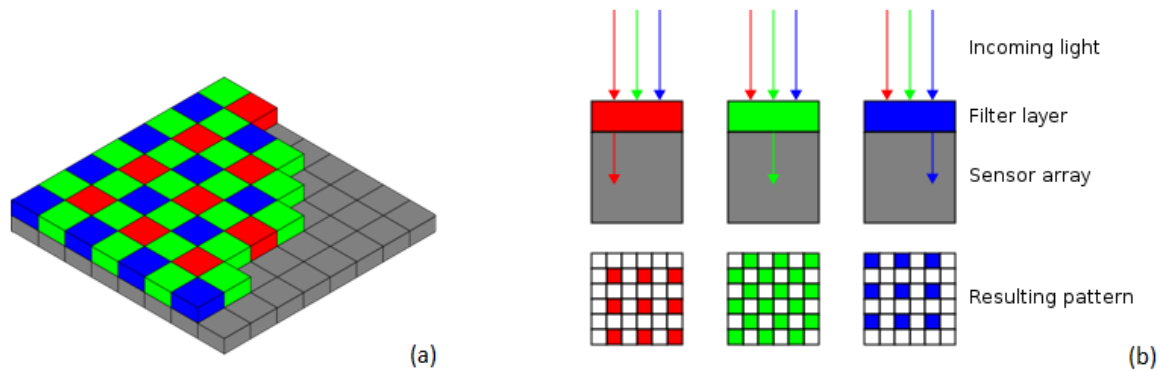


FIGURE 34.A: THE BAYER COLOR FILTER MOSAIC. EACH TWO-BY-TWO SUBMOSAIC CONTAINS 2 GREEN, 1 BLUE AND 1 RED FILTER, EACH COVERING ONE PIXEL SENSOR, PLACED ON A SQUARE GRID. 6.1.B: EACH COLOR MICROFILTER TRANSMITS SPECIFIC SPECTRAL BANDS.

In Table 2, a list of CFAs is presented. CFAs combined with imaging sensors are used in digital cameras, camcorders and scanners to create digital images. Each CFA has a different relative spectral response, depending on the micro-color filters that are used and modify the spectral response of the camera (figures 49 & 50).

A full color image is reconstructed from the incomplete color samples output from an image sensor overlaid with a CFA. Also known as CFA interpolation or color reconstruction, another common spelling is demosaicking. Most modern digital cameras acquire images using a single image sensor overlaid with a CFA, so demosaicking is part of the processing pipeline required to render these images into a viewable format. Many modern digital cameras can save images in a raw format allowing the user to demosaic it using software, rather than using the camera's built-in firmware.

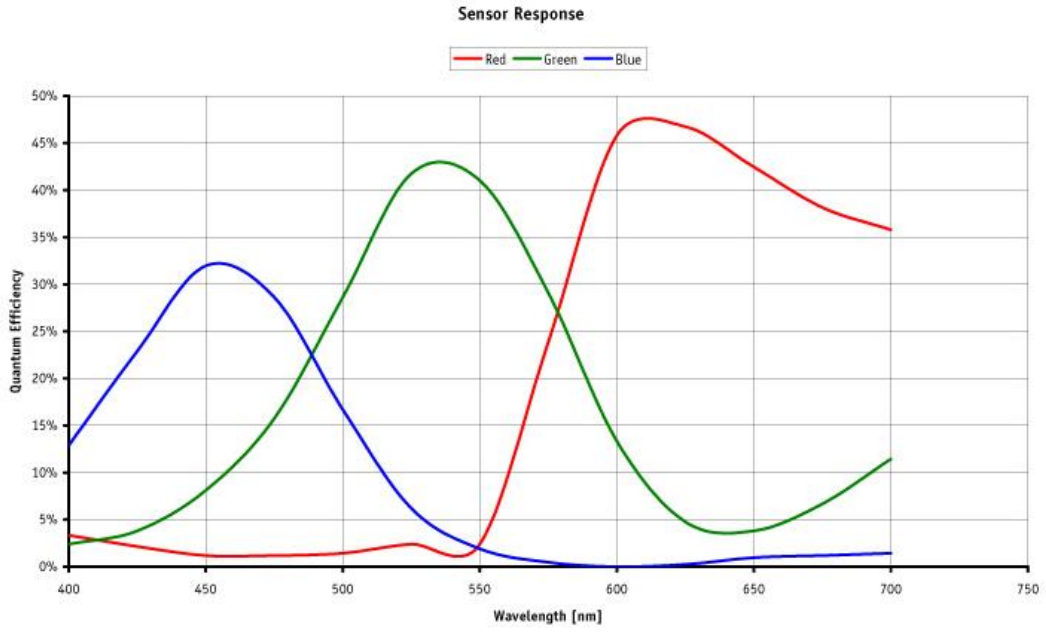


FIGURE 35. RELATIVE SPECTRAL RESPONSE OF A SONY, ICX445 CCD IMAGING SENSOR. A BAYER CFA IS USED.

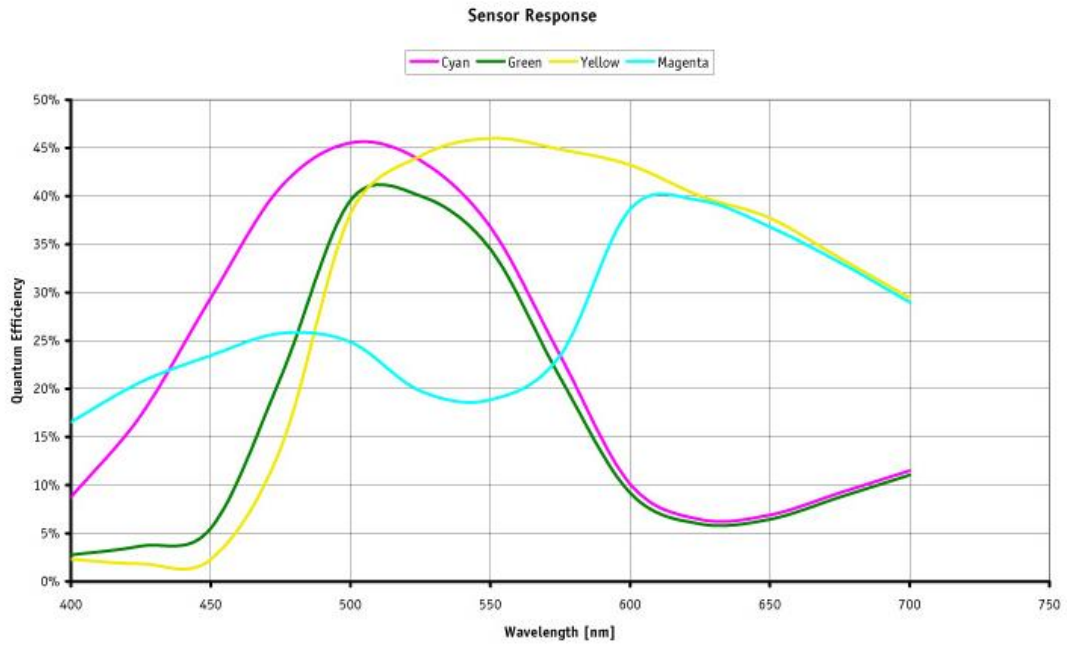


FIGURE 36. RELATIVE SPECTRAL RESPONSE OF A SONY, ICX419 CCD IMAGING SENSOR. A CMYK CFA IS USED.

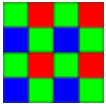
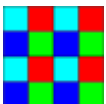
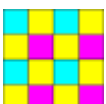
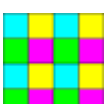
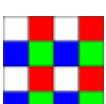
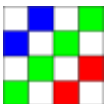
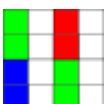
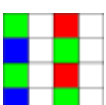
Pattern	Name	Description	Pattern size (pixels)
	Bayer filter	Very common RGB filter. With one blue, one red, and two green.	2x2
	RGBE filter	Bayer-like with one of the green filters modified to "emerald"; used in a few Sony cameras.	2x2
	CYYM filter	One cyan, two yellow, and one magenta; used in a few cameras of Kodak.	2x2
	CYGM filter	One cyan, one yellow, one green, and one magenta; used in a few cameras.	2x2
	RGBW Bayer	Traditional RGBW similar to Bayer and RGBE patterns.	2x2
	RGBW #1	Three example RGBW filters from Kodak, with 50% white.	4x4
	RGBW #2		
	RGBW #3		2x4

TABLE 2 LIST OF COLOR FILTER ARRAYS.

6.1.2 Measuring the spectral sensitivity of a color camera manually

The relative spectral response of a camera was calculated by stimulating it with very narrow band illumination, of the same intensity at each wavelength, produced by a **monochromator**. This method is conceptually very simple and can be very accurate. The equipment is required to produce sufficiently intense narrow band illumination at uniformly spaced wavelengths. Various researchers have investigated methods for characterization which do not use such equipment [71], as this equipment is relatively expensive and not always readily available, but still these methods are liable to errors.

To measure the relative spectral response of a color CCD camera (Point Grey Research, DR2-13S2C-CS in our case), the following experimental setup was designed: A halogen lamp (Thorlabs OSL1-EC) with a fiber optic was coupled to a tunable diffraction grating monochromator (Optometrics, MC1-03), with a minimum tuning step of 0.2nm and 3.4nm FWHM (figure 51). The camera was focused at the exit slit of the monochromator, in a distance of 20cm. Between the camera and the monochromator, a cube beam splitter (Edmund Optics NT47009, 25mm, non polarizing) was mounted, splitting 50% of the monochromatic light to the camera and the other 50% to an optical power and energy meter (Thorlabs PM1000D). Through this setup, the output light from the monochromator was kept to a constant value ($3.5\mu\text{W}$) by adjusting the output intensity of the halogen lamp. This process should be done for almost every tuning step (which in our case was 5nm), as the transmittance of the monochromator and the emission spectra of the halogen source alter throughout their wavelength active range. The combination of the halogen lamp, the monochromator and the photometer produced a tunable wavelength light source with a flat response between 400 and 1000 nm.

In contrast to the human eye, CCD chips are also sensitive to near infrared light. In the case of color cameras this would lead to a predominance of red. An IR cut filter (figure 54) corrects this situation. However, cameras without IR cut filter provide more flexibility because they enable the users to apply their own filter depending on the particular requirements.

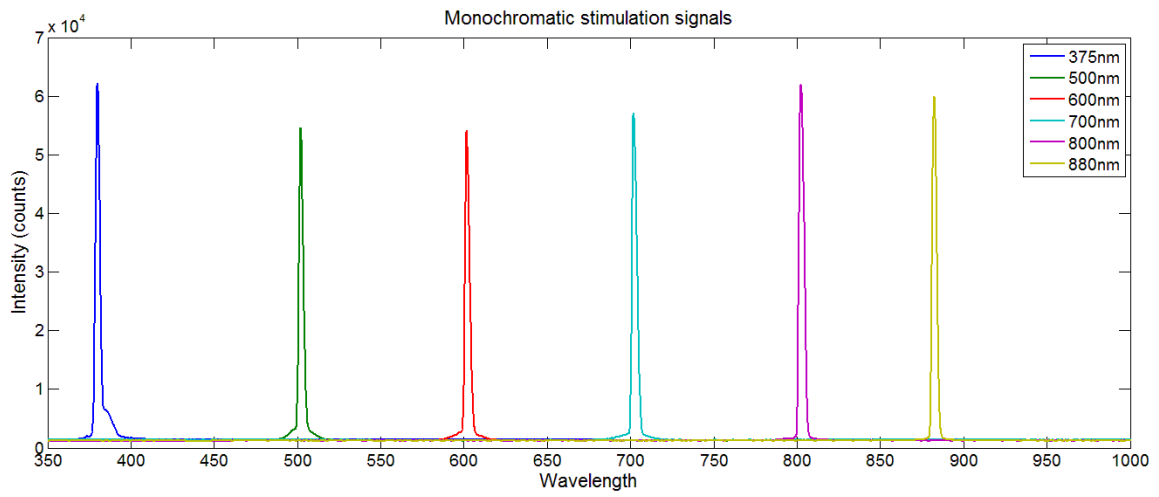


FIGURE 37. SAMPLE OUTPUT OPTICAL SIGNALS FROM A TUNABLE DIFFRACTION GRATING MONOCHROMATOR, MEASURED WITH A SPECTROMETER.

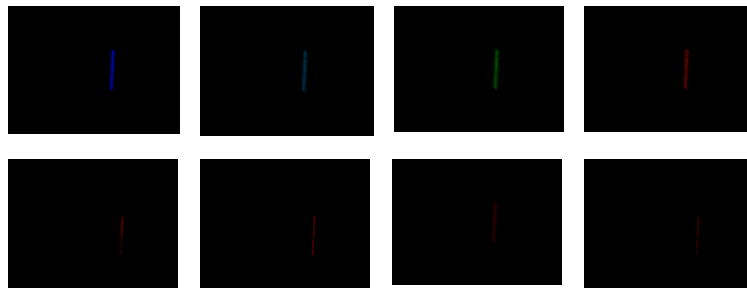


FIGURE 38. SAMPLE OUTPUT OPTICAL SIGNALS FROM A TUNABLE DIFFRACTION GRATING MONOCHROMATOR, CAPTURED WITH A DIGITAL CAMERA.

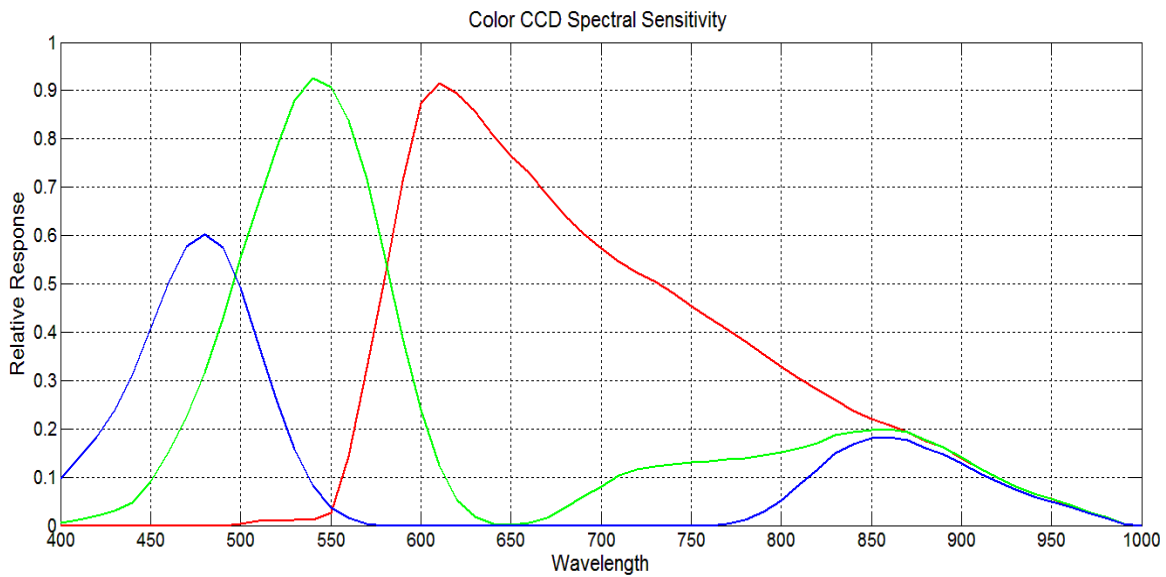


FIGURE 39. EXPERIMENTALLY MEASURED SPECTRAL SENSITIVITY OF A SONY ICX204AK CCD SENSOR FOR RGB CHANNELS RESPECTIVELY. CAMERA SETTINGS WERE SET AT THE DEFAULT VALUES.

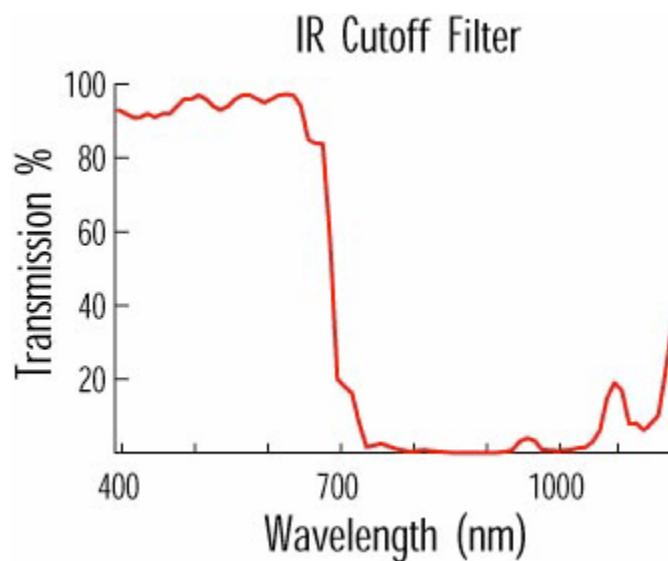


FIGURE 40. IR CUT-OFF FILTER. EDMUND OPTICS LTD, WWW. EDMUNDOPTICS.EU

6.1.3 Camera parameters – Maximizing the image quality

Image formation and quality, apart from the spectral characteristics of the imaging sensor, is also determined by several factors, such as illumination, lens and camera parameters. In the following matrix, basic camera parameters for optimal image quality are discussed.

Parameter	Determination
Shutter	Sensor's exposure time
Gain	Amplification of the sensor's output signal
Offset (Brightness)	Increase of the grey / color levels
Sharpness	Enhance blurred images
Gamma	Manipulation of the middle grey / color levels
Saturation	Adjustment of color saturation
Hue	Shift color values
White Balance	Adjust red and blue color channel amplification

TABLE 3 BASIC CAMERA SETTING PARAMETERS AND THEIR DEFINITIONS.

Controlling the white balance

White balance (WB) is a name given to a system of color correction to deal with differing lighting conditions (figure 53), describing how to manipulate the white balance of a color camera's Bayer tile pattern (e.g. R, G1, G2, B). Adjusting the white balance by modifying the relative gain of R, G and B in an image enables white areas to look "whiter". In principle, one wants to scale all relative luminances in an image so that objects which are believed to be neutral, appear so. If a surface with $R=240$ was believed to be a white object, and if 255 is the count which corresponds to white, one could multiply all red values by $255/240$. Doing analogously for green and blue would result, at least in theory, in a color balanced image. In this type of transformation the 3x3 matrix is a diagonal matrix.

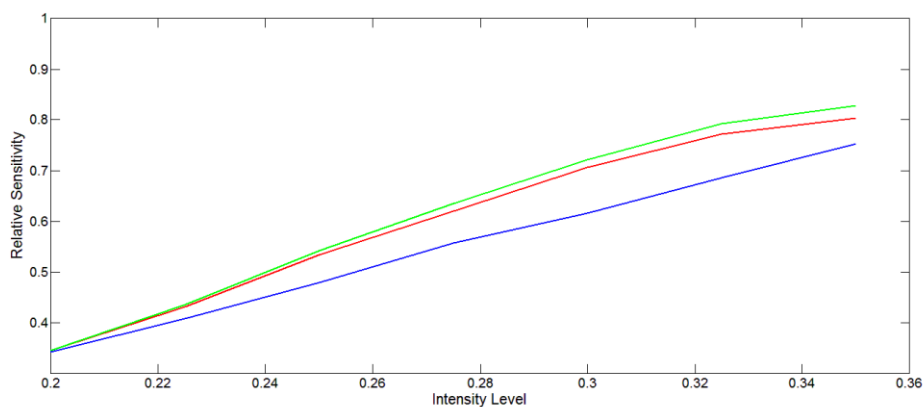
$$\begin{bmatrix} R \\ G \\ B \end{bmatrix} = \begin{bmatrix} 255/R'_w & 0 & 0 \\ 0 & 255/G'_w & 0 \\ 0 & 0 & 255/B'_w \end{bmatrix} \begin{bmatrix} R' \\ G' \\ B' \end{bmatrix}$$

where R , G and B are the color balanced red, green, and blue components of a pixel in the image; R' , G' and B' are the red, green, and blue components of the image before color balancing, and R'_w , G'_w and B'_w are the red,

green, and blue components of a pixel which is believed to be a white surface in the image before color balancing. This is a simple scaling of the red, green, and blue channels, and is why color balance tools in Photoshop and the GIMP have a white eyedropper tool. It has been demonstrated that performing the white balancing in the phosphor set assumed by sRGB (standard RGB color space) tends to produce large errors in chromatic colors, even though it can render the neutral surfaces perfectly neutral (figure 55).

In most digital cameras WB operation is performed through taking some subset of the target image and looking at the relative red to green and blue to green response. The general idea is to scale the gain of red and blue channels, so that the response is 1:1:1. For example, if the average pixel on the target was 222 (R), 232 (G), 236 (B) then all the reds should be scaled up by $232/222$ and the blues down by $232/236$ [WB2].

Practically, the most accurate and stable way to perform a white balance calibration is achieved as follows: The camera is focused to a white calibration card, typically made by Barium Sulfate (BaSO_4), which is the reflective standard. A light source illuminates the card at a constant intensity level. Many light sources (e.g. halogen lamps) need a warm up time to stabilize their color temperature. Then, the iris of the lens and the shutter time of the camera are set to a constant value and then the WB algorithm adjusts the gains of RGB channels to an equal outcome value. Through iris and shutter adjustment, the WB process should be performed to a relatively high value (e.g. 225 when using an 8-bit camera). This tactic assures that variations in the light source intensity levels will not affect the color calibration (figure 55). Also, it is wise to set the iris diameter to lower levels, in order to achieve high depth of field and the shutter time to medium to low levels, in order to avoid flickering in lower levels and not to sacrifice framerate at high shutter levels.



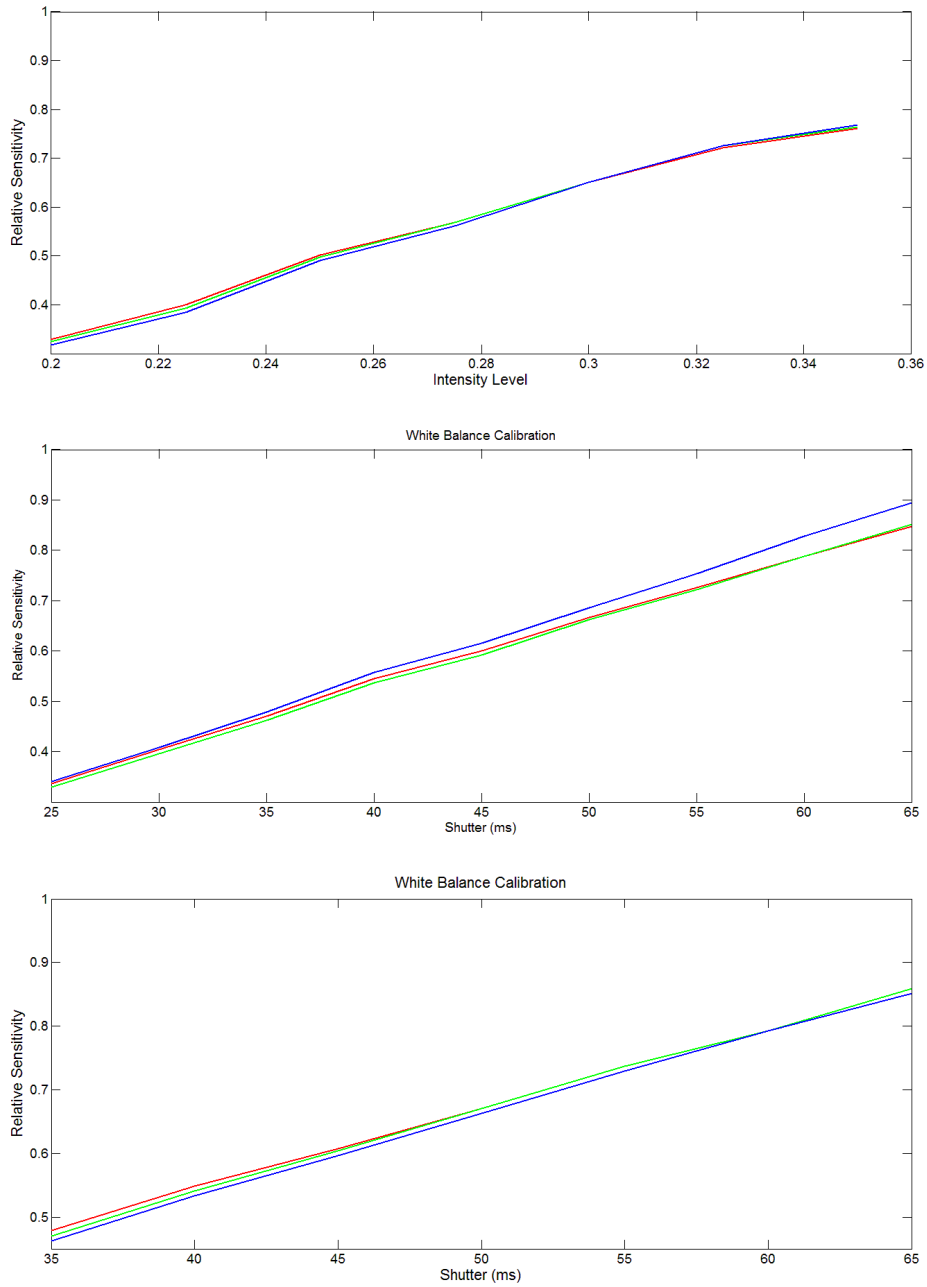


FIGURE 41. WHITE BALANCE OPERATION BY ADJUSTING THE LIGHT SOURCE'S INTENSITY LEVEL TO A LOW LEVEL (A) AND GRADUALLY INCREASING IT AND BY ADJUSTING THE LIGHT SOURCE'S INTENSITY LEVEL TO A HIGH LEVEL (B) AND GRADUALLY DECREASING IT. NOTICE THAT IN SECOND CASE, RGB VALUES ARE NOT AFFECTED BY THE VARIATIONS OF THE LIGHT SOURCE'S INTENSITIES.

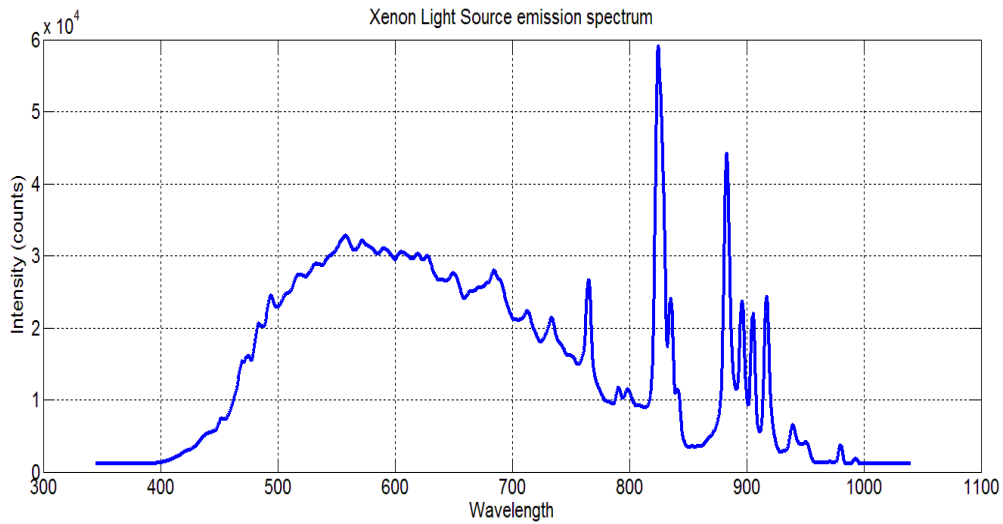
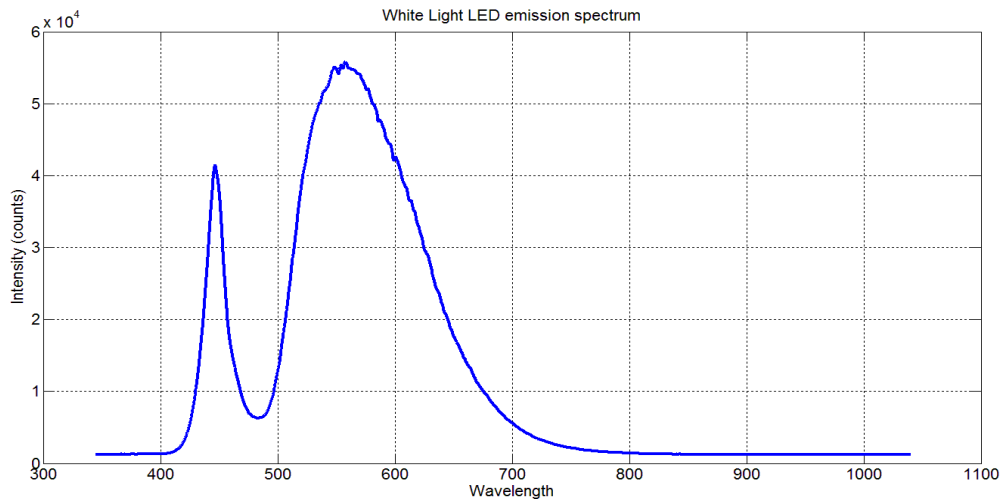
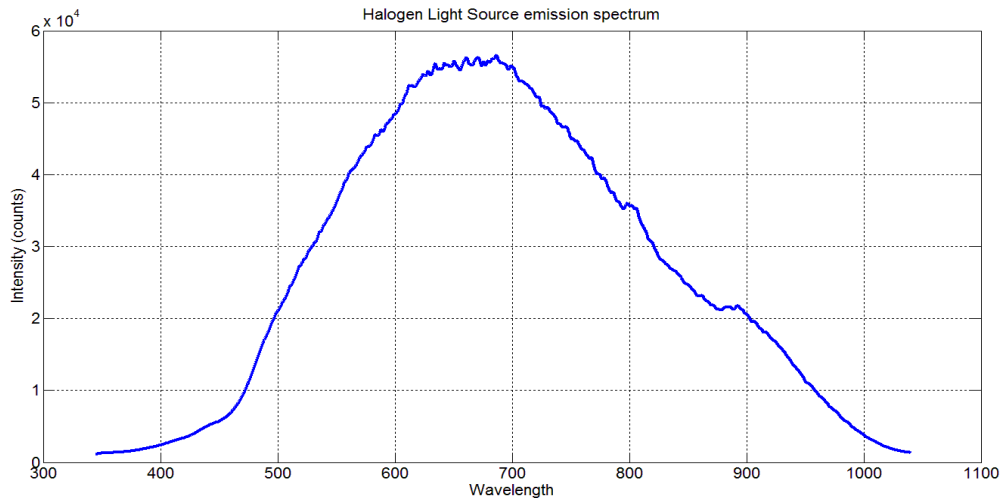


FIGURE 42. INDICATIVE ILLUMINATION SPECTRA OF A HALOGEN LAMP (A), A WHITE LIGHT LED (B) AND A XENON LAMP (C).

Through white balance and the global adjustment of the color channels of a camera, the overall mixture of colors in an image is changed and a color correction is performed, in order to compensate with the variable emission spectra of light sources that illuminate a scene.

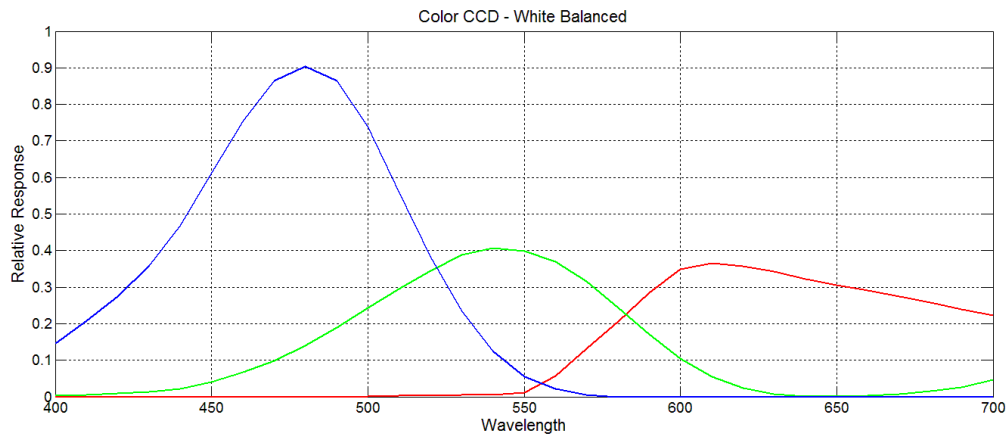


FIGURE 43. MODIFIED SPECTRAL SENSITIVITY OF A SONY ICX204AK CCD SENSOR BY THE WHITE BALANCE OPERATION. THE ILLUMINATING SOURCE WAS A HALOGEN LAMP.

6.2 Multi bandpass filters combined with color cameras

Multi band pass filters, i.e. filters that transmit light in several discrete narrow spectral bands, are widely used in fluorescence imaging applications as a means of rapidly identifying positively labeled multi-color samples. The filters are optimized to provide high transmission, steep edges and deep blocking for balance in contrast, brightness, and color representation. In this work, MBPFs are used in combination with color CCD cameras, which allows the acquisition of multiple spectral images at specified spectral bands.

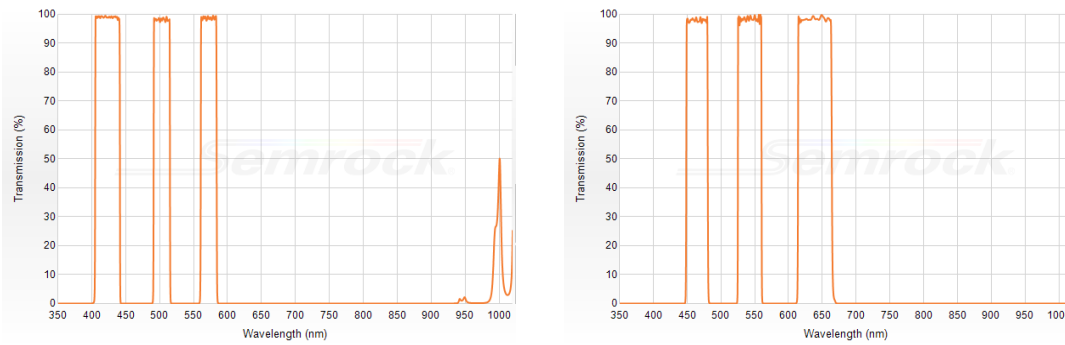


FIGURE 44.
TRANSMISSION
SPECTRA FOR
PRODUCTS FF01
422/503/572 (A)
AND FF01
464/542/639
(B), SEMROCK,

ROCHESTER, NY, WWW.SEMROCK.COM.

Multi band pass filters (MBPFs), i.e. filters that transmit light in several discrete narrow spectral bands (figure 58), are widely used in fluorescence imaging applications as a means of rapidly identifying positively labeled multi-color samples. The filters are optimized to provide high transmission, steep edges and deep blocking for balance in contrast, brightness, and color representation. In this work, MBPFs are used in combination with color CCD cameras and spectral unmixing algorithms, which allow the acquisition of multiple spectral images at specified spectral bands.

When using MBPFs in the visible spectrum, the out of band rejection might present leaks in the IR spectrum (figure 58a), thus, carefully selected, extra IR cut filters must be used. Also, by performing WB operation to sensors coupled with MBPFs, the spectral sensitivity of the sensor is modified twice, once from the illumination source used and again by the MBPF transmittance. For example, in figure 57, the spectral sensitivity of a color CCD sensor is presented, coupled with a Semrock 422/500/572 MBPF (figure 58) and illuminated by a halogen lamp (figure 56c). Notice the amplification on the red channel, as a result of the MBPF's very limited transmittance in the red bands.

6.2.1 Channel unmixing algorithm

When a triple bandpass filter, with central wavelengths λ_1 , λ_2 , λ_3 , is coupled to a Bayer tiled CCD, the sensitivity of each pixel, apart from the spectral characteristics of the Bayer pattern microfilters, is modified again by the transmittance characteristics of the filter (figure 57, table 2). Since RGB microfilters are approximately broad,

with each one covering a wide area of the active CCD sensitivity spectrum, when coupling a triple MBPF, each pixel will unevenly be sensitive to any of the three narrow spectral bands.

This fact implies that a pixel value for the e.g. Red channel will be a summation of captured photons in all three narrow spectral bands of the MBPF. Assuming that the spectral bands of the MBPF are located in the red, green and blue channel sensitivity areas of an optical sensor and that R_{Broad} , is the value of the R channel, then R_{Narrow} , R_{Green} and R_{Blue} , will be the R channel values recorded at the red, green and blue band of the MBPF. Making the same assumptions for the G and B channels, equation (1) derives

$$\begin{aligned}
 R_{Broad} &= R_{Narrow} + R_{Green} + R_{Blue} \\
 G_{Broad} &= G_{Red} + G_{Narrow} + G_{Blue} \\
 B_{Broad} &= B_{Red} + B_{Green} + B_{Narrow}
 \end{aligned} \tag{1}$$

The initial objective of this thesis was to decide if the above fact could lead to a system, where each one RGB channel of a color camera will acquire only one narrow spectral band, after performing an unmixing algorithm that would eliminate the “crosstalking” of the channels in all MBPF’s bands. By advancing mathematically the equation (1), the above hypothesis is possible. Specifically, by noticing that for the e.g. red channel, the R_{Green} value, apart from being a fraction of R_{Broad} , is also a fraction of G_{Narrow} . This may be expressed as a ratio of the areas covered within the region of MBPF’s green spectral band between G_{Narrow} and R_{Broad} . This ratio is furthermore a weighted coefficient between R_{Green} and G_{Narrow} . So, by formulating mathematically the curves of the active spectrum of the RGB channels and by calculating their integrals at the MBPF’s bands, equation (1) leads to eq. (2).

$$\begin{aligned}
 R_{Broad} &= w_{RR} \cdot R_{Narrow} + w_{RG} \cdot G_{Narrow} + w_{RB} \cdot B_{Narrow} \\
 G_{Broad} &= w_{GR} \cdot R_{Narrow} + w_{GG} \cdot G_{Narrow} + w_{GB} \cdot B_{Narrow} \\
 B_{Broad} &= w_{BR} \cdot R_{Narrow} + w_{BG} \cdot G_{Narrow} + w_{BB} \cdot B_{Narrow}
 \end{aligned} \tag{2}$$

Converting these 3 equations system to matrix form, we have:

$$\begin{bmatrix} R_{Broad} \\ G_{Broad} \\ B_{Broad} \end{bmatrix} = \begin{bmatrix} W_{RR} & W_{RG} & W_{BR} \\ W_{GR} & W_{GG} & W_{BG} \\ W_{BR} & W_{BG} & W_{BB} \end{bmatrix} \cdot \begin{bmatrix} R_{Narrow} \\ G_{Narrow} \\ B_{Narrow} \end{bmatrix} \quad (3)$$

or

$$\begin{bmatrix} R_{Broad} \\ G_{Broad} \\ B_{Broad} \end{bmatrix} = W \cdot \begin{bmatrix} R_{Narrow} \\ G_{Narrow} \\ B_{Narrow} \end{bmatrix} \quad (4)$$

where W is the weight matrix, R_{Broad} , G_{Broad} , B_{Broad} , are the signal values of the light intensities as it is recorded by a color sensor and R_{Narrow} , G_{Narrow} , B_{Narrow} are the actual spectral band light intensities, before light reaches the sensor's surface. Since "broad" signals are known and W matrix can be calculated as it described in subchapter 2.2.1, then spectral intensities of the "narrow" signals can be calculated by a matrix inversion:

$$\begin{bmatrix} R_{Narrow} \\ G_{Narrow} \\ B_{Narrow} \end{bmatrix} = W^{-1} \cdot \begin{bmatrix} R_{Broad} \\ G_{Broad} \\ B_{Broad} \end{bmatrix}$$

This process enables the concurrent acquisition of any three spectral bands, by using a triple MBPF and an ordinary color camera. This setup may be expanded to the concurrent capturing of four spectral bands, by using CMYG color cameras and quadruple MBPFs. Also, with the use of optical dispersing elements, more than one cameras can be used, to increase the number of the acquired spectral bands.

Optomechanical Engineering

Optomechanical engineering, as a subset of mechanical engineering, specializes in optical systems, which usually have much higher design and manufacturing specifications than most machinery. They often require submicron precision during design and manufacturing. In addition, materials that are used in optical systems, such as glass filters, tend to have unusual physical properties, regarding great sensitivity to heat tolerance and mechanical stress. For the described imaging device, a conceptualization and design of a precision two-CCD camera system should be developed, involving beam splitting elements, relay lens, triple band pass filters and

detachable x, y, z stages with micron mobility. The design was modeled using Solidworks 3D CAD design software and manufactured at a specialized in micromachining machinery. A complete model of the snapshot multispectral imaging device is shown in figure 59.

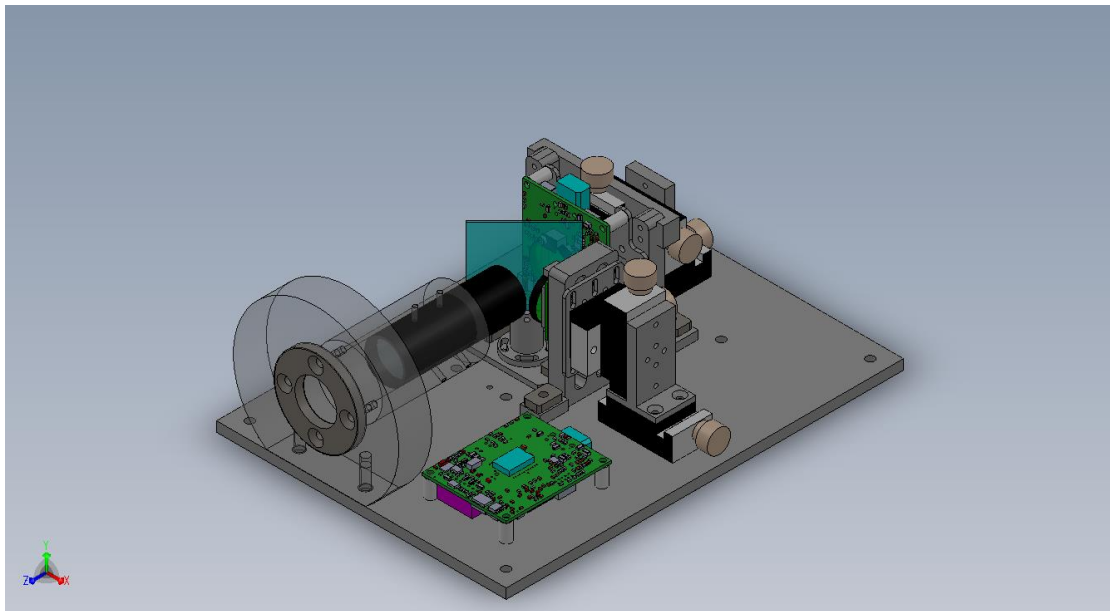


FIGURE 59: DIAGONAL VIEW OF THE EXPERIMENTAL SETUP

6.3 Results

Experimental performance is illustrated in Figure 60, presenting reflectance measurements versus wavelength. Each graph refers to a different color sample of the MacBeth checkerboard array target (figure 59). The chart's 24 color patches have spectral reflectances intended to mimic those of natural objects such as human skin, foliage, and flowers, to have consistent color appearance under a variety of lighting conditions and to be stable over time. Solid curves represent the reflectance spectra, and asterisks (*) represent the multispectral data obtained. The results indicate that the method enables simultaneous measurement of three spectral bands for a wide range of spectra. The reflection spectrum is successfully measured for all color samples with an average error of 6%. It can be seen that while most measurements offer a better match than

6%, there are still some inaccuracies observed. Moreover, the measured spectral bands might not be optimally located relative to the RGB sensitivity spectra.

These preliminary findings demonstrate that the developed method could be used for simultaneous multispectral imaging applications. The key advantage of the approach is the simple implementation in terms of hardware complexity that can correspondingly lead to low-cost applications. Further, this method could be used for a new generation of multispectral sensors based on the commonly used 3CCD sensor design, by using polychroic mirrors and color CCDs. Thus 12-band multispectral imaging sensors would be virtually the same size and weight as existing 3CCD sensors.

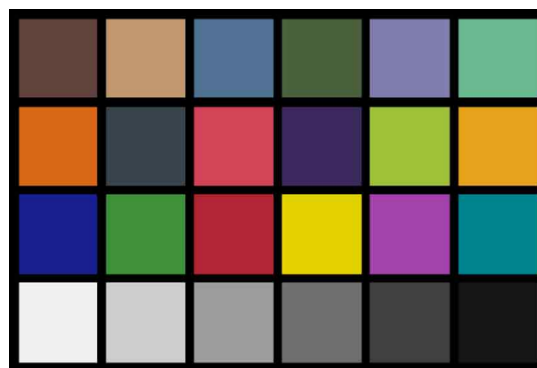
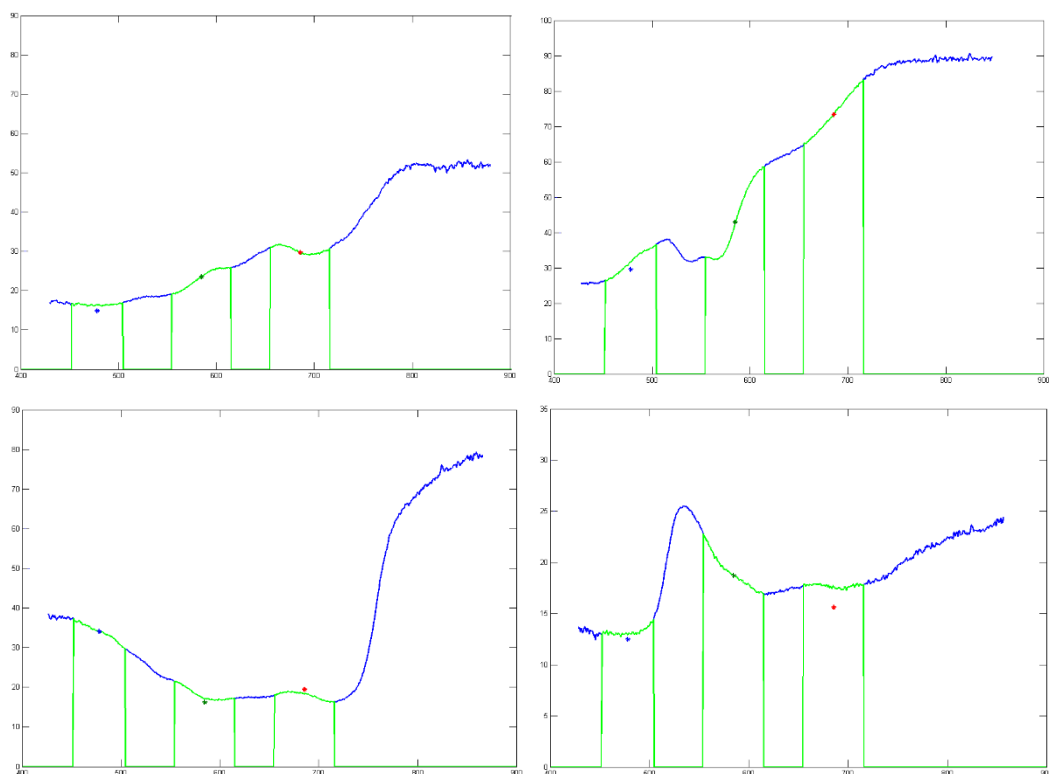
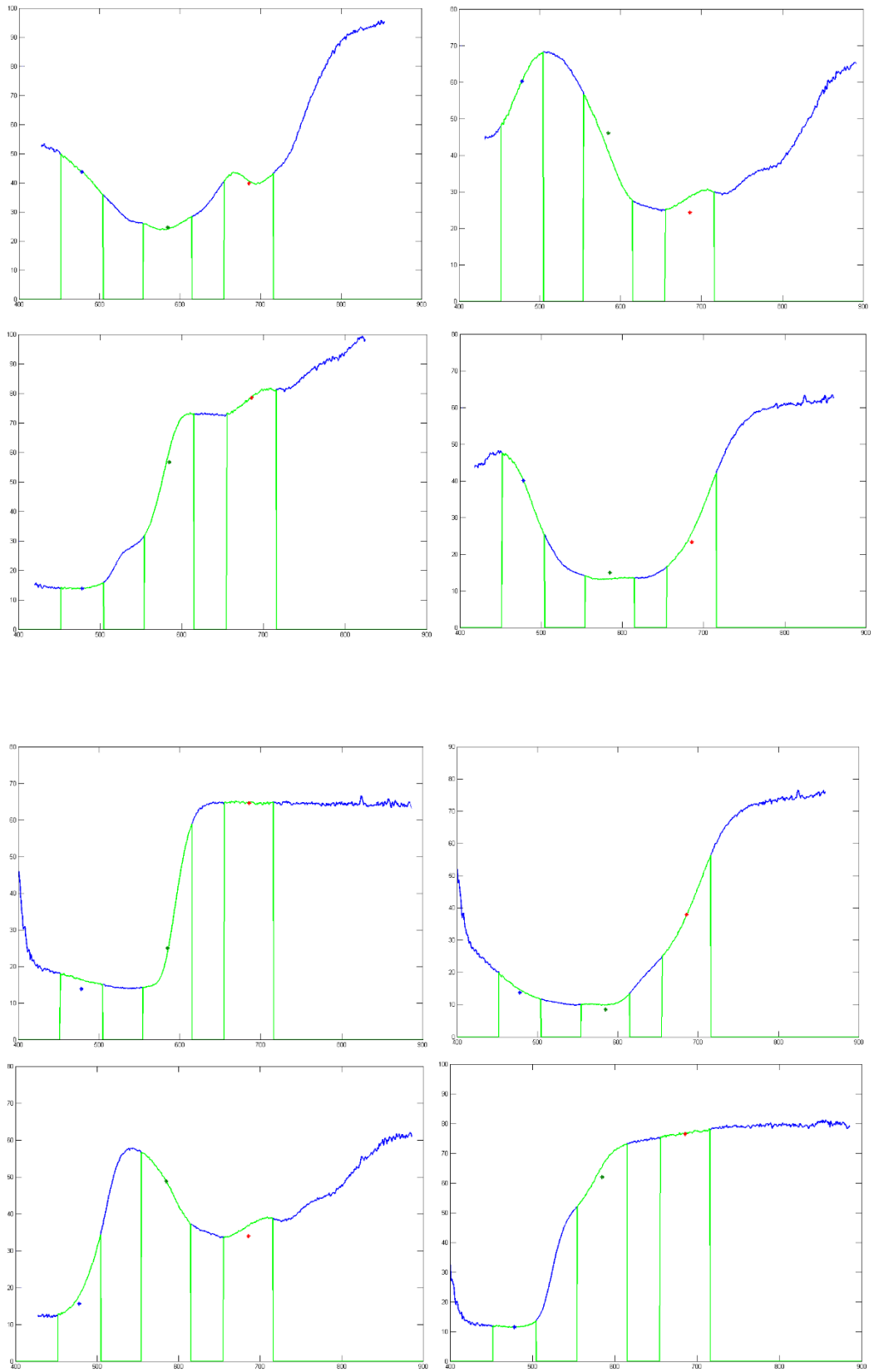
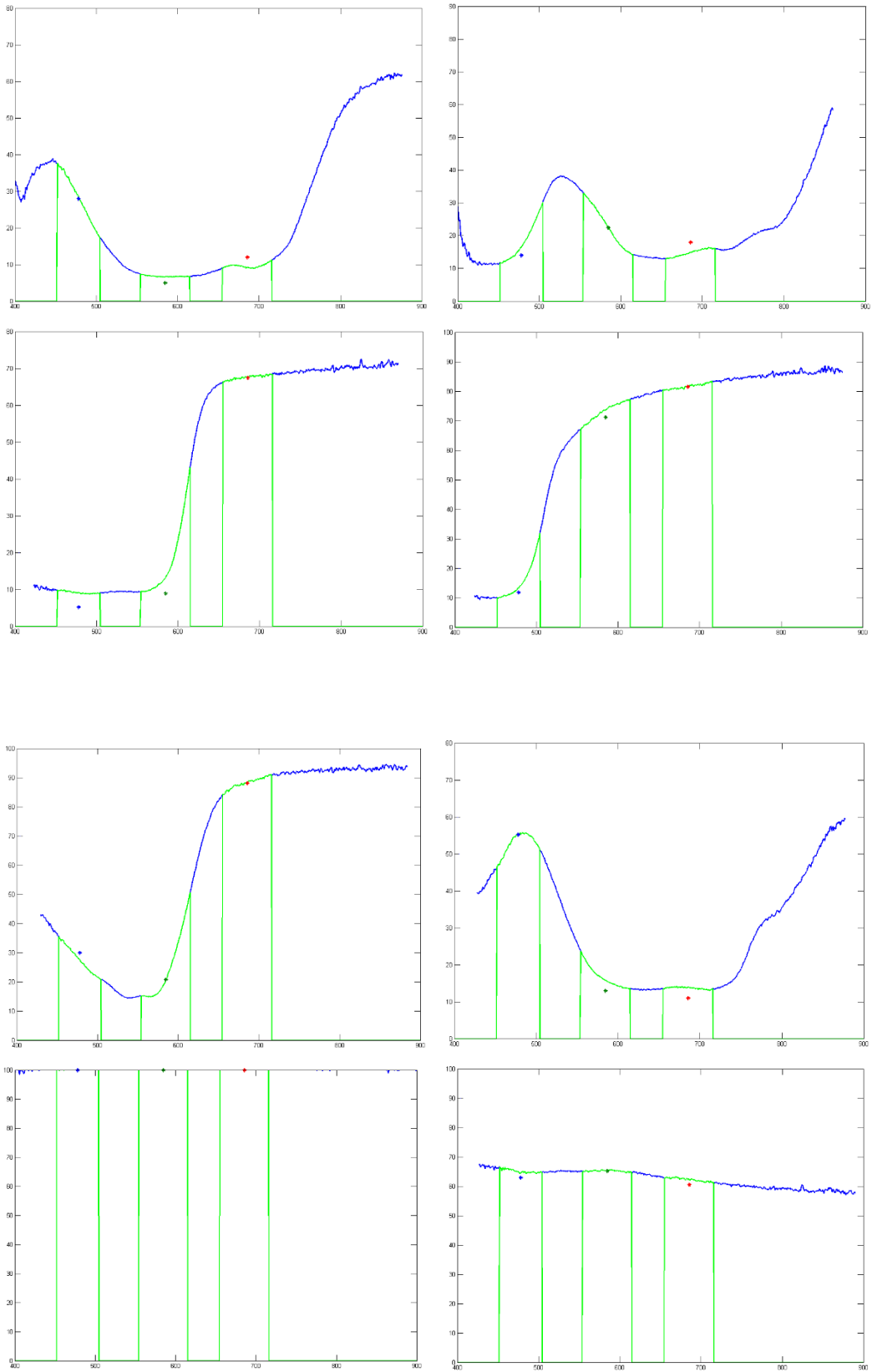


FIGURE 45 THE MACBETH COLORCHECKER CHART







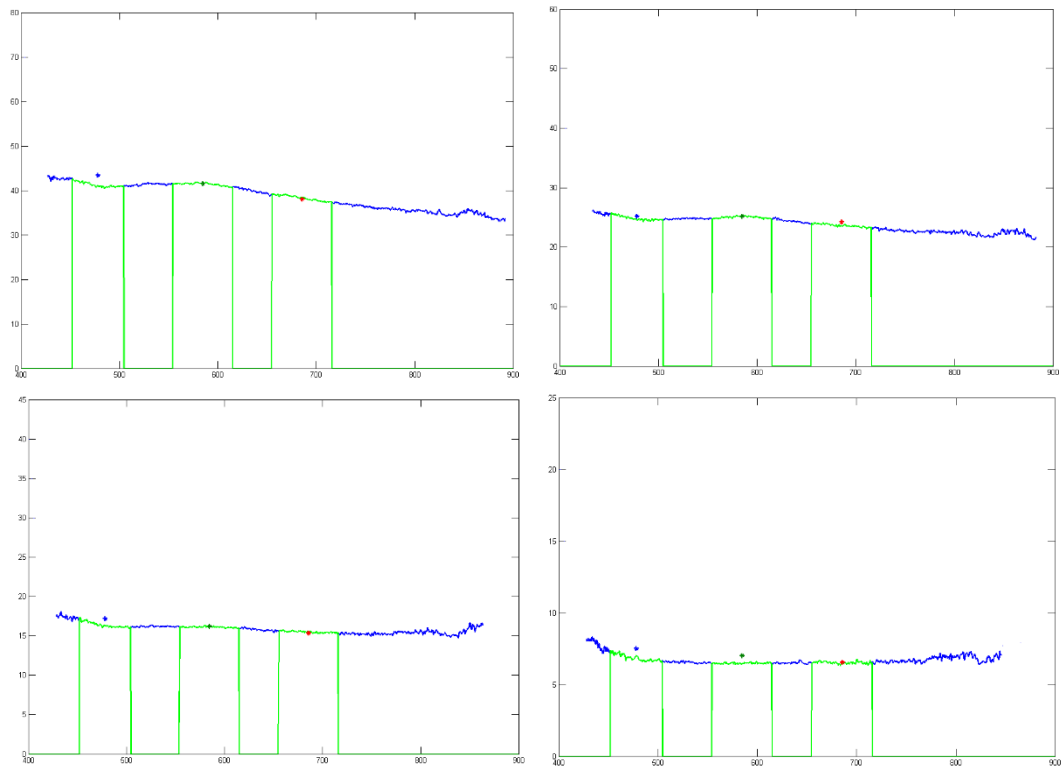
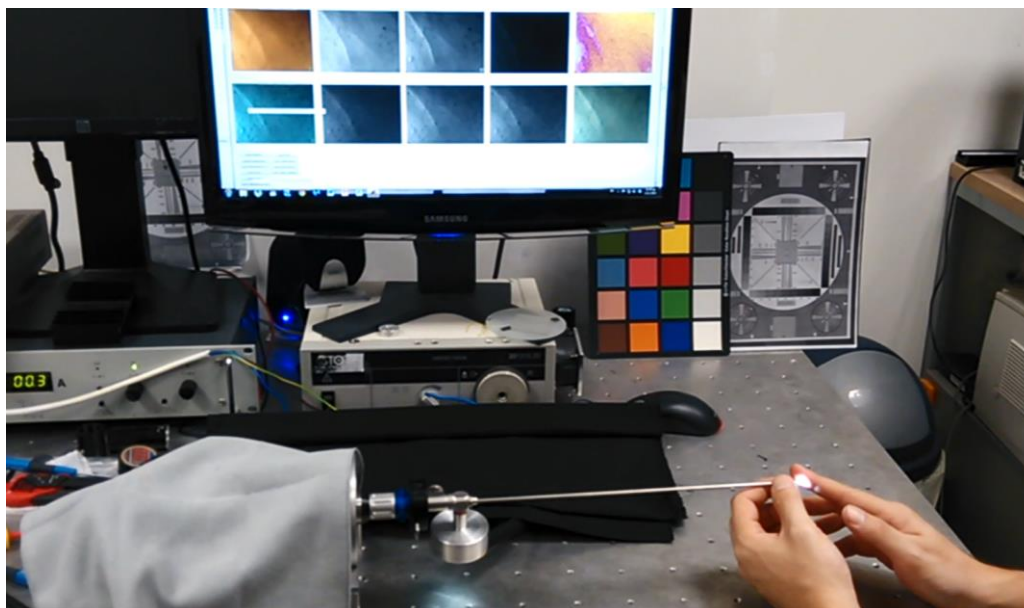


FIGURE 46. MEASUREMENTS OF REFLECTANCE OF THE CHECKERBOARD SAMPLES (ASTERISK) AND REFLECTANCE SPECTRA (SOLID CURVE). EACH GRAPH CORRESPONDS TO A DIFFERENT COLOR SAMPLE



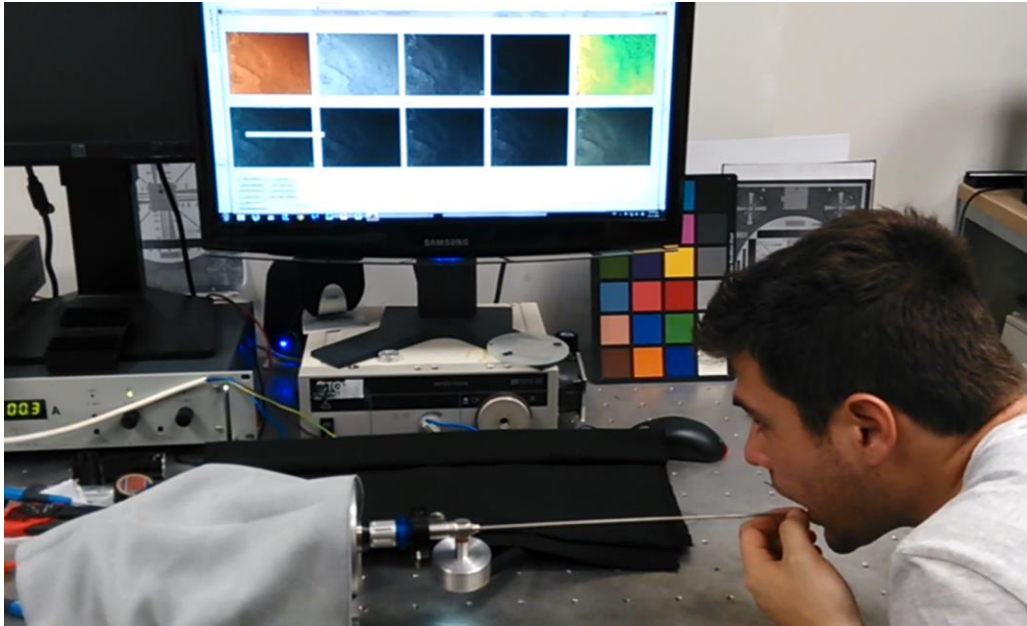


FIGURE 47. SNAPSHOT MULTISPECTRAL IMAGING DEVICE, CAPTURING 6 NARROW SPECTRAL BANDS SIMULTANEOUSLY, AT VIDEO RATES. (A) FINGERTIPS TISSUE INSPECTION. (B) LIPS TISSUE INSPECTION.

Chapter 7 - Clustering of Spectra Obtained from the Endometrium

Introduction

The SPECL endoscopic platform was used for examining the inner lining of the uterus, known as endometrium. In fact, the SPECL system enabled for the first time the collection of spectra from the endometrium corresponding to a wide range of clinical conditions. The examination of the endometrium is routinely performed with the aid of a very thin rigid endoscope (3.5 mm diameter), which is called hysteroscope. Hysteroscopy is performed for a variety of gynecological conditions, such as abnormal uterine bleeding (menorrhagia), infertility, polyps, fibroids, endometrial adhesions, uterine diaphragm, endometrial hyperplasia, cancer etc.

Although endometrial abnormalities are manifold that may be the etiology of several conditions ranging from infertility to cancer, all the existing diagnostic tests including transvaginal ultrasonography, sonohysterography and diagnostic hysteroscopy, have been proved to be just moderately accurate in detecting intrauterine pathology [54-55]. Very recently and in an attempt to improve the diagnostic performance of hysteroscopy, the NBI endoscopy technique has been used in examining the endometrium but with the limitations outlined in introduction [56].

The SPECL system was installed in the outpatient clinic of the Obstetrics and Gynecology department of the University of Ioannina, Ioannina, Greece. The SPECL's camera and tunable light source was coupled with a 3.5 mm Bettocchi Hopkins II hysteroscope (Karl Storz). A clinical study is currently underway with the purpose of establishing the spectral patterns of various pathologic conditions of the endometrium. The participants of the study are examined with the SPECL endoscope following the standard endoscopic procedures and guidelines. All women participating to the study have signed an informed consent and the ethics committee of the hospital has approved the study. During the preliminary phase of this large study, data were obtained from fifteen cases with different conditions (normal and pathologic). Particularly, these cases span a wide spectrum of conditions including normal, polyps, inflammation, abnormal uterine bleeding, endometrial hyperplasia and cancer (biopsy confirmed). By following the procedures described in paragraph II.B, 25 spectral cubes were collected from all these cases using the SPECL system.

It is easy to realize that it is impossible to visually analyze this huge number of spectra (2 million per spectral cube) and a number of further processing steps should be employed. The following sections will present an overview of the current workflow analysis, involving all the major steps of processing spectra for

misregistration problems, establishing a sampling rate (spatial and / or spectral dimension reduction) for almost real time analysis, image filtering, background removal, as well as clustering for estimating the number of the distinguishable spectral classes that might correlate with the normal/pathologic conditions of the endometrium.

7.1 Processing workflow of endometrium spectra

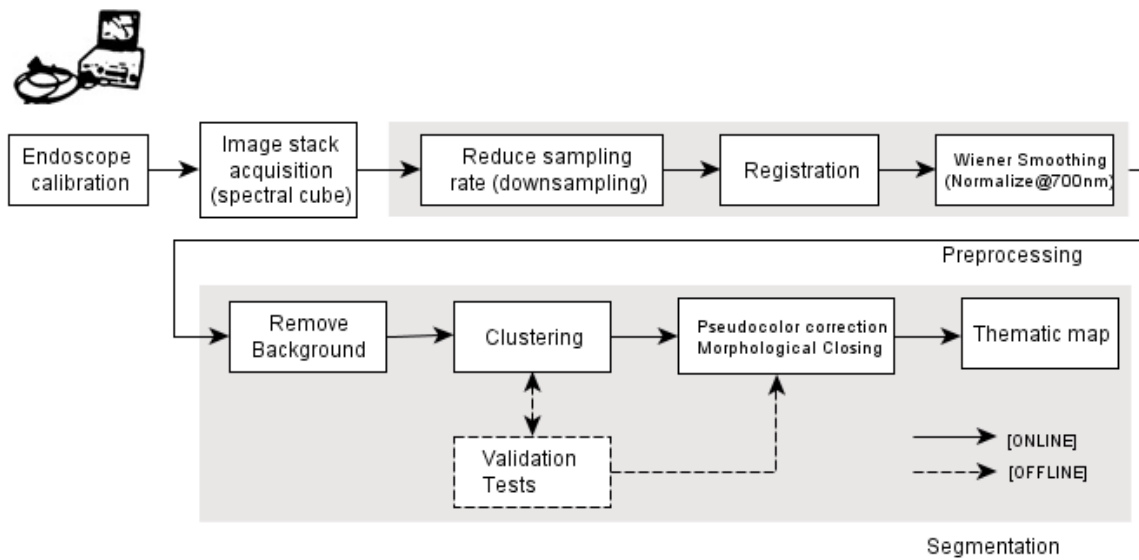


FIGURE 48. SPECL SYSTEM DATA WORKFLOW

1. Endoscope Calibration

System parameter(s) configuration (shutter, gain, etc), as previously discussed in Chapter 5.

2. Image stack acquisition

A 12-band spectral cube is acquired¹, saved and documented upon basic patient info. Other image and video operations are also provided, particularly recording video streams for specific timeframes (data are stored with *single* float precision), as previously discussed in Chapter 5.

3. Reduce sampling rate

In order to achieve (almost) real time performance with consumer based processing units (i5/i7 desktop computers), image down-sampling is required. Three approaches were tested:

- Block Processing,
- Resize Image(s),
- Sample pixels along horizontal and vertical axes at a constant period.

Block processing enables image processing in configurable blocks (3x3, 9x9, etc.) of pixels without altering the original (1280x1024) spatial dimensions of the spectral cube. While each block is processed sequentially, enabling operations on very large images, real benefits of this method account for systems with little memory and not for real time performance. Also accumulating X number of clustered blocks into a single map will increase both code complexity and process time. On the other hand, image resizing scales down the spatial dimensions of the spectral cube based on 3 different algorithms:

- Nearest-neighbor interpolation,
- Bi-linear interpolation, where the output pixel value is a weighted average of pixels in the nearest 2-by-2 neighborhood (averaging-based subsampling provides robustness² against noise),
- Bi-cubic interpolation, where the output pixel value is a weighted average of pixels in the nearest 4-by-4 neighborhood.

After clustering, regardless of the resizing algorithm, the resulting maps are visually almost identical, whereas in terms of performance, nearest-neighbor is the fastest method as it involves only pixel assignment without weighting. Also, image resizing causes an increasing fluctuation in the mantissa of each pixel value explaining

¹ @ 440, 470, 500, 525, 550, **575**, 600, 625, 650, **675**, 700 and 830 nm

the slight increase in the k-means processing time (segmentation). Nearest-neighbor interpolation is similar with a fast 2-dimensional sampling at a constant period achieving even lower processing times³:

CPU	i5@2.5GHz		i7@2.8Ghz	
	Reduce image stack (sec)	Segmentation (sec)	Reduce image stack (sec)	Segmentation (sec)
Block	-	-	-	-
BL	0.42	5.56	0.35	3.13
BC	0.48	5.76	0.37	3.32
NN	0.38	5.96	0.32	4.10
Sampling	0.29	3.95	0.23	2.33

TABLE 4. PROCESSING TIMES FOR SEVERAL DOWNSAMPLING TECHNIQUES.

Four times down-sampling (or even eight times) is possible without significant loss of information due to the endoscope's high camera resolution against the narrow optical field of view of the attached fiberoptic instrument.

4. Registration

Registration of a camera acquisition system relatively to an optical tracker is an important step for image guided applications. It is necessary in order to be able to compare data obtained from different modalities. Common causes of misalignment are patient's inadvertent movements during acquisition time and geometric distortions due to image capturing at different wavelengths by different sensors. The proposed endoscope system implements spectral imaging based on a linear variable filter avoiding major distortions due to different sensors. However, during screening tests a patient may experience discomfort or even pain, inevitably resulting in a series of movements (inadvertent or not). One way to perform registration consists on finding some common cues between the images in a spectral cube. Several approaches were tested:

- Control point registration [*user based*],
- Video stabilization using point feature matching [*feature based*],
- Automatic registration [*intensity based*]

³ Testing parameters are: downscale by 4 (1280x1024→320x256), wiener smoothing + remove background, k-means clustering (k=6) for an 11-dimensional single matrix i.e. 320x256x11 (images @830nm are omitted). Segmentation time is the **sum** of 4 consequent runs (for a single run elapsed time is <1 sec @i7).

In *Control Point Registration*, the user picks points in a pair of images that identify the same feature or landmark in the images. Then, a spatial mapping is inferred from the positions of these control points. Since it is not possible for the endoscope operator to simultaneously perform a medical examination and specify alignment points, this method was omitted. On the other hand, the problem of registration is similar to stabilizing a video that was captured from a jittery or moving platform. One way to stabilize a video is to track a salient feature such as edges or corners and use those anchors points to cancel out all perturbations relative to them. This approach automatically searches for the "background plane" in the image sequence, and uses its observed distortion to correct for camera motion. The stabilization algorithm involves two steps. First, we determine the affine image transformations between all neighboring frames of the sequence using a Random Sampling and Consensus (RANSAC) [57] procedure applied to point correspondences between two images. Second, we warp the video frames to achieve a stabilized video.

Using RANSAC method for estimating geometric transforms in computer vision

Random sample consensus, or RANSAC, is an iterative method for estimating a mathematical model from a data set that contains outliers. The RANSAC algorithm works by identifying the outliers in a data set and estimating the desired model using data that does not contain outliers. RANSAC is accomplished with the following steps:

1. Randomly selecting a subset of the data set
2. Fitting a model to the selected subset
3. Determining the number of outliers
4. Repeating steps 1-3 for a prescribed number of iterations

It is a non-deterministic algorithm in the sense that it produces a reasonable result only with a certain probability, with this probability increasing as more iterations are allowed. The algorithm was first published by Fischler and Bolles at in 1981. A basic assumption is that the data consists of "inliers", i.e., data whose distribution can be explained by some set of model parameters, though may be subject to noise, and "outliers" which are data that do not fit the model. The outliers can come, e.g., from extreme values of the noise or from erroneous measurements or incorrect hypotheses about the interpretation of data. RANSAC also assumes that, given a (usually small) set of inliers, there exists a procedure which can estimate the parameters of a model that optimally explains or fits this data.

Let p be the probability that the RANSAC algorithm in some iteration selects only inliers from the input data set when it chooses the n points from which the model parameters are estimated. When this happens, the resulting

model is likely to be useful so p gives the probability that the algorithm produces a useful result. Let w be the probability of choosing an inlier each time a single point is selected, that is,

$w = \text{number of inliers in data} / \text{number of points in data}$

A common case is that w is not well known beforehand, but some rough value can be given. Assuming that the n points needed for estimating a model are selected independently, w^n is the probability that all n points are inliers and $1 - w^n$ is the probability that at least one of the n points is an outlier, a case which implies that a bad model will be estimated from this point set. That probability to the power of k is the probability that the algorithm never selects a set of n points which all are inliers and this must be the same as $1 - p$. Consequently,

$$1 - p = (1 - w^n)^k$$

which, after taking the logarithm of both sides, leads to

$$k = \frac{\log(1 - p)}{\log(1 - w^n)}$$

This result assumes that the n data points are selected independently, that is, a point which has been selected once is replaced and can be selected again in the same iteration.

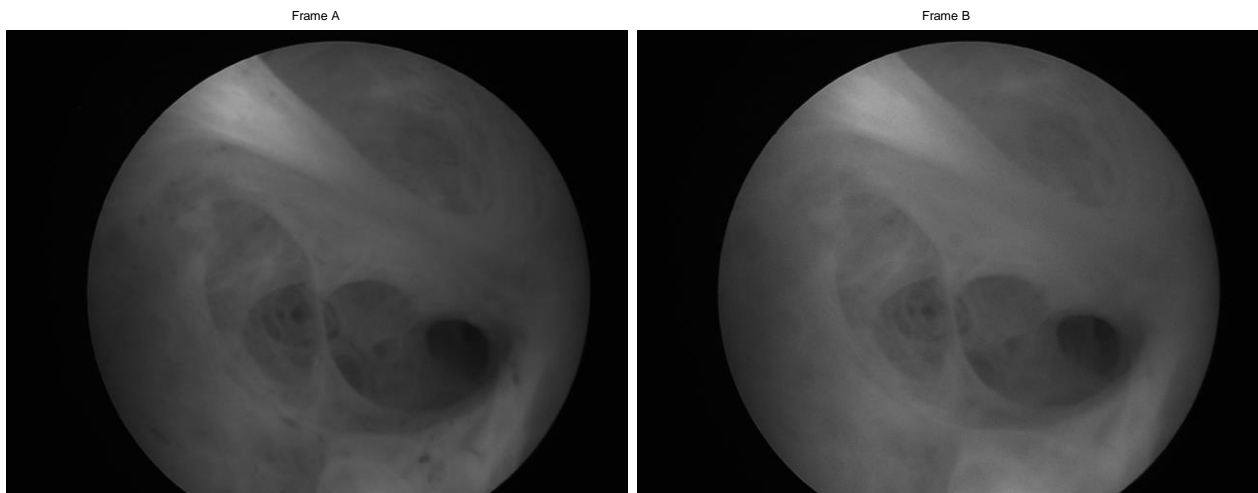
To gain additional confidence, the standard deviation or multiples thereof can be added to k . The standard deviation of k is defined as

$$SD(k) = \frac{\sqrt{1 - w^n}}{w^n}$$

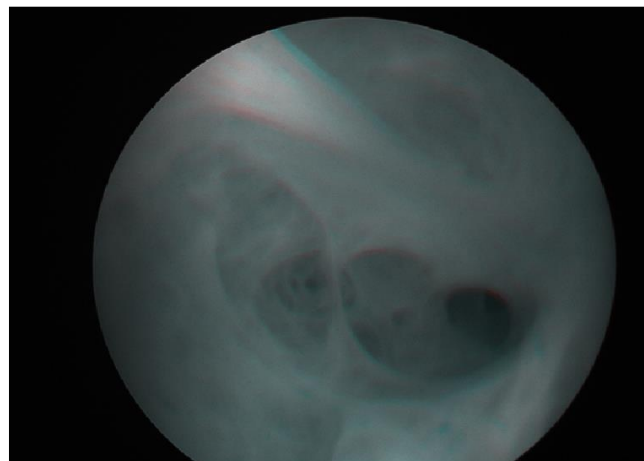
An advantage of RANSAC is its ability to do robust estimation of the model parameters, i.e., it can estimate the parameters with a high degree of accuracy even when a significant number of outliers are present in the data set. A disadvantage of RANSAC is that there is no upper bound on the time it takes to compute these parameters. When the number of iterations computed is limited the solution obtained may not be optimal, and it may not even be one that fits the data in a good way. In this way RANSAC offers a trade-off; by computing a greater number of iterations the probability of a reasonable model being produced is increased. Moreover, RANSAC is not always able to find the optimal set even for moderately contaminated sets and it usually performs badly when the number of inliers is less than 50%. Optimal RANSAC was proposed to handle both these problems and is capable of finding the optimal set for heavily contaminated sets, even for an inlier ratio under 5%. Another disadvantage of RANSAC is that it requires the setting of problem-specific thresholds. RANSAC can only estimate one model for a particular data set. As for any one-model approach when two (or more) model instances exist, RANSAC may fail to find either one. The Hough transform is one alternative robust estimation technique that may be useful when more than one model instance is present. Another approach for multi model fitting is known as PEARL, which combines model sampling

from data points as in RANSAC with iterative re-estimation of inliers and the multi-model fitting being formulated as an optimization problem with a global energy functional describing the quality of the overall solution.

- (1) *[Visualization] Produce a red-cyan color composite image to demonstrate the pixel-wise difference. There is obviously a vertical and horizontal offset between the two frames.*

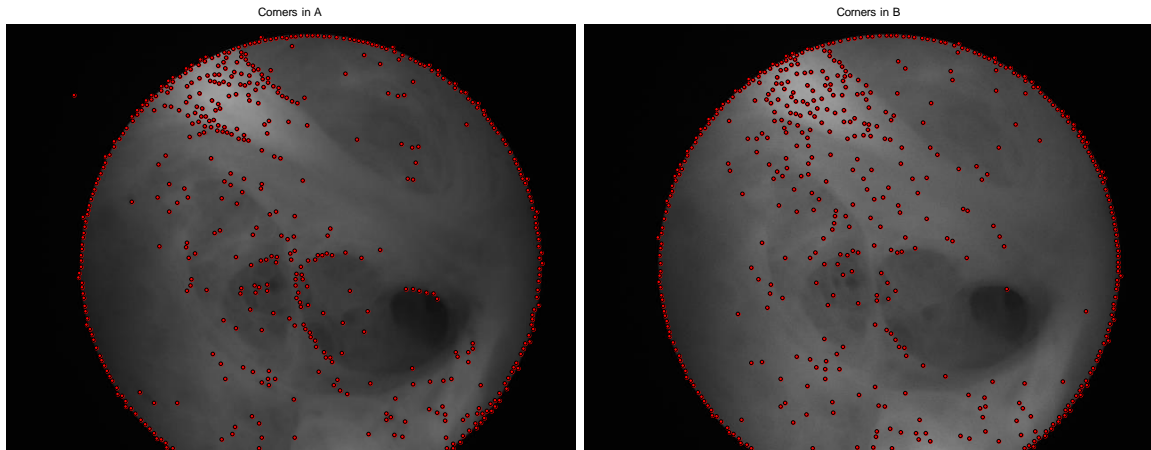


COLOR COMPOSITE (FRAME A = RED, FRAME B = CYAN)

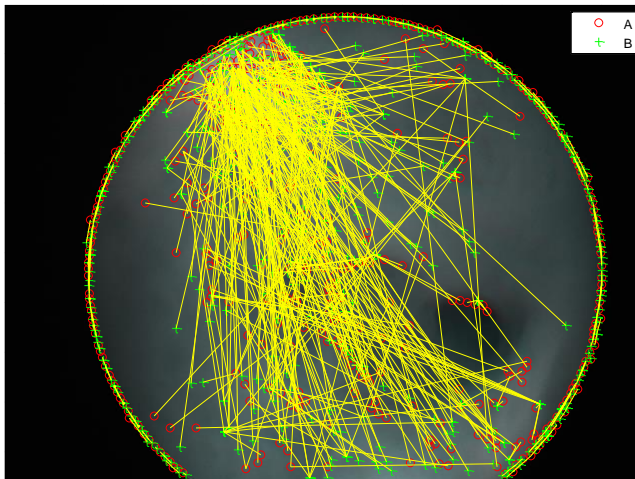


- (2) *Determine an affine transformation that will correct for the distortion between the two frames. As input we must provide a set of point correspondences between the two frames. To generate these correspondences, we first collect points of interest from both frames, then select likely correspondences between them. To have the best chance that these points will have corresponding points in the other frame, we want points around salient image features such as corners (or edges). The FAST⁴ corner detector algorithm is one of the fastest options.*

⁴ (Other) Algorithms used: Harris corner detection (by Harris & Stephens), Minimum eigenvalue (by Shi & Tomasi), or Local intensity comparison (Features from Accelerated Segment Test, FAST by Rosten & Drummond) method.

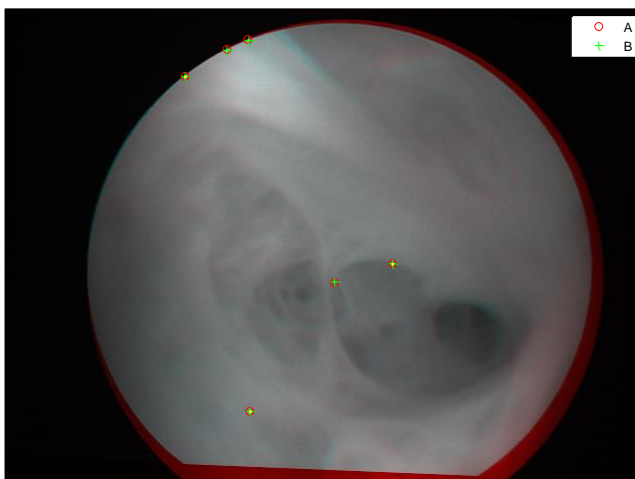


(3) Next we pick correspondences between the points derived above. For each point, we extract a 9-by-9 block centered around it. The matching cost we use between points is the sum of squared differences (SSD) between their respective image regions. Points in frame A and frame B are matched putatively. (Note that there is no uniqueness constraint, so points from frame B can correspond to multiple points in frame A).



THE IMAGE ON THE LEFT SHOWS THE SAME COLOR COMPOSITE GIVEN ABOVE, BUT ADDED ARE THE POINTS FROM FRAME A IN RED, AND THE POINTS FROM FRAME B IN GREEN. YELLOW LINES ARE DRAWN BETWEEN POINTS TO SHOW THE CORRESPONDENCES SELECTED BY THE ABOVE PROCEDURE. MANY OF THESE CORRESPONDENCES ARE CORRECT, BUT THERE IS ALSO A SIGNIFICANT NUMBER OF OUTLIERS.

(4) Many of the point correspondences obtained in the previous step are incorrect. But we can still derive a robust estimate of the geometric transform between the two images using the Random Sample Consensus (RANSAC) algorithm. For added robustness, we run the algorithm multiple times and calculate a cost for each result. This cost is obtained by projecting frame B onto frame A according to the derived transform, and taking the sum of absolute difference (SAD) between the two images. We take the best transform as the one that minimizes this cost.



THE IMAGE ON THE LEFT IS A COLOR COMPOSITE SHOWING FRAME A OVERLAID WITH THE REPROJECTED FRAME B, ALONG WITH THE REPROJECTED POINT CORRESPONDENCES. THE INLIER CORRESPONDENCES ARE NEARLY COINCIDENT. THE CORES OF THE IMAGES ARE BOTH ALIGNED, SUCH THAT THE RED-CYAN COLOR COMPOSITE BECOMES ALMOST PURELY BLACK-AND-WHITE IN THE FOREGROUND REGION.

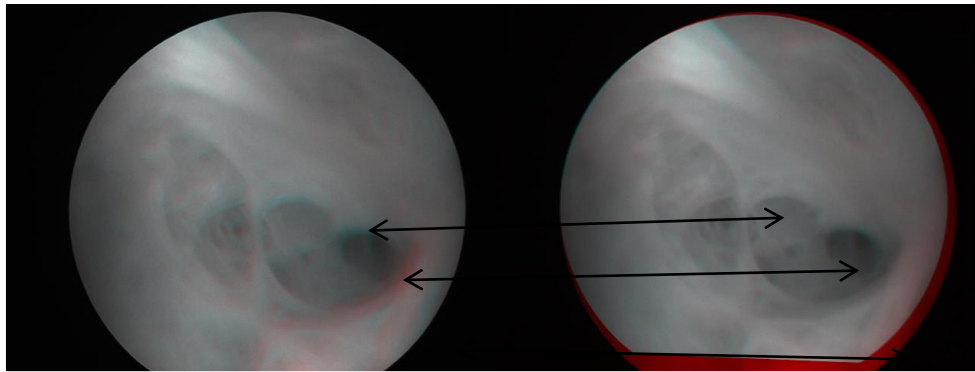


FIGURE 49. LEFT – UNREGISTERED / RIGHT - REGISTERED

- (5) Given a set of video frames, we can now use the above procedure to estimate the distortion between all frames as affine transforms, where the cumulative distortion of a frame relative to the first frame will be the product of all the preceding inter-frame transforms.

Finally, *intensity-based automatic image registration* is an iterative process that requires you specify a pair of images, a metric, an optimizer, and a transformation type. The metric defines the image similarity metric for evaluating the accuracy of the registration. This image similarity metric takes two images and returns a scalar value that describes how similar the images are. The optimizer defines the methodology for minimizing or maximizing the similarity metric. The transformation type defines the type of 2-D transformation that brings the misaligned image into alignment with the reference image. The process begins with the transform type you specify and an internally determined transformation matrix. Together, they determine the specific image transformation that is applied to the image with bilinear interpolation. Next, the metric compares the transformed moving image to the fixed image and a metric value is computed. The method described above is an another type of registration, where instead of extracting features, a metric such as mean square error between images is used for evaluating similarity. Specifically two metrics were implemented, **mean square error** and **Mutual Information Metric** [58] (maximizes the number of coincident pixels with the same relative brightness value) and two optimizers, **gradient descent** (adjusts the transformation parameters so that the optimization follows the gradient of the image similarity metric in the direction of the extrema) and **One-plus-one evolutionary optimizer** (perturbs/mutates a set of parameters that produce the best possible registration result). The results of the following table present typical execution times for all three methods:

CPU I5@2.5GHz	
Method	Registration (sec)
Control point registration	(user specific)
Video stabilization (/4)	3.42
Video stabilization (/8)	2.55
MSE+GD+params1 (/8)	7.56
MSE+GD+params2 (/8)	130.24(~2min)
MI+GD+params1 (/8)	43.80
MI+GD+params2 (/8)	13.31
EO+MI+params1 (/8)	5.17

TABLE 5. PROCESSING TIMES FOR SEVERAL IMAGE REGISTRATION ALGORITHMS.

Overall video stabilization required the minimum execution time but registration with gradient descent optimizer and mutual information metric produced the most visually registered image stack. Furthermore video stabilization was the most sensitive parameter-wise, requiring fine tuning across different stacks.

5. Smoothing

Smoothing reduces additive noise, while producing less pixelated segmentation maps. *Mean, gaussian, median and wiener filtering* have been tested. Comparative maps are presented in the following sections.

All filters produced similar results, but in terms of execution time reduction, the Wiener filter was selected. The goal of the Wiener filter is to filter out noise that has corrupted a signal. It is based on a statistical approach. Typical filters are designed for a desired frequency response. However, the design of the Wiener filter takes a different approach. One is assumed to have knowledge of the spectral properties of the original signal and the noise, and one seeks the linear time-invariant filter whose output would come as close to the original signal as possible. Wiener filters are characterized by the following:

1. Assumption: signal and (additive) noise are stationary linear stochastic processes with known spectral characteristics or known autocorrelation and cross-correlation
2. Requirement: the filter must be physically realizable/causal (this requirement can be dropped, resulting in a non-causal solution)
3. Performance criterion: minimum mean-square error (MMSE)

Wiener filter problem setup

Suppose the input $i(t)$ to a time-varying linear system consists of signal $s(t)$ and additive noise $n(t)$, i.e., $i(t) = s(t) + n(t)$. If the impulse response of the system is $h(t - \tau, t)$, the system output is obtained by the convolution

$$y(t) = \int_{-\infty}^{\infty} h(\tau, t) i(t - \tau) d\tau \quad (\text{A-1})$$

where the integration limits have been defined so as to permit acausal filters. If the desired filter output is $d(t)$, the error signal is

$$e(t) = d(t) - \int_{-\infty}^{\infty} h(\tau, t) i(t - \tau) d\tau \quad (\text{A-2})$$

and the expected error power (mean-squared error) is

$$E[e^2(t)] = E\left\{ \left[d(t) - \int_{-\infty}^{\infty} h(\tau, t) i(t - \tau) d\tau \right]^2 \right\} \quad (\text{A-3})$$

By assuming interchangeability of integration and averaging, and defining

$$\Phi_{di}(t, t-\tau) = E[d(t)i(t-\tau)]$$

$$\Phi_{dd}(t, t-\tau) = E[d(t)d(t-\tau)]$$

and

$$\Phi_{ii}(t, t-\tau) = E[i(t)i(t-\tau)]$$

expression (A-3) becomes

$$E[e^2(t)] = \Phi_{dd}(t, t) - 2 \int_{-\infty}^{\infty} h(\tau, t) \Phi_{di}(t, t - \tau) d\tau + \int_{-\infty}^{\infty} \int_{-\infty}^{\infty} h(\tau, t) h(\tau', t) \Phi_{ii}(t - \tau, t - \tau') d\tau d\tau' \quad (\text{A-4})$$

The optimum filter $h(r, t)$ will minimize $E[e^2(t)]$ in (A-4).

If $h(\tau, t)$ is the response function for the optimum filter, the mean-square error will increase for any perturbation $\delta h(\tau, t)$ from the optimum. For the perturbed system

$$E\{[e(t) + \delta e(t)]^2\} = \Phi_{dd}(t, t) - 2 \int_{-\infty}^{\infty} [h(\tau, t) + \delta h(\tau, t)] \Phi_{di}(t, t - \tau) d\tau + \int_{-\infty}^{\infty} \int_{-\infty}^{\infty} [h(\tau, t) + \delta h(\tau, t)][h(\tau', t) + \delta h(\tau', t)] \Phi_{ii}(t - \tau, t - \tau') d\tau d\tau'$$

$$(\text{A-5})$$

When $E[e^2(t)]$ is a minimum, the difference Δ in mean-square error for equations (A-4) and (A-5) is always positive, being equal to

$$\Delta = 2 \int_{-\infty}^{\infty} [h(\tau, t) \phi_{di}(t, t - \tau) d\tau + 2 \int_{-\infty}^{\infty} \int_{-\infty}^{\infty} h(\tau', t) \delta h(\tau, t) \phi_{ii}(t - \tau, t - \tau') d\tau d\tau' + \int_{-\infty}^{\infty} \int_{-\infty}^{\infty} \delta h(\tau, t) \delta h(\tau', t) \phi_{ii}(t\tau, t - \tau) d\tau d\tau' \quad (A-6)$$

Since the last term in equation (A-6) can be written as a perfect square, it is always positive. Thus Δ will be positive if

$$\int_{-\infty}^{\infty} \delta h(\tau, t) [\phi_{di}(t, t - \tau) - \int_{-\infty}^{\infty} h(\tau', t) \phi_{ii}(t - \tau, t - \tau') d\tau'] d\tau = 0 \quad (A-7)$$

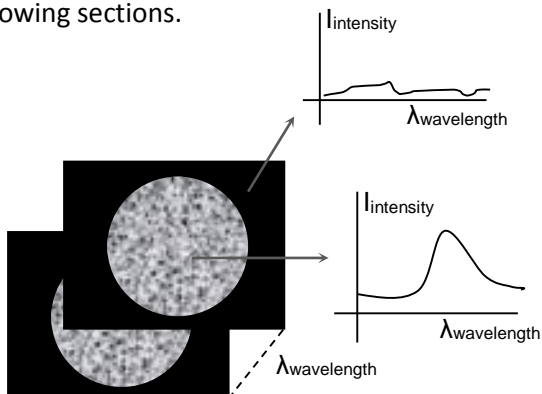
that is, if the optimum filter response satisfies the integral equation

$$\phi_{di}(t, t - \tau) = \int_{-\infty}^{\infty} h(\tau', t) \phi_{ii}(t - \tau, t - \tau') d\tau' = 0 \quad (A-8)$$

Equation (A-8) is the nonstationary form of the Wiener-Hopf equation and involves time-dependent correlation functions and a time-varying linear filter.

6. Remove background

Background information consists mainly of black pixels around images. Removing these pixels with low intensity values enhances greatly execution times during clustering. Comparative results are presented in the following sections.



The image on the left depicts two different pixels from a spectral cube across different wavelengths. Background pixels are nearly zero for every λ :

$$\forall x, y \sum_{\lambda} p(x, y, \lambda) \leq \text{Threshold}$$

(Typical threshold values ~ 0.1-0.4)

7. Clustering

Image segmentation aims to extract regions by dividing an image into disjoint sets of pixel segments or clusters. In the case of (multi/hyper) spectral data, clustering can organize a large quantity of unordered N-dimensional pixels (in this case N=11) into a small number of meaningful and coherent clusters, thereby providing a basis for intuitive and informative understanding of data. Several algorithms have been proposed for clustering spectral data, such as convex cone analysis, multi-thresholding, isoclustering, histogram-based segmentation methods applied to the spectral index image, segmentation of hyperspectral images based on the histogram of the principal components or based on a multicomponent hidden Markov chain mode. Also, statistical hyperspectral image segmentation approach based on Gaussian mixture models and Bayesian segmentation using hidden Markov modeling. Among them, K-means is an established unsupervised method for image segmentation, well-understood with several optimized versions for performance as well as modified versions for specific domains (k-medoids, kernel k-means, spherical k-means. etc.).

In general, given a set \mathbf{S} of pixels \mathbf{p} , k-means clustering aims to partition them into k sets ($S = \{S_1, S_2, \dots, S_k\}$) so as to minimize the within-cluster distance:

$$\underset{S}{\operatorname{argmin}} \sum_{i=1}^k \sum_{p_j \in S_i} D(p_j - \mu_i), \quad \mu_i: \text{mean of pixels in } S_i \text{ (centroid)}$$

The algorithm starts by randomly assigning k clusters in spectral space. Each pixel in the input image stack is assigned to the nearest cluster center and the cluster center locations are moved to the average of their cluster values. This step is repeated until convergence (the assignments no longer change) or when a number of steps (user defined) are completed. An important step for accurate clustering is to determine a similarity/distance metric D . The metric reflects the degree of closeness or separation of the target objects and should correspond to the characteristics that are believed to distinguish the clusters embedded in the data. In many cases, these characteristics are dependent on the data or the problem context at hand, and there is no measure that is universally best for all kinds of clustering problems. Moreover, K-means clustering requires not only a distance metric, but also a way to compute the centroid μ of a cluster. That is, the criterion that is minimized in k-means is the sum of point-to-centroid distances, summed over all clusters. Thus, it is natural to want the centroid to be the point that minimizes the point-to-centroid distances within a cluster. The arithmetic mean does that for (squared) Euclidean distance and there exist only a few distances for which the

centroid is easily computable. More specifically, candidate functions for D must be non-negative, equal to zero for identical pixels and to comply with the triangular (in)equality. Given an initial set of k means $m_1^{(1)}, \dots, m_k^{(1)}$, the algorithm proceeds by alternating between two steps:

Assignment step: Assign each observation to the cluster whose mean yields the least within-cluster sum of squares (WCSS).

$$S_i^{(t)} = \{x_p - m_i^{(t)} \mid \|x_p - m_i^{(t)}\|^2 \leq \|x_p - m_j^{(t)}\|^2 \forall 1 \leq j \leq k\}$$

where each x_p is assigned to exactly one $S_i^{(t)}$, even if it could be assigned to two or more of them.

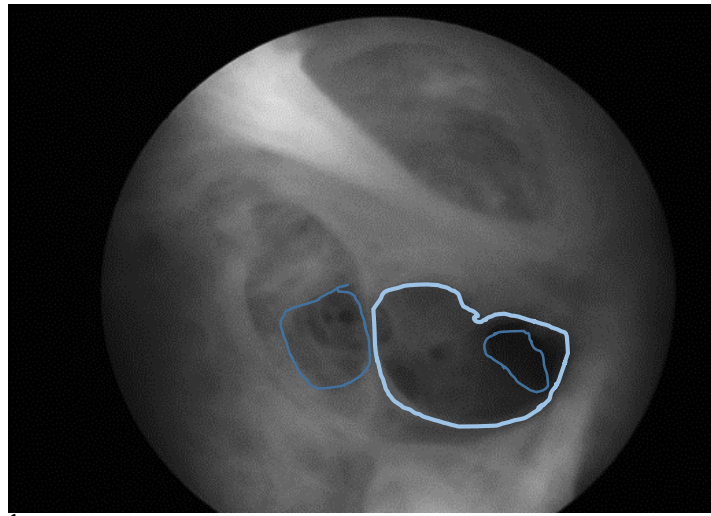
Update step: Calculate the new means to be the centroids of the observations in the new clusters.

$$m_i^{(t+1)} = \frac{1}{|S_i^{(t)}|} \sum_{x_j \in S_i^{(t)}} x_j$$

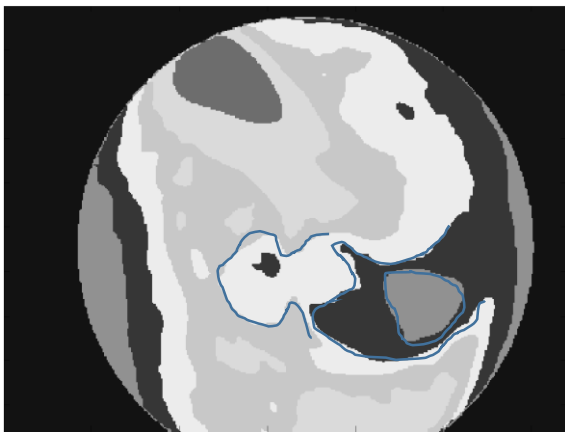
Since the arithmetic mean is a least-squares estimator, this also minimizes the within-cluster sum of squares (WCSS) objective.

Common metrics are *Euclidean, Canberra, Chebychev, Correlation, Jaccard, Manhattan, Cosine*, etc. Cosine metric is a measure of similarity between two vectors (in this case 11-dimensional pixel vectors) by measuring the cosine of the angle between them. The result of the cosine function is equal to 1 when the angle is 0, and it is less than 1 when the angle is of any other value. As the angle between the vectors shortens, the cosine angle approaches 1, meaning that the two vectors are more similar. This is a direct analogy with another established technique for classification of spectral data, spectral angle mapper (SAM); SAM is relatively insensitive to illumination (magnitude) and albedo effects.

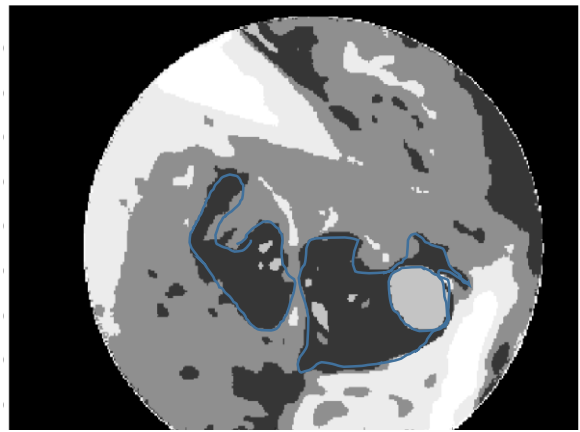
Similarly, the cosine distance measure depends only on the direction of the feature vectors and is independent of their magnitude. Cosine similarity is a convenient technique for producing clusters immune to illumination differences (invariance to multiplicative scaling) between pixel vectors. Moreover, it is not possible to directly substitute cosine with spectral angle, as SAM does not comply with the property of triangle (in)equality.



1

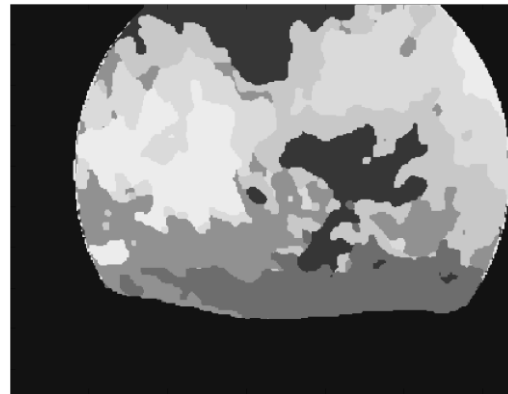
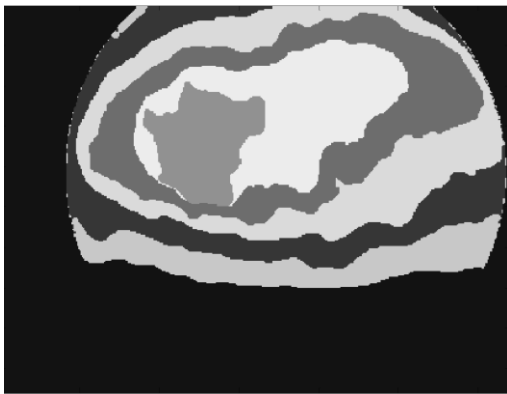
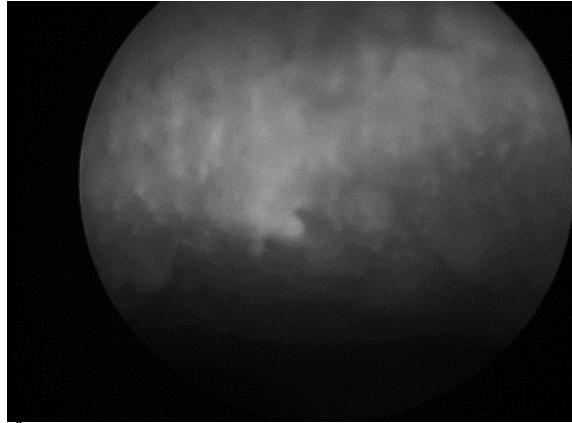


2



3

- (1) GRAYSCALE IMAGE,
- (2) K-MEANS WITH (SQUARE) EUCLIDEAN METRIC,
- (3) K-MEANS WITH COSINE METRIC. IT IS VISUALLY PERCEPTIBLE –ALSO BY THE AID OF HAND-DRAWN ROIS, THAT IN (3), CLUSTER REGIONS ARE MORE SIMILAR WITH THE ORIGINAL GRAYSCALE IMAGE (1).



- (4) GRAYSCALE IMAGE,
- (5) K-MEANS WITH (SQUARE) EUCLIDEAN METRIC,
- (6) K-MEANS WITH COSINE METRIC. IT IS VISUALLY APPARENT, THAT IN (6), CLUSTER REGIONS ARE MORE SIMILAR WITH THE ORIGINAL GRAYSCALE IMAGE (4).

In both examples Euclidean metric produces (near) concentric cluster ellipsoids due to illumination scaling effects of the original grayscale images.

Other parameters worth mentioning are:

a. Batch/update phases

For robustness, we use a k-means version with a two-phase iterative algorithm: The first phase uses batch updates, where in each iteration pixels are reassigned to their nearest cluster centroid, all at once, followed by recalculation of cluster centroids. This phase occasionally does not converge to solution of a local minimum, that is, a partition of the data where moving any single point to a different cluster increases the total sum of distances (more likely to

happen for small data sets). Although, the batch phase is fast, it only approximates a solution used as a starting point for the second phase. The second phase uses online updates, where points are individually reassigned reducing the sum of distances (cluster centroids are recomputed after each reassignment). Each iteration during the second phase consists of one pass through all the points. The second phase will converge to a local minimum, although there may be other local minima with lower total sum of distances.

b. Replicates

The problem of finding the global minimum can only be solved in general by an exhaustive (or clever, or lucky) choice of starting points, but using several replicates with random starting points typically results in a solution that is a global minimum. In order to bypass this inherent problem of K-means we repeat clustering a preconfigured number of times, each with a new set of initial cluster centroid positions. K-means returns the solution with the lowest value of the within-cluster sums of point-to-centroid distances.

c. Initial centroid positions

Three approaches were tested with similar results:

- i. Select k pixels at random,
- ii. Perform a preliminary clustering phase on a random 10% subsample of pixels,
- iii. Perform a preliminary clustering phase using K-Means++ for supplying initial centroid positions [61].

The results of the following table present typical execution times⁵ for several parameter sets:

Clustering Algorithm	Parameter Set				CPU i5@2.5Ghz		CPU i7@2.8Ghz	
	#clusters	replicates	Background Thr.	Subsample	Reduce image Stack+smooth (sec)	Clustering (sec)	Reduce image Stack+smooth (sec)	Clustering (sec)
KM+cos+rand.sam.	5	0	0.6	4	0.295	0.535		
	6	0	0.6	4	0.289	1.032		
	7	0	0.6	4	0.306	0.625		
	8	0	0.6	4	0.294	1.237		
	5	2	0.6	4	0.312	1.364		
	6	2	0.6	4	0.313	2.223		
	7	2	0.6	4	0.293	2.336		
	8	2	0.6	4	0.301	2.390		
	5	4	0.6	4	0.291	2.463		
	6	4	0.6	4	0.288	2.517		
	7	4	0.6	4	0.296	2.797		
	8	4	0.6	4	0.301	3.724		

⁵ Registration time is not included.

	5	0	0.6	8	0.224	0.256	
	6	0	0.6	8	0.245	0.333	
	7	0	0.6	8	0.245	0.277	
	8	0	0.6	8	0.242	0.282	
	5	2	0.6	8	0.268	0.617	
	6	2	0.6	8	0.234	0.374	
	7	2	0.6	8	0.239	0.433	
	8	2	0.6	8	0.242	0.531	
	5	4	0.6	8	0.251	0.476	
	6	4	0.6	8	0.234	0.775	
	7	4	0.6	8	0.256	1.063	
	8	4	0.6	8	0.248	1.056	
	5	2	0	4	0.312	1.679	
	8	2	0	4	0.290	3.194	
	5	2	0	8	0.241	0.510	
	8	2	0	8	0.231	1.151	
KM+cos+cluster	5	2	0.6	4	0.299	0.771	
	8	2	0.6	4	0.292	2.417	
	5	2	0.6	8	0.269	0.310	
	8	2	0.6	8	0.243	0.524	
KM+Euc+rand.sam.	5	2	0.6	4	0.270	5.001	
	8	2	0.6	4	0.286	6.876	
	5	2	0.6	8	0.240	0.663	
	8	2	0.6	8	0.243	1.964	
KM+cos+rand.sam. +norm@700	5	2	0.6	4	0.326	1.201	
	8	2	0.6	4	0.286	3.360	
KM+Euc+rand.sam. +norm@700	5	2	0.6	4	0.297	3.120	
	8	2	0.6	4	0.301	5.122	

↑ clusters	↑ Execution time
↑ replic.	↑ Execution time
↑ subsamp.	↓ Execution time
↑ back.thr.	↑ Execution time
cosine sim	↓ Execution time
Eucl. sim	↑ Execution time

TABLE 6. TYPICAL EXECUTION TIMES FOR SEVERAL PARAMETER SETS.

8. Validation Tests

The process of evaluating the results of cluster analysis in a quantitative and objective way is called cluster validation. It usually has four main components:

- (1) Determine whether there is non-random structure in the data;
- (2) Determine the number of clusters;

(3) Evaluate how well a clustering solution fits the given data when the data is the only information available;

(4) Evaluate how well a clustering solution agrees with partitions obtained based on other data sources.

Among these, Component (3) is known as internal validation while Component (4) is referred to as external validation. Component (1) is fundamental for cluster analysis because almost every clustering algorithm will find clusters in a dataset, even if there is no cluster structure in it. However, this component is not the focus of this report because earlier research and screening tests on the (sub)typing of endometrial neoplasia and cancer with ratio maps of the acquired spectral images confirmed a plurality of different structures with different symptoms.

We can use internal and/or external validation to determine the number of clusters in a dataset. In the context of this study, we do not have a ground-truth partition of the data to which we can compare our solution. Therefore, the number of clusters in our data is determined using internal validation only. Specifically, two main measures are used to evaluate clustering solutions internally: fitness and stability, both of which are employed in this study. Evaluating the fitness of a clustering solution refers to the quality of a clustering solution, usually evaluated by indices that are based on geometrical properties of clusters such as compactness, separation, and connectedness, as these criteria are the ones being optimized by most clustering methods [63-64]:

- a. *Silhouette index,*
- b. *Davies-Bouldin,*
- c. *Calinski-Harabasz,*
- d. *Dunn index,*
- e. *R-squared index,*
- f. *Hubert-Levin (C-index),*
- g. *Krzanowski-Lai index,*
- h. *Hartigan index,*

Furthermore, the stability of a clustering solution, which usually refers to how robust a clustering solution is under perturbation or sub-sampling of the original data [65-66], is another commonly-used validation criterion. A stable clustering solution is considered to have captured the underlying structure of a dataset, under the assumption that this clustering solution should be reproducible on other datasets drawn from the same source. One of the methods we use to estimate the number of

clusters for our dataset is to assess the stability of clustering results by replication analysis [64]. To perform replication analysis, a dataset is split into two equal subsets. As the core part of the analysis, the partition performed on one subset is used as the “ground truth” to group the items in the other subset via classification:

1. *Two disjoint subsets, A and B, are selected at random from a dataset D; Subset A is grouped into k disjoint clusters and subset B is also grouped into k disjoint clusters.*
2. *A classification model is built to learn the class structure of subset A, assuming A is the training set and Clustered(A) is the ground truth; The data points in subset B are classified using the this classification model.*
3. *The degree of replication between A and B is measured by the agreement between the two partitions of subset B, Classified(B) and Clustered(B).*

In Step (2) of the procedure of replication analysis, a strong classification algorithm which has a small empirical classification error is needed, so that the agreement between *Classified(B)* and *Clustered(B)* can be attributed to the intrinsic stability of the clustering solution, without considering the influence a poor classifier may have on the agreement. However, there is no known and agreed-upon optimal classification algorithm [64]. An intuitive choice would be a classifier that mimicked the clustering algorithm used to analyze subsets A and B. When no such choice is available, a k-nearest neighbor classifier is proposed¹⁷. In our experiments we used a modified version of Nearest Neighbor classifier with cosine distance metric. Four measurements of agreement were used:

- a. *Rand index,*
- b. *Adjusted Rand index,*
- c. *Jaccard index,*
- d. *Fowlkes-Mallows (FM) index.*

Internal indices

The following sections provide the precise definitions of the most important internal quality indices used in this study, which have been proposed by various authors in order to determine an optimal clustering. These indices, also called quality indices, are all denoted by the same letter C. Let us also denote by d the distance function between two points.

Silhouette method

Assume the data have been clustered via any technique, such as k-means, into k clusters. For each datum i , let

- $a(i)$ be the average dissimilarity of i with all other data within the same cluster. Any measure of dissimilarity can be used but distance measures are the most common. We can interpret
- $a(i)$ as how well i is assigned to its cluster (the smaller the value, the better the assignment). We then define the average dissimilarity of point i to a cluster c as the the average of the distance from i to points in c .
- $b(i)$ be the lowest average dissimilarity of i to any other cluster which i is not a member. The cluster with this lowest average dissimilarity is said to be the "neighbouring cluster" of i because it is the next best fit cluster for point i .

We now define:

$$s(i) = \begin{cases} 1 - \frac{a(i)}{b(i)}, & \text{if } a(i) < b(i) \\ 0, & \text{if } a(i) = 0 \\ \frac{b(i)}{a(i)} - 1, & \text{if } a(i) > b(i) \end{cases}$$

From the above definition it is clear that

$$-1 \leq s(i) \leq 1$$

For $s(i)$ to be close to 1 we require $a(i) \ll b(i)$. As $a(i)$ is a measure of how dissimilar i is to its own cluster, a small value means it is well matched. Furthermore, a large $b(i)$ implies that i is badly matched to its neighbouring cluster. Thus an $s(i)$ close to one means that the datum is appropriately clustered. If $s(i)$ is close to negative one, then by the same logic we see that i would be more appropriate if it was clustered in its neighbouring cluster. An $s(i)$ near zero means that the datum is on the border of two natural clusters.

The average $s(i)$ over all data of a cluster is a measure of how tightly grouped all the data in the cluster are. Thus the average $s(i)$ over all data of the entire dataset is a measure of how appropriately the data has been clustered. If there are too many or too few clusters, as may occur when a poor choice of k is used in the k-means algorithm, some of the clusters will typically display much narrower silhouettes than the rest. Thus silhouette plots and averages may be used to determine the natural number of clusters within a dataset.

Davies–Bouldin method

Let $R_{i,j}$ be a measure of how good the clustering scheme is. This measure, by definition has to account for $M_{i,j}$ the separation between the i^{th} and the j^{th} cluster, which ideally has to be as large as possible, and S_i , the within cluster scatter for cluster i , which has to be as low as possible. Hence the Davies Bouldin Index is defined as the ratio of S_i and $M_{i,j}$ such that these properties are conserved:

1. $R_{i,j} \geq 0$
2. $R_{i,j} = R_{j,i}$
3. *If $S_j \geq S_k$ and $M_{i,j} = M_{i,k}$ then $R_{i,j} > R_{i,k}$*
4. *and if $S_j = S_k$ and $M_{i,j} \leq M_{i,k}$, then $R_{i,j} > R_{i,k}$*

$$R_{i,j} = \frac{S_i + S_j}{M_{i,j}}$$

This is the symmetry condition. Due to such a formulation, the lower the value, the better the separation of the clusters and the 'tightness' inside the clusters. If N is the number of clusters:

$$DB \equiv \frac{1}{N} \sum_{i=1}^N D_i$$

DB is called the Davies Bouldin Index. This is dependent both on the data as well as the algorithm. D_i chooses the worst case scenario, and this value is equal to $R_{i,j}$ for the most similar cluster to cluster i . There could be many variations to this formulation, like choosing the average of the cluster similarity, weighted average and so on.

These conditions constrain the index so defined to be symmetric and non-negative. Due to the way it is defined, as a function of the ratio of the within cluster scatter, to the between cluster separation, a lower value will mean that the clustering is better. It happens to be the average similarity between each cluster and its most similar one, averaged over all the clusters, where the similarity is defined as S_i above. This affirms the idea that no cluster has to be similar to another, and hence the best clustering scheme essentially minimizes the Davies Bouldin Index. This index thus defined is an average over all the i clusters, and hence a good measure of deciding how many clusters actually exists in the data is to plot it against the number of clusters it is calculated over. The number i for which this value is the lowest is a good measure of the number of clusters the data could be ideally classified into. This has applications in deciding the value of k in the kmeans algorithm, where the value of k is not known apriori.

Dunn method

Let C_i be a cluster of vectors. Let x and y be any two n dimensional feature vectors assigned to the same cluster C_i .

$\Delta_i = \max_{x,y \in C_i} d(x,y)$, which calculates the maximum distance

$\Delta_i = \frac{1}{|C_i|(|C_i| - 1)} \sum_{x,y \in C_i, x \neq y} d(x,y)$, which calculates the mean distance between all pairs

$\Delta_i = \frac{\sum_{x \in C_i} d(x, \mu)}{|C_i|}$, $\mu = \frac{\sum_{x \in C_i} x}{|C_i|}$, calculates the distance of all the points from the mean

This can also be said about the intercluster distance, where similar formulations can be made, using either the closest two data points, one in each cluster, or the farthest two, or the distance between the centroids and so on. The definition of the index includes any such formulation, and the family of indices so formed are called Dunn-like Indices. Let $\delta(C_i, C_j)$ be this intercluster distance metric, between clusters C_i and C_j .

With the above notation, if there are m clusters, then the Dunn Index for the set is defined as:

$$DI_m = \min_{1 \leq i \leq m} \left\{ \min_{1 \leq j \leq m, j \neq i} \left\{ \frac{\delta(C_i, C_j)}{\max_{1 \leq k \leq m} \Delta_k} \right\} \right\}$$

Being defined in this way, the DI depends on m , the number of clusters in the set. If the number of clusters is not known apriori, the m for which the DI is the highest can be chosen as the number of clusters. There is also some flexibility when it comes to the definition of $d(x,y)$ where any of the well known metrics can be used, like Manhattan distance or Euclidean distance based on the geometry of the clustering problem. This formulation has a peculiar problem, in that if one of the clusters is badly behaved, where the others are tightly packed, since the denominator contains a 'max' term instead of an average term, the Dunn Index for that set of clusters will be uncharacteristically low. This is thus some sort of a worst case indicator, and has to be used keeping that in mind.

Calinski-Harabasz method

The cluster index of Calinski and Harabasz is calculated using the following equation:

$$CH(K) = \frac{[\text{trace} \frac{B}{K} - 1]}{[\text{trace} \frac{W}{N} - K]} \text{ for } K \in N,$$

where **B** denotes the error sum of squares between different clusters (inter-cluster)

$$\text{trace } B = \sum_{k=1}^K |C_k| |\bar{C}_k - \bar{x}|^2$$

and **W** the squared differences of all objects in a cluster from their respective cluster center (intra-cluster)

$$\text{trace } W = \sum_{k=1}^K \sum_{i=1}^N w_{k,i} \|x_i - \bar{C}_k\|^2$$

Calculated for each possible cluster solution the maximal achieved index value indicates the best clustering of the data. The important characteristic of the index is the fact that on the one hand trace **W** will start at a comparably large value. With increasing number of clusters K , approaching the optimal clustering solution in K^* groups, the value should significantly decrease due to an increasing compactness of each cluster. As soon as the optimal solution is exceeded an increase in compactness and thereby a decrease in value might still occur; this decrease, however, should be notably smaller. On the other hand, trace **T** should behave in the opposite direction, getting higher as the number of clusters K increases, but should also reveal a kind of softening in its rise if K gets larger than K^* .

Hubert-Levin (C-index) method

Let us consider the distances between the pairs of points inside each cluster. One computes the following three quantities:

- S_w is the sum of the N_w distances between all the pairs of points inside each cluster;

- S_{min} is the sum of the N_w smallest distances between all the pairs of points in the entire data set. There are N_T such pairs: one takes the sum of the N_w smallest values ;
- S_{max} is the sum of the N_w largest distances between all the pairs of points in the entire data set. There are N_T such pairs: one takes the sum of the N_w largest values.

The C-index is defined like this:

$$C = \frac{S_w - S_{min}}{S_{max} - S_{min}}$$

If one considers the N_T distances between pairs of points as a sequence of values sorted in increasing order, the C index uses the N_w smallest values and the N_w largest values in order to compute the sums S_{min} and S_{max} : the sum S involves the N_w distances in this sequence which correspond to pairs present in some cluster (that is to say pairs whose two points are in a same cluster). No more than $3N_w$ distances are effectively retained in the calculation of this index.

Krzanowski-Lai index

Krzanowski and Lai developed a cluster index that, similar to the index of Calinski and Harabasz, is based on the squared differences of all objects in a cluster from their respective cluster center – trace W . The authors define $DIFF(K)$ as the difference between a clustering of the data in K and a clustering in $K-1$ clusters. Let J be the number of variables that have been measured on each $x_i \in X$ and trace W_k the sum of squares function that corresponds to the clustering in K clusters, their measure $DIFF(K)$ is then defined as follows:

$$DIFF(K) = (K - 1)^{\frac{2}{J}} \text{trace } W_{K-1} - K^{\frac{2}{J}} \text{trace } W_K$$

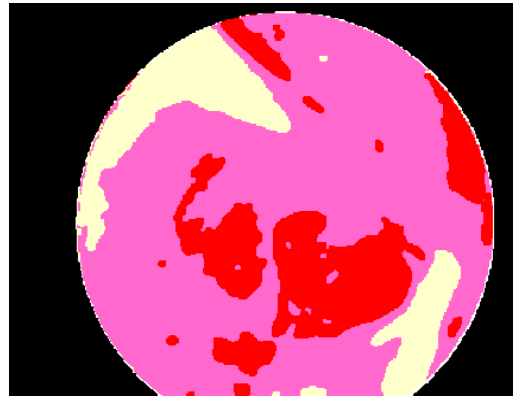
Here, the introduction of the normalizing factor $2/J$ is derived from the observation that – given independently uniformly distributed measurements on each variable $j \in [1, \dots, J]$ – the optimal clustering of the data will reduce the sum of squares exactly by this factor. The authors claim that if there exists an optimal clustering solution in K^* groups, the value of $DIFF(K^*)$ should be comparably large and positive. In contrast, all values of $DIFF(K^*)$ for $K > K^*$ will have rather small values (maybe even negative), while values for $K < K^*$ will be rather large and positive. Bringing these observations together, the $KL(K)$ is defined as follows:

$$KL(K) = \left| \frac{DIFF(K)}{DIFF(k+1)} \right|$$

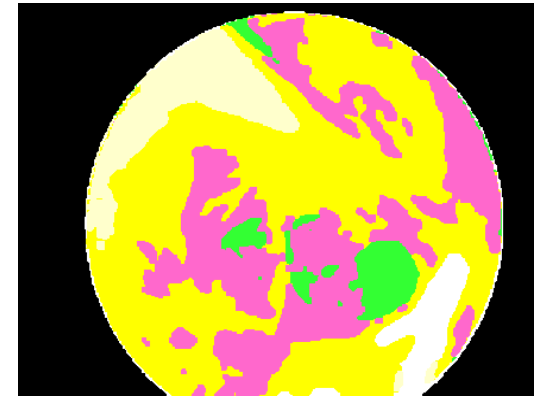
The optimal cluster solution is then indicated by the highest value of KL(K).

9. Pseudocolor Correction

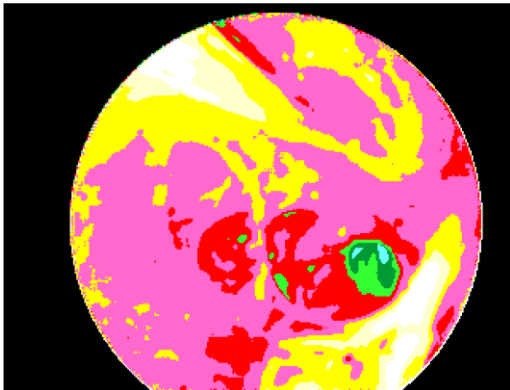
K-means algorithm returns an integer for each pixel indicating cluster membership, while a pseudocolor map can be induced by representing pixels with k different colors (numbers). However, as membership is represented by a set of numbers randomly generated by k-means, a map is required to depict not only different clusters but cluster colors should also be consistent with different symptoms/pathologies. Previous clinical trials utilized a 12 color scale based on a ratio index between the 575 nm and the 675 nm images. A correction scheme is implemented by comparing clustering centroids against ratio centroids with Spectral Angle Mapper (other spectral metrics could also be used). If a cluster centroid spectrum is similar with a ratio centroid, calculated as the mean spectrum of all spectra in the image with the same ratio index value, then the corresponding cluster(s) on the thematic map is (re)colored based on the 12 color scale. Finally a morphological closing operator (dilation and erosion) is performed on the pseudocolor map for merging small partitions. Also, if the image stack is subsampled, then the pseudocolor map is resized to original spatial dimensions (1280x1024) by nearest-neighbor interpolation.



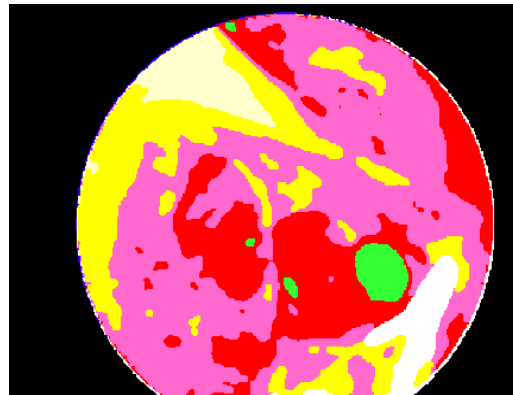
k=4



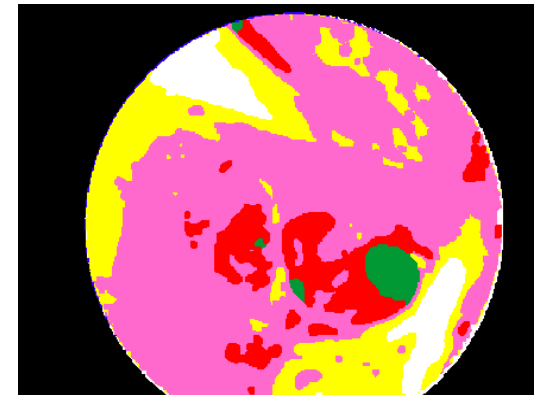
k=6



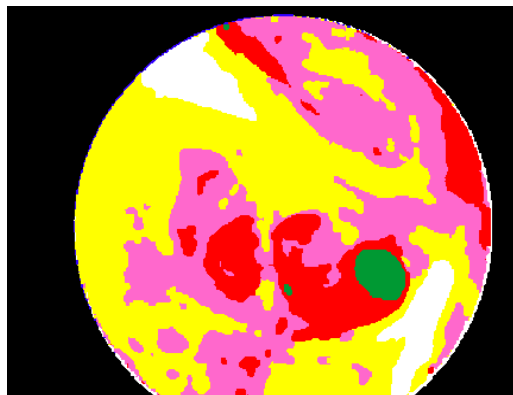
RATIO INDEX



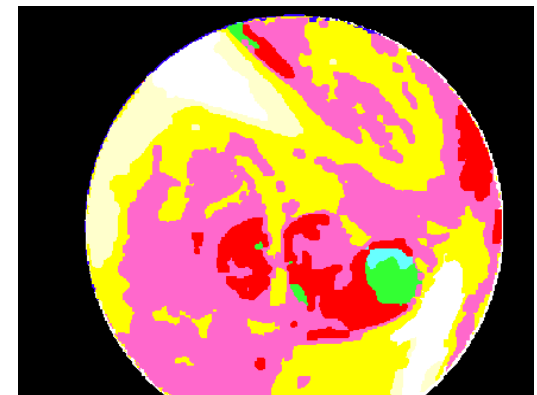
k=8



k=10

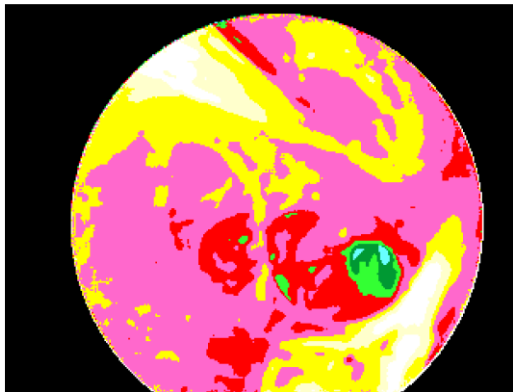


k=12



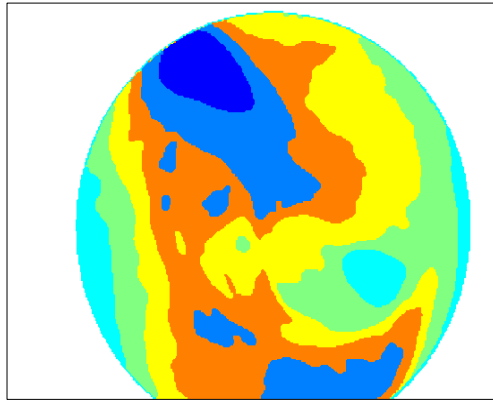
k=14

*RATIO INDEX VERSUS K-MEANS FOR
k=4,6,8,10,12,14. MAPS HAVE BEEN CORECTED WITH
RATIO INDEX COLOR SCALE CAUSING ONE OR MORE
OF THE ORIGINAL K CLUSTERS TO MERGE. MERGING
OCCURS WHEN TWO OR MORE K-MEANS CENTROIDS
ARE SIMILAR WITH THE SAME RATIO INDEX CENTROID.
SIMILARITY IS DEFINED BY MEASURING THE ANGLE
BETWEEN SPECTRA (SAM).*

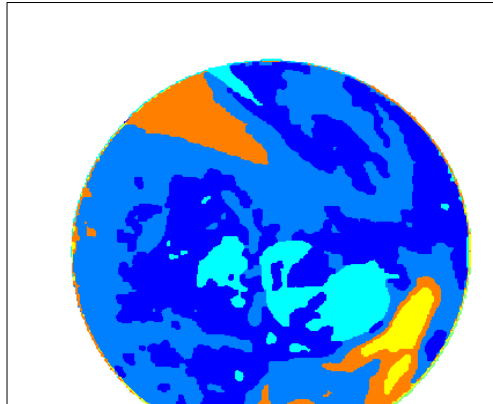


RATIO INDEX

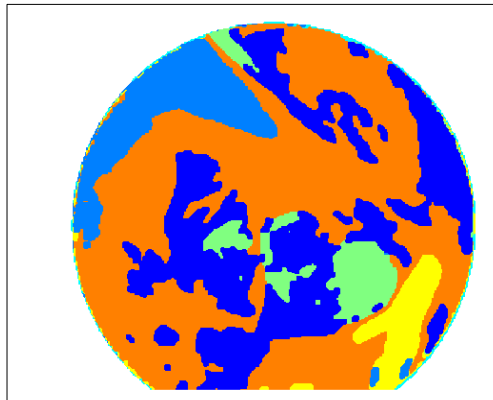
RATIO INDEX VERSUS K-MEANS FOR DIFFERENT DISTANCE METRICS. EUCLIDEAN METRIC PRODUCES (NEAR) CONCENTRIC CLUSTER ELLIPSOIDS DUE TO ILLUMINATION SCALING EFFECTS OF THE ORIGINAL GRAYSCALE IMAGES. MAPS HAVE ALSO BEEN CORRECTED WITH RATIO INDEX COLOR SCALE.



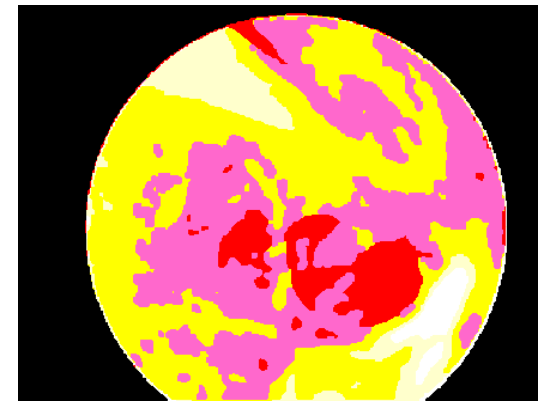
EUCLIDEAN DISTANCE METRIC (k=6)

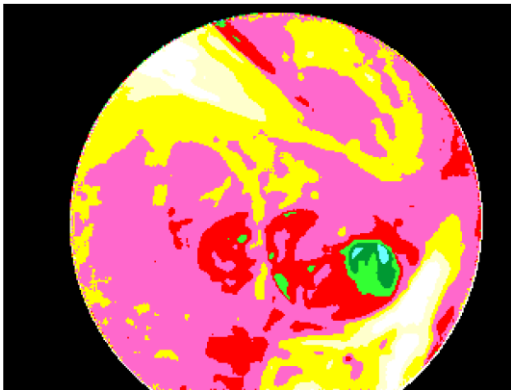


NORMALIZED EUCLIDEAN DISTANCE METRIC (k=6) (@700)



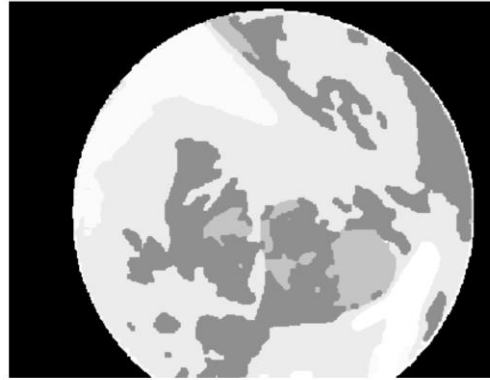
COSINE DISTANCE METRIC (k=6)



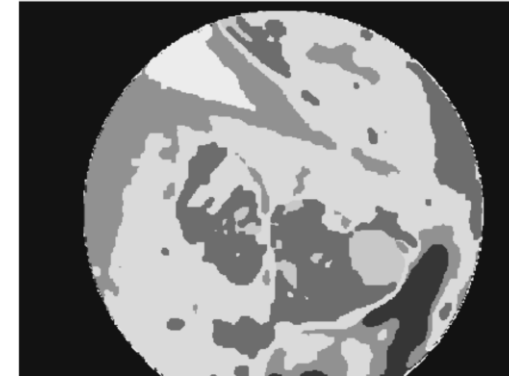


RATIO INDEX

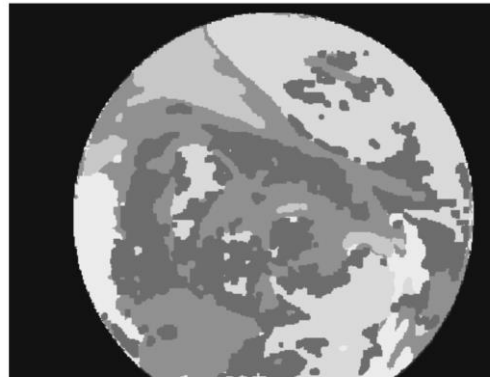
RATIO INDEX VERSUS K-MEANS FOR DIFFERENT FEATURES ($k=6$, COSINE). 575NM AND 675 NM IMAGES WERE USED FOR RATIO INDEX. K-MEANS WITH ONLY 575 AND 675NM IMAGES YIELDS A VERY SIMILAR MAP WITH RATIO MAP (WITH YELLOW ARE UNDERLINED THE FEATURES USED FOR EACH K-MEAN RUN).



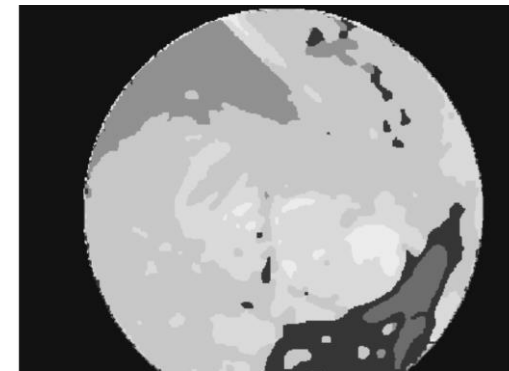
@440, 470, 500, 525, 550, 575, 600, 625, 650, 675, 700



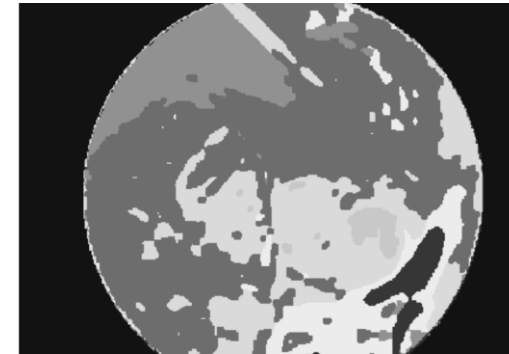
@440, 470, 500, 525, 550, 575, 600, 625, 650, 675, 700



@440, 470, 500, 525, 550, 575, 600, 625, 650, 675, 700

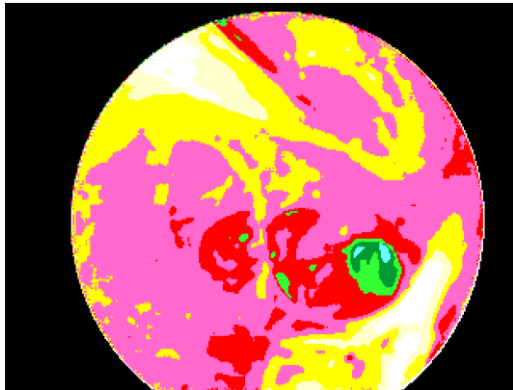


@440, 470, 500, 525, 550, 575, 600, 625, 650, 675, 700





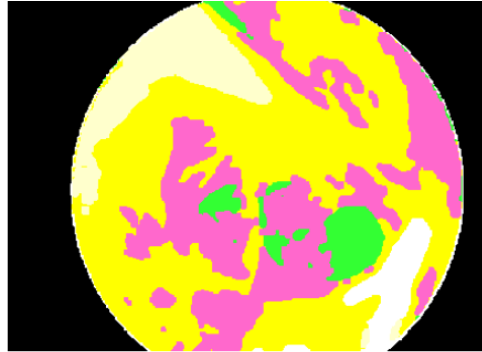
RATIO INDEX PROCESSED



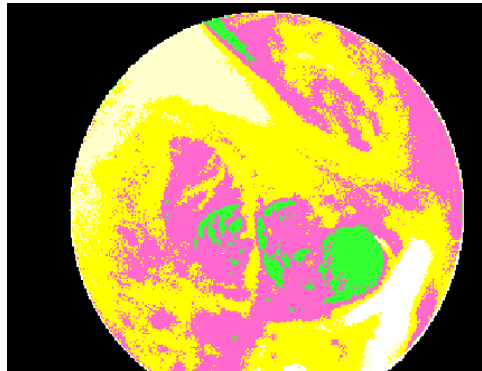
RATIO INDEX RAW



@440, 470, 500, 525, 550, 575, 600, 625, 650, 675, 700



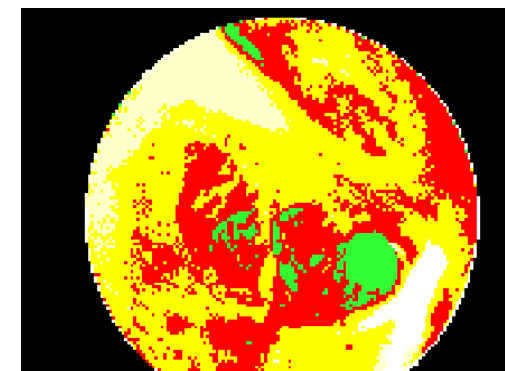
SUBSAMPLE /4



@440, 470, 500, 525, 550, 575, 600, 625, 650, 675, 700



SUBSAMPLE /8

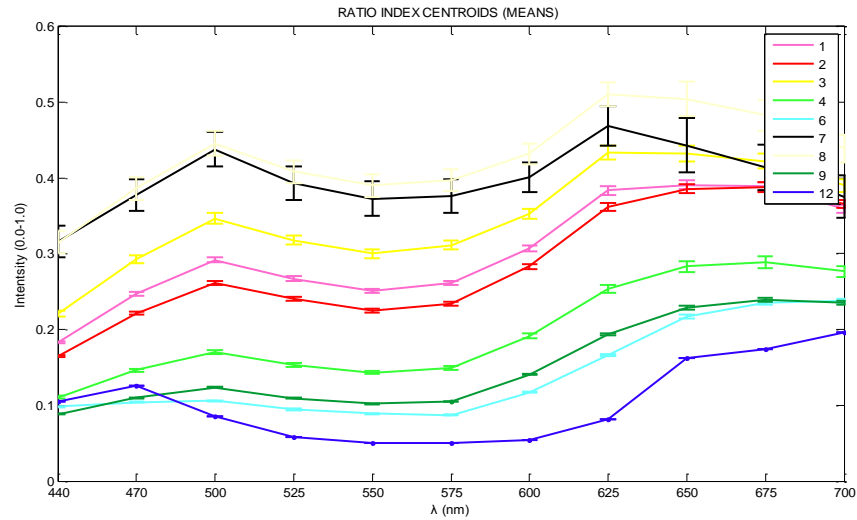


SUBSAMPLE /4, NO (PRE)SMOOTHING BY WIENER FILTERING,
NO (POST) CLOSING, NO BACKGROUND REMOVAL

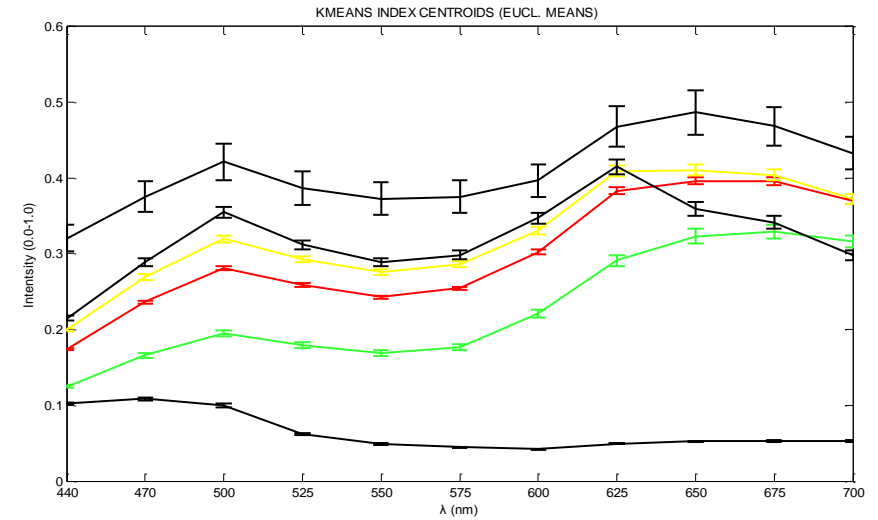


SUBSAMPLE /8, NO (PRE)SMOOTHING BY WIENER FILTERING,
NO (POST) CLOSING, NO BACKGROUND REMOVAL

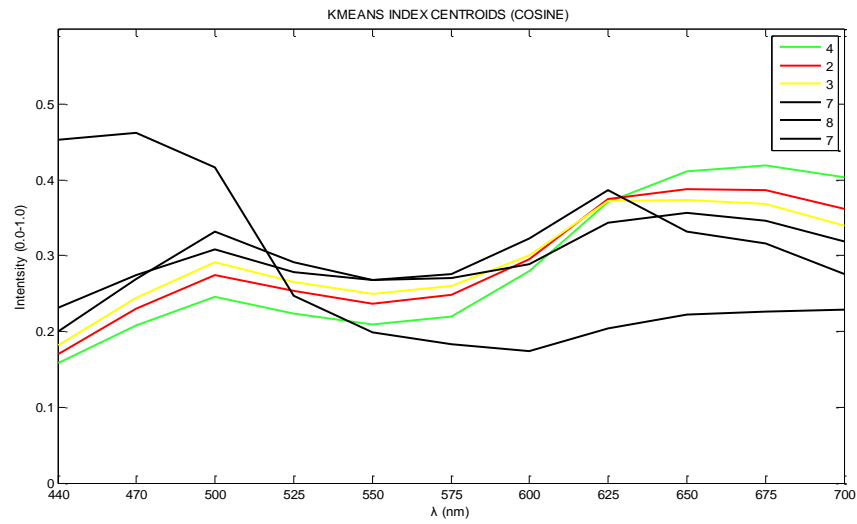
DIFFERENT MAPS WITH/WITHOUT PRE/POST
PROCESSING (K-MEANS MAP EVALUATION WITHOUT



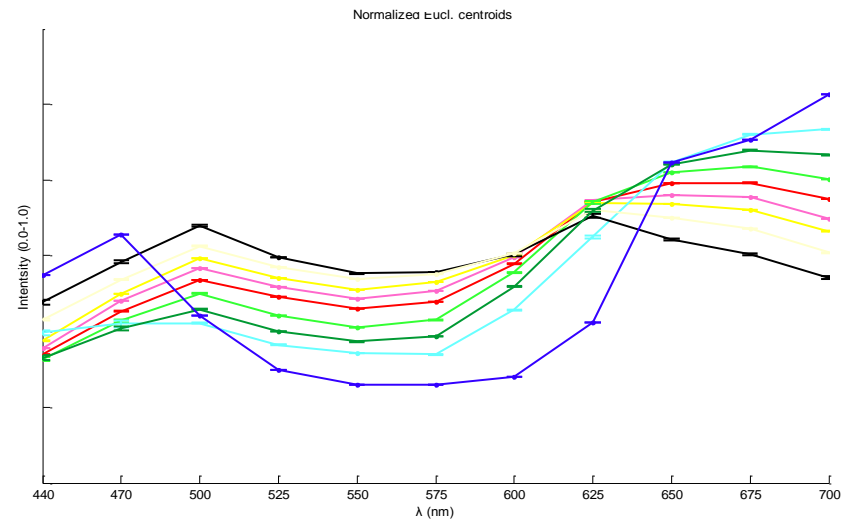
(A)



(B)



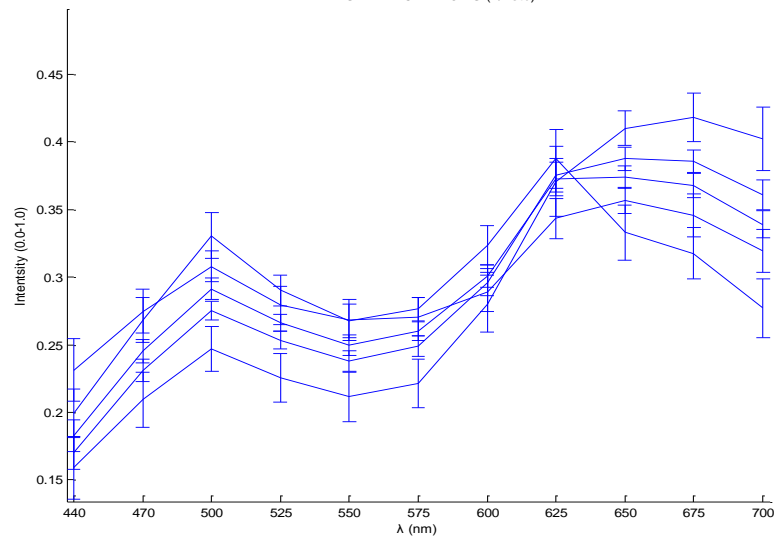
(C)



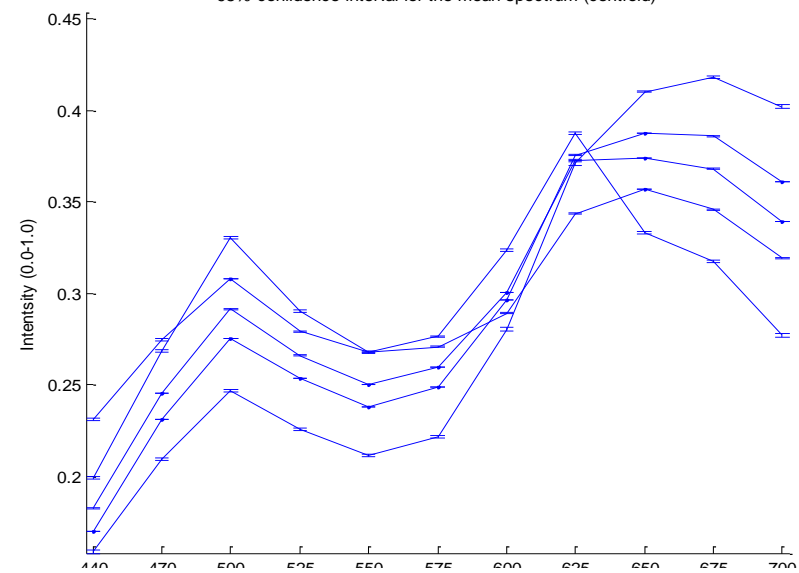
(D)

(A) MEAN SPECTRA FROM RATIO INDEX, (B) MEAN SPECTRA FROM K-MEANS CLUSTERS, (C) K-MEANS COSINE CENTROIDS, (D) NORMALIZED MEAN SPECTRA FROM RATIO INDEX. LEGENDS/COLORS INDICATE ANGLE SIMILARITY BETWEEN K-MEANS AND RATIO SPECTRA.

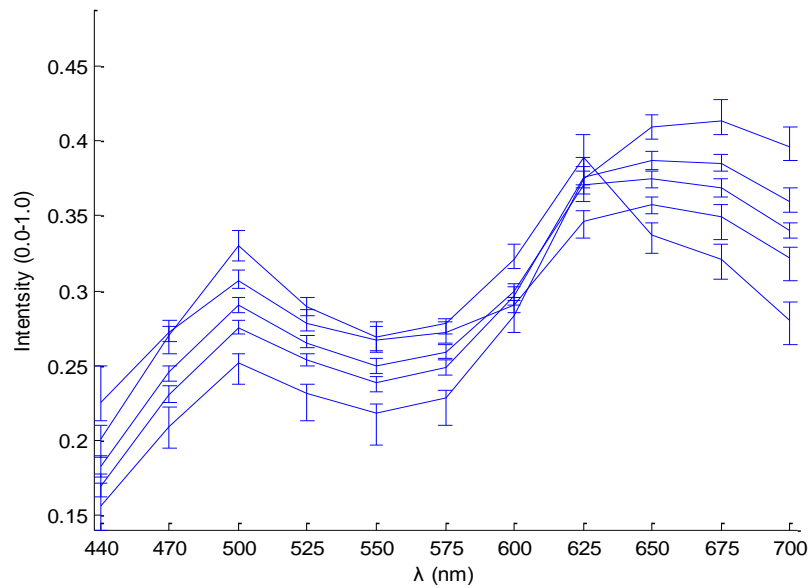
KMEANS INDEX CENTROIDS (+/- std)



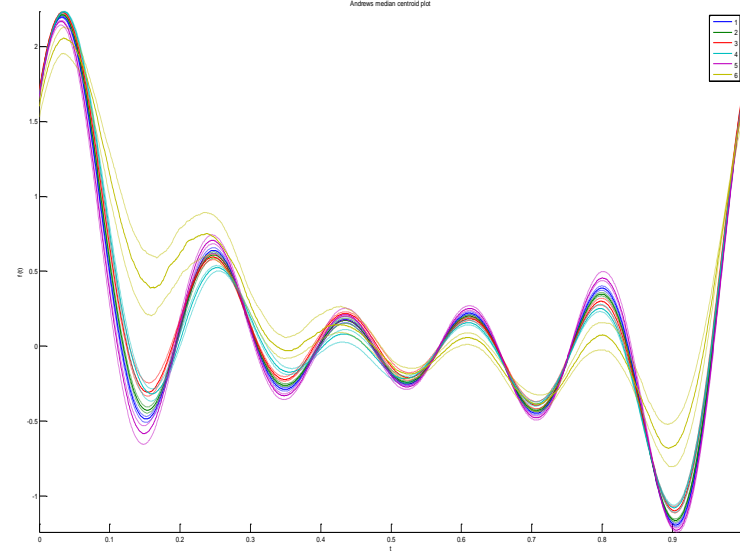
95% confidence interval for the mean spectrum (centroid)

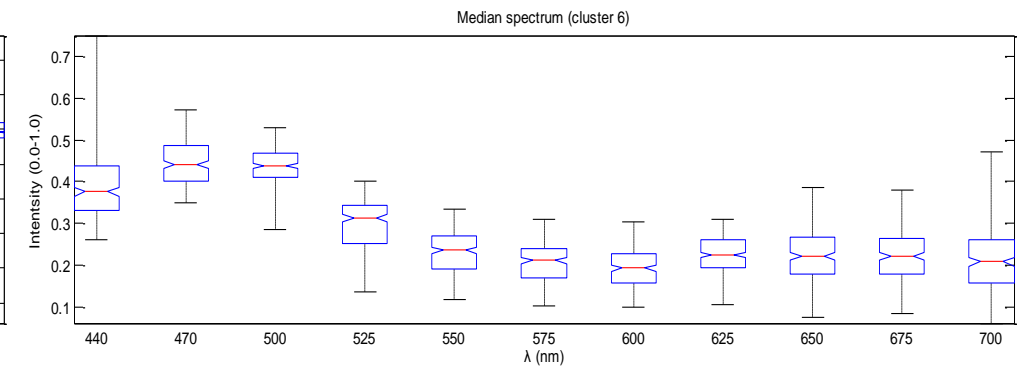
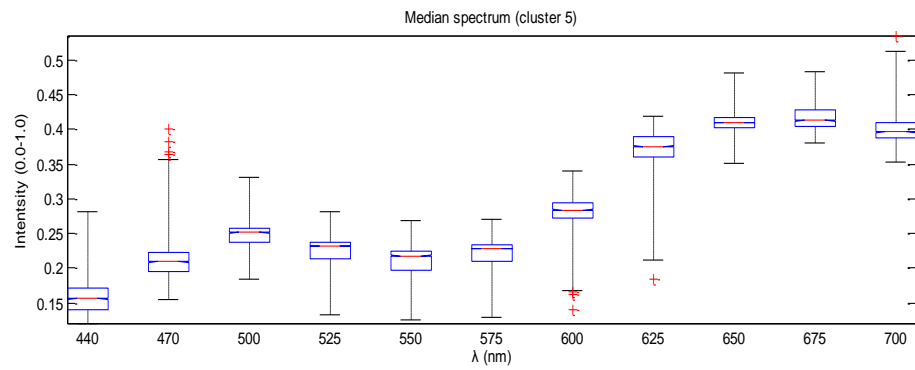
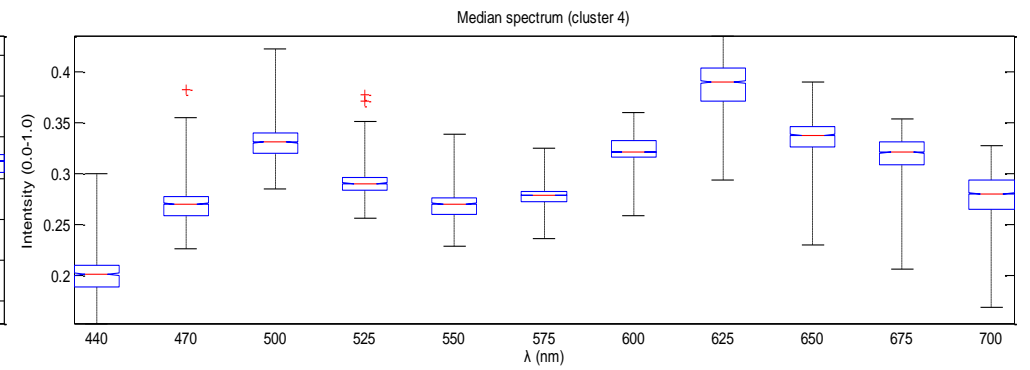
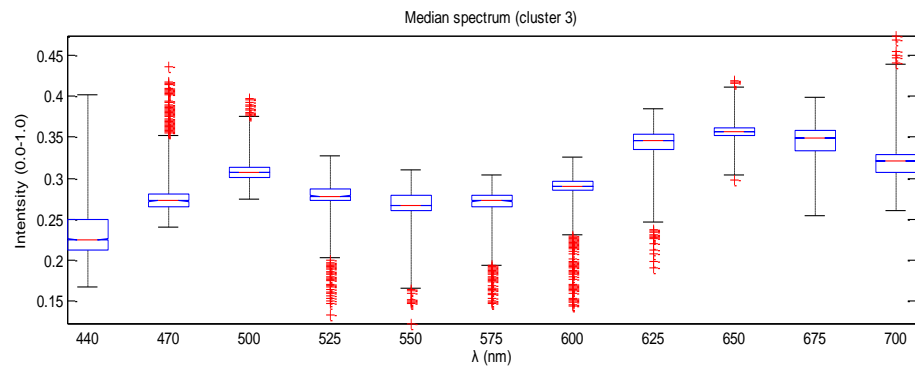
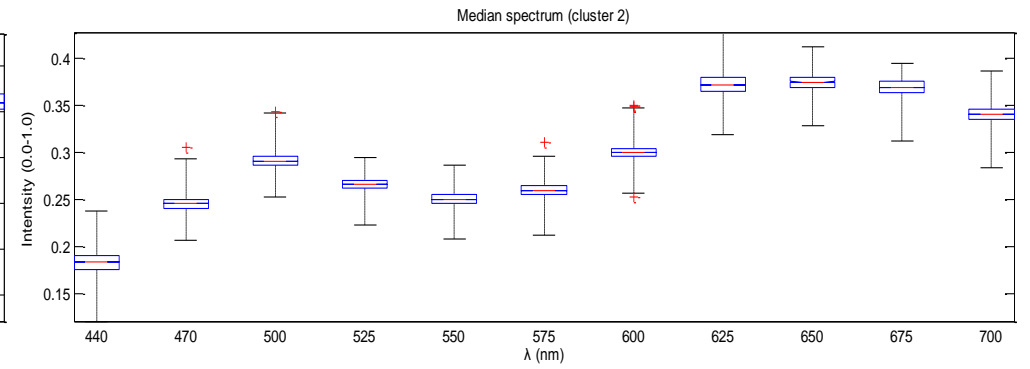
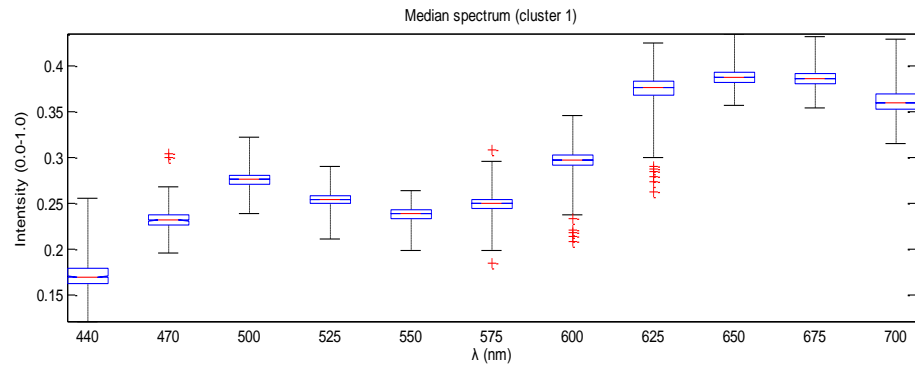


Median cluster spectrum



Andrews median centroid plot

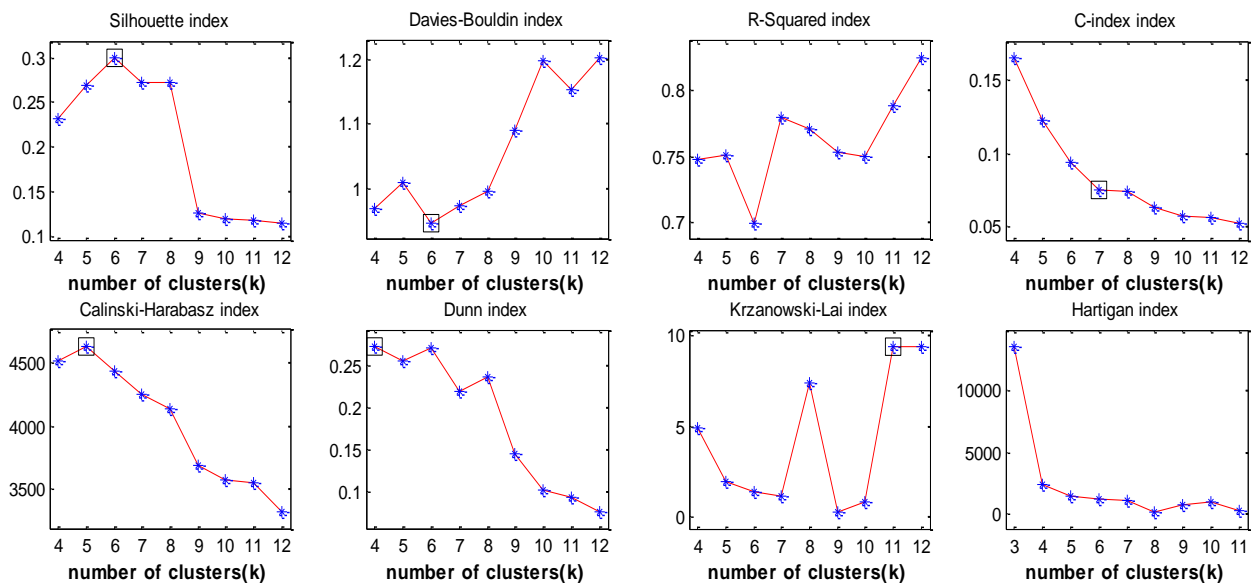
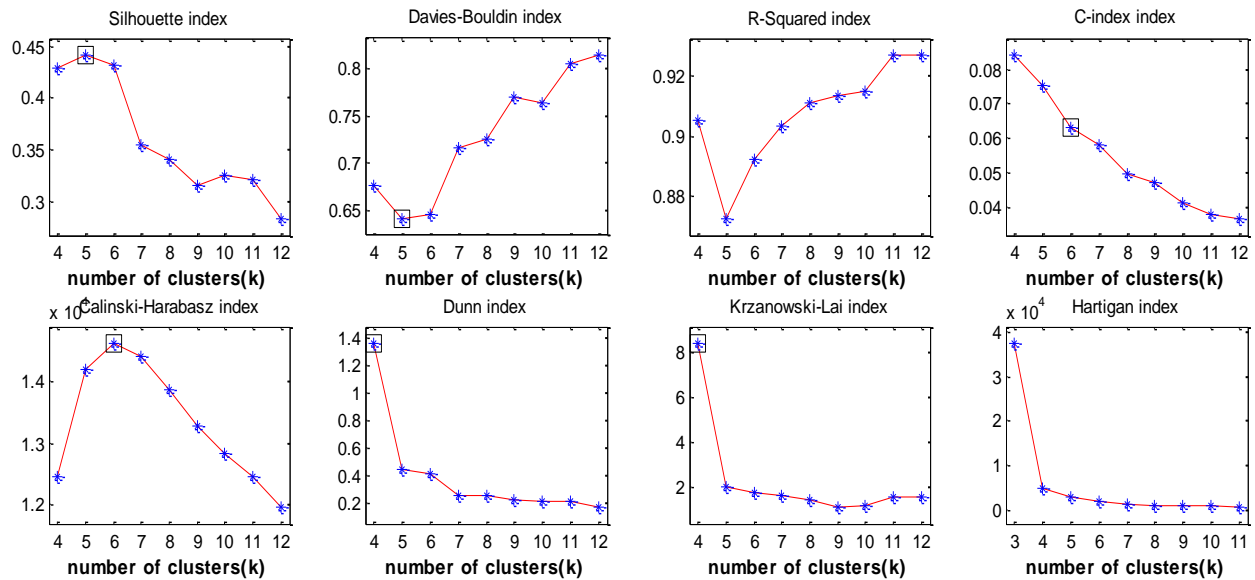




Cluster Validation

(a) fitness:

[image stack is reduced by subsampling /8 as it was not possible to evaluate indexes at higher sampling rates due to hardware restrictions]



All of the above indexes were implemented using Euclidean distance metric; the first eight plots depict different indexes for a normalized set of features @700nm (prior to normalization image @700 is processed by a gaussian filter eliminating any distinct features), while the next eight plots validate cluster number with standard normalization (every feature normalized to 0-1 range, dividing by the largest element of every feature). Different normalization strategies affect both k-means clustering outcome and validation indexes. Some indexes didn't produce meaningful results (R-square, Hartigan), others are prone to noise and outliers (Krzanowski-Lai), while others always predict the minimum k (Dunn index). This result is also reproduced with other k ranges (k= 3 – 8, k= 3 – 12, k= 2 – 12) due to overlapping clusters.

Finally based on these preliminary results, the mean outcome of Silhouette, Davies-Bouldin, Calinski-Harabasz and C-index is 5,75 ≈ 6 clusters

Results and discussion

The light throughput of the SPECL's-VOF light source was measured with the photometer (Thorlabs PM100D) and found to increase from 30-60% in the range 400-460 nm and then remained flat for all other wavelengths within the visible and the infrared wavelength range. The FWHM of the SPECL's-VOF light source was measured with the spectrometer (Ocean Optics USB4000) and found to range from about 11nm to about 14 nm, indicating a quite sufficient spectral resolution across the operating wavelength range. The combined high and flat light throughput and spectral resolution was the key factor that enabled the SPECL endoscope to perform fast (within 2 s) and of high spatial resolution, imaging. This was obtained even in the case of a 3.5 mm thin, low throughput hysteroscope. Figure 36 illustrates a series of representative spectral images belonging to a spectral cube. In the bottom-right part of the figure the corresponding color image and the calculated spectral clustering map (bottom right) are displayed. As expected, the 440nm image shows superficial blood vessels with high contrast due to the high absorption of oxy-, deoxy-hemoglobin in the vicinity of this band. In the NIR band the blood vessels and the superficial features of the endometrium become transparent, thus allowing for the visualization of underlying features, such as connective tissue (whiter areas).

The clustering map shows, with different pseudocolors, 5 to 6 distinguishable spectral classes. It is clearly seen that their spatial heterogeneity can be identified neither in the raw color nor in the spectral images, which indicates the diagnostic value of this artificial image. The number of the different clusters appearing in the clustering map was determined to be 5 to 6 on the basis of the maximization of the Silhouette index. Going one step further, we have attempted to correlate the "colors" of the particular clusters with endometrial tissue conditions, on the basis of the data collected, thus far (spectral cubes and biopsies). Particularly green hues seem to correspond to normal tissue; blue-purple areas indicate the presence of inflammation, while red shows incipient and white-yellow atypical hyperplasia. Interestingly, figure 36 was selected because it shows that all these conditions are possible to coexist at the same tissue area. It is worth noticing that the system has successfully identified five out of the five cases with biopsy confirmed atypical hyperplasia. Despite these very good initial results, a higher confidence, with regard to the SPECL's diagnostic performance, need to be established. Clinical testing of SPECL endoscope is currently underway for establishing sensitivity-specificity statistics in a sufficient number of clinical trial participants, which have been defined with the aid of calculations of statistical power.

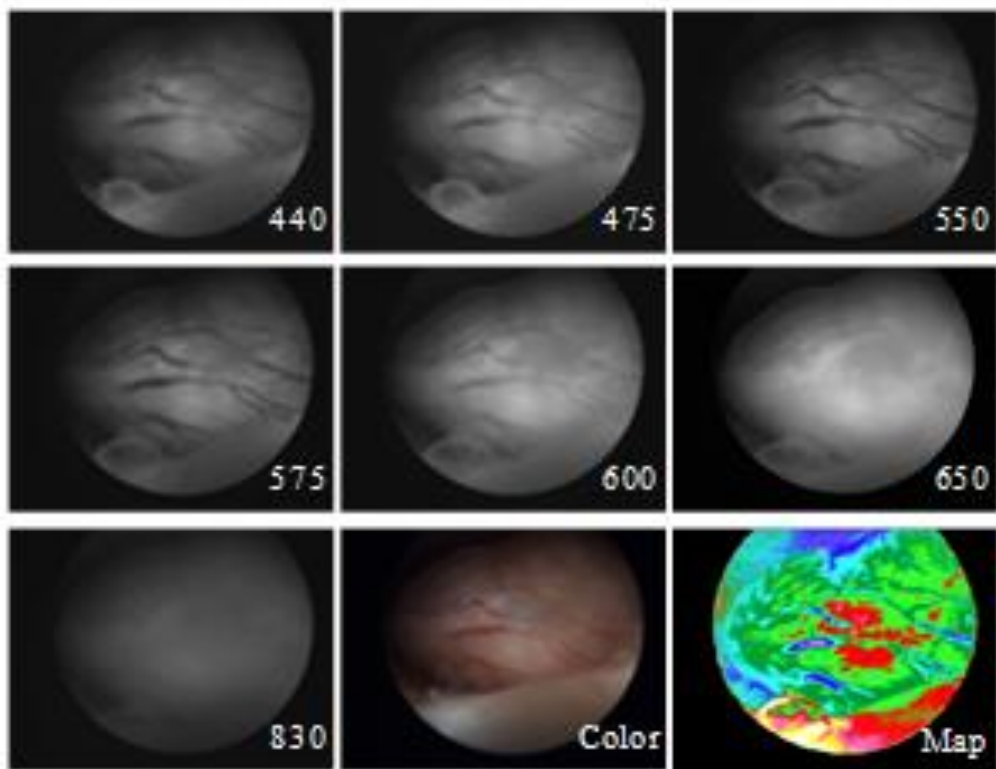


FIGURE 50. SPECTRAL AND COLOR-CODED IMAGES OF THE ENDOMETRIUM. DIFFERENT ARTIFICIAL COLORS CORRESPOND TO DIFFERENT MEDICAL CONDITIONS.

7.2 Identification of endometrial physiology and pathology with the use of multispectral hysteroscopy.

7.2.1 Identification of the menstrual cycle healthy endometrium conditions

Menstrual circle

As it was stated in Chapter 5 (*Endometrial physiology and pathology*), the menstrual cycle is the cycle of changes that occurs in the uterus and ovary for the purpose of sexual reproduction [68-69]. It is essential for the production of eggs and for the preparation of the uterus for pregnancy [68]. The menstrual cycle occurs only in fertile female humans and other female primates.

In humans, the length of a menstrual cycle varies greatly among women (ranging from 25 to 35 days), with 28 days designated as the average length. Each cycle can be divided into three phases based on events in the ovary (ovarian cycle) or in the uterus (uterine cycle) [1]. The ovarian cycle consists of the follicular phase, ovulation, and luteal phase whereas the uterine cycle is divided into menstruation, proliferative phase, and secretory phase. Both cycles are controlled by the endocrine system and the normal hormonal changes that occur can be interfered with using hormonal contraception to prevent reproduction [70].

By convention, menstrual cycles are counted from the first day of menstrual bleeding. Stimulated by gradually increasing amounts of estrogen in the follicular phase, discharges of blood (menses) slow then stop, and the lining of the uterus thickens. Follicles in the ovary begin developing under the influence of a complex interplay of hormones, and after several days one or occasionally two become dominant (non-dominant follicles atrophy and die). Approximately mid-cycle, 24–36 hours after the Luteinizing Hormone (LH) surges, the dominant follicle releases an ovum, or egg, in an event called ovulation. After ovulation, the egg only lives for 24 hours or less without fertilization while the remains of the dominant follicle in the ovary become a corpus luteum; this body has a primary function of producing large amounts of progesterone. Under the influence of progesterone, the endometrium (uterine lining) changes to prepare for potential implantation of an embryo to establish a pregnancy. If implantation does not occur within approximately two weeks, the corpus luteum will involute, causing sharp drops in levels of both progesterone and estrogen. The hormone drop causes the uterus to shed its lining and egg in a process termed menstruation.

In the menstrual cycle, changes occur in the female reproductive system as well as other systems (which lead to breast tenderness or mood changes, for example). A woman's first menstruation is termed menarche, and occurs typically around age 12-13. The end of a woman's reproductive phase is called the menopause, which commonly occurs somewhere between the ages of 45 and 55.

The following figures (37 – 41) show several cases of healthy endometrium hysteroscopic images, along with their pseudocolor map, where each 'color' is correlated to a tissue condition. Results are summed in table 7.

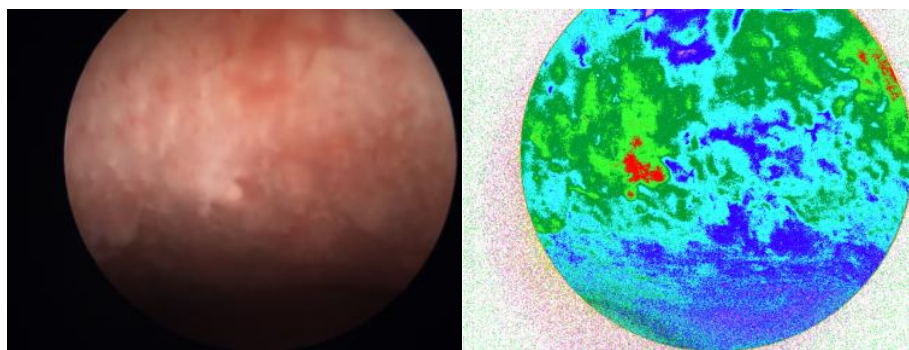


FIGURE 51. EARLY PROLIFERATIVE PHASE. HYSTEROSCOPIC IMAGE (LEFT) AND PSEUDOCOLOR MAP (RIGHT).

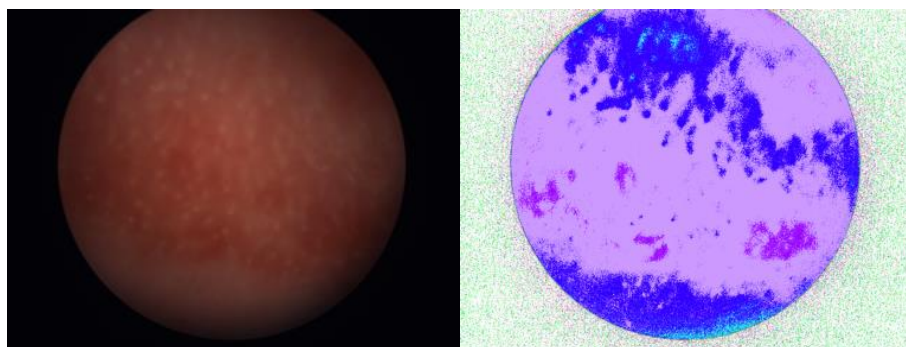


FIGURE 52 . LATE PROLIFERATIVE PHASE. LEFT COLUMN: HYSTEROSCOPIC IMAGE (LEFT) AND PSEUDOCOLOR MAP (RIGHT).

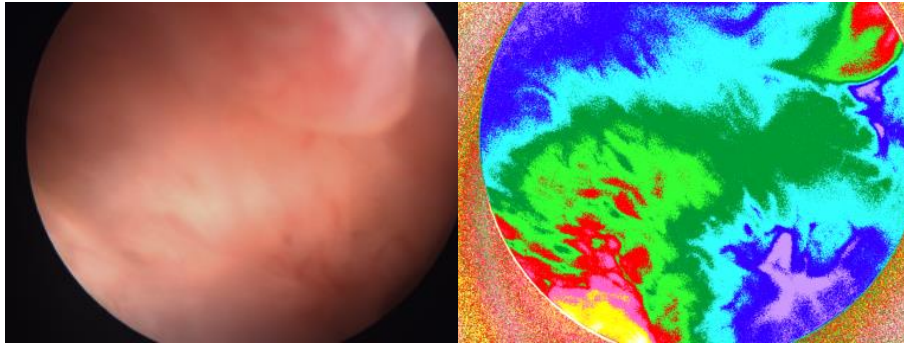


FIGURE 53 . OVULATORY PHASE. LEFT COLUMN HYSTEROSCOPIC IMAGE (LEFT)AND PSEUDOCOLOR MAP (RIGHT).

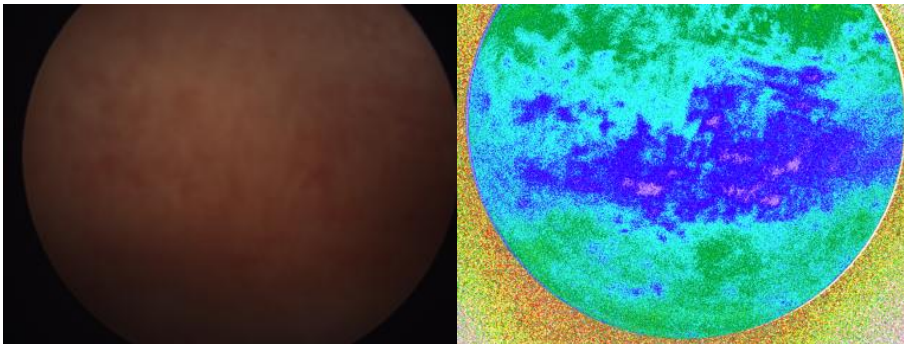


FIGURE 54 . EARLY SECRETORY PHASE. HYSTEROSCOPIC IMAGE (LEFT)AND PSEUDOCOLOR MAP (RIGHT).

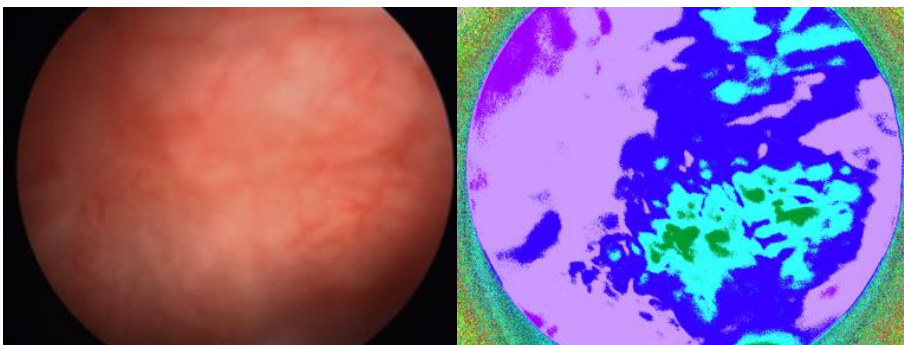


FIGURE 55 . LATE SECRETORY PHASE. HYSTEROSCOPIC IMAGE (LEFT) AND PSEUDOCOLOR MAP (RIGHT).

Phase	Days	Hysteroscopic findings	Corresponding pseudocolor
Early Proliferative	3 – 8	The basal layer is visible, along with the main arteries. Small arterioles appear like speckled spots.	Green
Late Proliferative	9 – 12	Increased size of spiral arterioles.	Green, Purple
Ovulatory	14 – 16	Not identified characteristic hysteroscopic image	Green, Purple, scarce Red spots
Early Secretory	17 – 22	Typical form of the glands, spiral arteries size is increased even more	Purple, Green
Late Secretory	23 - 25	The thickness of the endometrium is increased and spiral arteries are no longer visible	Green, Purple

TABLE 7. IDENTIFICATION OF THE MENSTRUAL CYCLE. COLOR SEQUENCE FOLLOWS DESCENDING ORDER OF COLOR APPEARANCE.

7.2.2 Identification of the AUB conditions, with the use of hyperspectral hysteroscopy

Abnormal uterine bleeding (AUB) refers to not expected uterine bleeding situations. Such abnormal abnormal situations are bleeding between periods, spotting anytime in the menstrual circle, bleeding heavier, for more days than normal or after menopause. Also, menstrual circles that are longer than 35 days, or shorter than 21 days are abnormal. The lack of periods for 3-6 months (amenorrhea) is abnormal too.

AUB may have many causes. These include miscarriage, ectopic pregnancy, adenomyosis, infection of the uterus or the cervix, fibroids, polyps, endometrial hyperplasia, etc. The following figures (42 - 47) show several cases of pathological endometrium hysteroscopic images, along with their pseudocolor map, where each 'color' is correlated to a tissue condition. Results are summed in table 8.

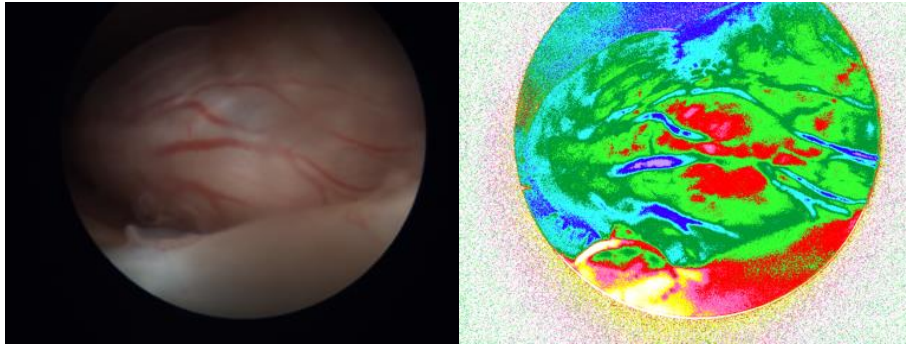


FIGURE 56 . NONFUNCTIONAL ENDOMETRIAL POLYP LOCATED AT THE LEFT SIDE WALL. HYSTEROSCOPIC IMAGE (LEFT) AND PSEUDOCOLOR MAP (RIGHT).

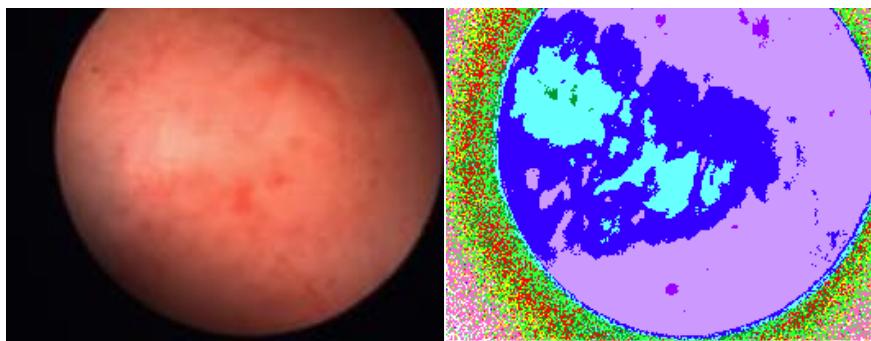


FIGURE 57. FUNCTIONAL ENDOMETRIAL POLYP LOCATED AT THE UTERUS FUNDUS. HYSTEROSCOPIC IMAGE (LEFT)AND PSEUDOCOLOR MAP (RIGHT).

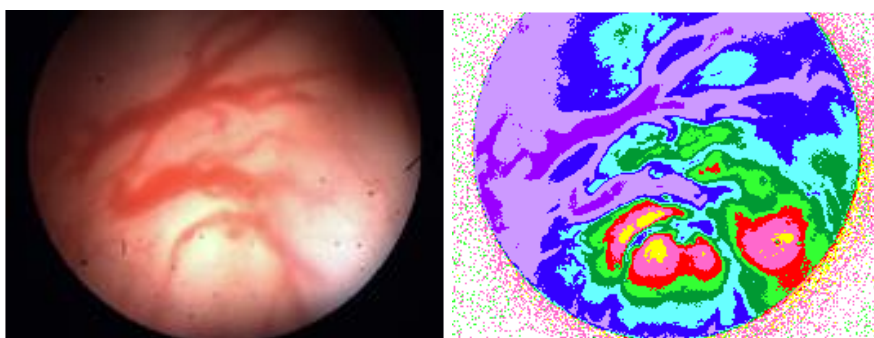


FIGURE 58. SUBMUCOSAL FIBROMYOMA. HYSTEROSCOPIC IMAGE (LEFT)AND PSEUDOCOLOR MAP (RIGHT).

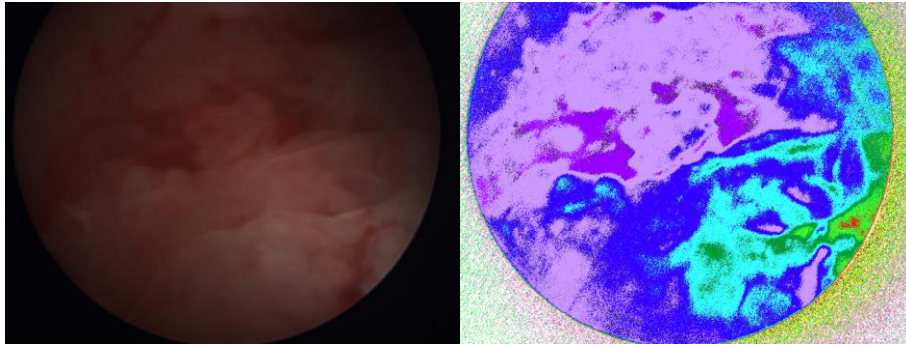


FIGURE 59. ENDOMETRITIS. HYSTEROSCOPIC IMAGE (LEFT) AND PSEUDOCOLOR MAP (RIGHT).

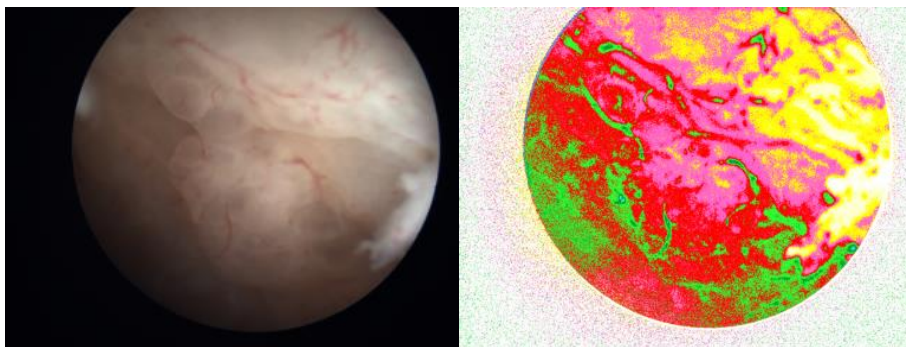


FIGURE 60. COMPLEX ATYPICAL HYPERPLASIA. HYSTEROSCOPIC IMAGE (LEFT) AND PSEUDOCOLOR MAP (RIGHT).

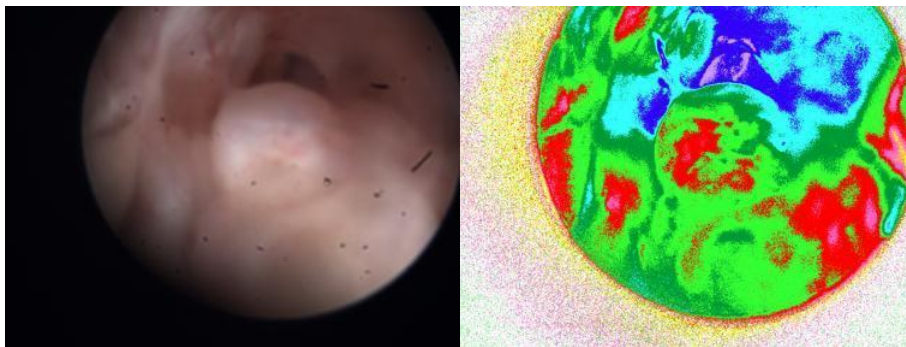


FIGURE 61. ENDOMETRIAL ADENOCARCINOMA. LEFT COLUMN HYSTEROSCOPIC IMAGE (LEFT) AND PSEUDOCOLOR MAP (RIGHT).

AUB	Hysteroscopic findings	Corresponding pseudocolor
Nonfunctional endometrial polyp	Endometrial eminences	Yellow, Red
Functional endometrial polyp	Endometrial eminences	Purple Green
Submucosal fibromyoma	The surface of the fibroids is whitish and crossed by one or more vessels	Red, Yellow
Endometritis	Increased vascularization, mikropolypodiasis, swelling and thickening of the endometrium	Purple, Blue
Complex atypical hyperplasia	Polypoid formations, areas of necrosis and non-uniform presence of glandular orifices	Red, Yellow
Endometrial adenocarcinoma	Cystic glandular formations coexisting or not with cystic atrophy	Variety of colors

TABLE 8. IDENTIFICATION OF THE ENDOMETRIAL PATHOLOGY WITH CORRELATED CLUSTERING PSEUDOCOLORS

ENDOMETRIAL TISSUE CONDITION	CORRELATED PSEUDOCOLOR
FUNCTIONAL ENDOMETRIUM	Green
INFLAMMATION	Blue, Purple
HYPERPLASIA	Red
FIBROSIS	Yellow

TABLE 9. PSEUDOCOLORS CORRELATED WITH PARTICULAR ENDOMETRIAL TISSUE CONDITIONS

Conclusions

A novel spectral clustering endoscope was described and it was identified that in the case of the endometrium there are 5 to 6 distinguishable clusters of spectra. Preliminary clinical validation, currently in progress, shows that the identified clusters of spectra correlate well with tissue pathology. This new technology is therefore of high potential; to provide in vivo, early detection, and grading of the lesion, to minimize the need for biopsies, to offer objective follow up, to guide and to evaluate treatments.

Discussion

A novel snapshot spectral clustering endoscope was developed and it has been identified that in the case of the endometrium there are 5 to 6 distinguishable clusters of spectra. Preliminary clinical validation, currently in progress, shows that the identified clusters of spectra correlate well with tissue pathology. This new technology is therefore of high potential; to provide in vivo, early detection, and grading of the lesion, to minimize the need for biopsies, to offer objective follow up, to guide and to evaluate treatments.

This project aims at developing the next generation of spectral imaging devices, incorporating novel optoelectronic hardware for enabling the instantaneous acquisition of spectral images and innovative software solutions for calculating/displaying spectral clustering maps (thematic maps) in (nearly) real-time, related to endometrial pathology. To the best of our knowledge such an efficient and integrated solution has not been reported so far. This development is expected to open new horizons in spectral imaging applications since: a) it will expand the applications of spectral imaging to dynamically changing phenomena and targets; b) it will enable the clinical implementation of spectral imaging to a variety of biomedical applications, where the shortening of the examination time and objectivity is crucial. Besides the expected innovations at the system's level, several particular innovations related with the system's components are expected to enrich the outcomes of this project, including: a) methods and apparatus for separating images on the basis of their spectral components; b)

Computing platforms for (real-time) processing of spectral cube data based on novel algorithms and data steaming methods.

Despite these very good initial results, a higher confidence, with regard to the snapshot spectral hysteroscope diagnostic performance, need to be established. Clinical testing of SPECL endoscope is currently underway for establishing sensitivity-specificity statistics in a sufficient number of clinical trial participants, which have been defined with the aid of calculations of statistical power.

References

- [1]. George, C.T., Basiji, D.A., Hall, B.E. et al. 2004. Distinguishing Modes of Cell Death Using the ImageStream Multispectral Imaging Flow Cytometer. *Cytometry* 59A: 237–45
- [2]. Chi, W., George, N. 2009. Phase-coded aperture for optical imaging. *Optics Communications* 282:2110-7
- [3]. S.Svanberg, *Atomic and molecular spectroscopy – Basic aspects and practical applications*, (Springer Verlag, Heidelberg, 2004).
- [4]. P.W.Atkins, *Physical chemistry*, (Oxford University Press, Oxford, 1982).
- [5]. I.Wang, *Photodynamic therapy and laser-based diagnostic studies of malignant tumours*, Dissertation thesis, Lund University, Lund, Sweden (1999).
- [6]. J.Mobley and T.Vo-Dinh, *Optical properties of tissue*, in *biomedical photonics handbook*, ed. T.Vo-Dinh, pp. 2-1-2-74 (CRC Press, Boca Raton, 2005).
- [7]. S.L.Jacques and S.A.Prahl. *Optical properties*, [Http://omlc.ogi.edu](http://omlc.ogi.edu), (1998).
- [8]. S.L.Jacques, *Reflectance spectroscopy with optical fiber devices, and transcutaneous bilirubinometers*, in *biomedical optical instrumentation and laser-assisted biotechnology*, eds. A.M.Verga Scheggi, S.Martellucci, A.N.Chester and R.Pratesi, pp. 83-94 (Kluwer Academic Publishers, Dordrecht, 1996).
- [9]. J.R.Mourant, J.P.Freyer, A.H.Hielscher, A.A.Eick, D.Shen and T.M.Johnson, *Mechanisms of light scattering from biological cells relevant to noninvasive optical-tissue diagnostics*, *Appl. Opt.* 37, 3586-3593 (1998).
- [10]. S.Jacques, *Origins of tissue optical properties in the UVA, visible, and NIR Regions*, *OSA TOPS on Advances in Optical Imaging and Photon Migration*, vol. 2, 364-369 (1996).
- [11]. N.Kollias, G.Zonios and G.N.Stamatas, *Fluorescence spectroscopy of skin*, *Vibrational Spectroscopy* 28, 17-23 (2002).
- [12]. A.Mahadevan, M.F.Mitchell, E.Silva, S.Thomsen and R.Richards-Kortum, *Study of the fluorescence properties of normal and neoplastic human cervical tissue*, *Lasers Surg. Med.* 13, 647-655 (1993).
- [13]. J.Lu, C.Lau, M.Morizono, K.Ohta and M.Kai, *A chemiluminescence reaction between hydrogen peroxid and acetonitrile and its applications*, *Anal. Chem.* 73, 5979-5983 (2001).
- [14]. M.Soto Thompson, T.Johansson, S.Pålsson, S.Andersson-Engels, S.Svanberg, N.Bendsoe, U.Stenram, K.Svanberg, J.Spigulis, A.Derjabo and J.Kapostins, *Photodynamic therapy of basal cell carcinoma with multi-fibre contact light delivery*, *J. Env. Path. Tox. Onc.* 25, (2005).
- [15]. R.Rydell, C.Eker, S.Andersson-Engels, P.Wahlberg and K.Svanberg, *Fluorescence investigations to identify laryngeal lesions in vivo*, *Manuscript in preparation for Head and Neck* (2002).
- [16]. J.H.Knox and B.Kauer, *High Performance Liquid Chromatography*, eds. P.R.Brown and R.A.Hartwick, (Wiley Interscience: New York, 1989).

- [17]. S.Andersson-Engels, J.Johansson, K.Svanberg and S.Svanberg, Fluorescence diagnosis and photochemical treatment of diseased tissue using lasers: Part II, *Anal. Chem.* 62, 19-27 (1990).
- [18]. J.-L.Boulnois, Photophysical processes in recent medical laser developments: a review, *Lasers Med. Sci.* 1, 47-66 (1986).
- [19]. Gray's Anatomy for Students, 2nd edition
- [20]. Blue Histology - Female Reproductive System. School of Anatomy and Human Biology - The University of Western Australia
<http://www.lab.anhb.uwa.edu.au/mb140/CorePages/FemaleRepro/FemaleRepro.htm> Accessed 20061228 20:35.
- [21]. Arias-Stella, J. (Jan 2002). "The Arias-Stella reaction: facts and fancies four decades after. *Adv Anat Pathol* 9 (1): 12–23. PMID 11756756.
- [22]. "adenomyosis" at Dorland's Medical Dictionary
- [23]. Katz VL (2007). *Comprehensive gynecology* (5th ed.). Philadelphia PA: Mosby Elsevier.
- [24]. "endometritis" at Dorland's Medical Dictionary
- [25]. Rubert Guedj; Baggish, Michael S.; Valle, Rafael Heliodoro (2007). *Hysteroscopy: visual perspectives of uterine anatomy, physiology, and pathology*. Hagerstown, MD: Lippincott Williams & Wilkins. p. 488. ISBN 0-7817-5532-8.
- [26]. Batt, Ronald E. (2011). *A history of endometriosis*. London: Springer. pp. 13–38. ISBN 978-0-85729-585-9.
- [27]. Bulletti C, Coccia ME, Battistoni S, Borini A (August 2010). "Endometriosis and infertility". *J. Assist. Reprod. Genet.* 27 (8): 441–7. doi:10.1007/s10815-010-9436-1. PMC 2941592. PMID 20574791.
- [28]. Culley, L.; Law, C.; Hudson, N.; Denny, E.; Mitchell, H.; Baumgarten, M.; Raine-Fenning, N. (2013). "The social and psychological impact of endometriosis on women's lives: A critical narrative review". *Human Reproduction Update* 19 (6): 625–639. doi:10.1093/humupd/dmt027. PMID 23884896.
- [29]. "Endometriosis fact sheet". NIH. Retrieved Feb. 12, 2013.
- [30]. "Uterine leiomyoma" at Dorland's Medical Dictionary
- [31]. Neiger, R.; Sonek, J.; Croom, C.; Ventolini, G. (2006). "Pregnancy-related changes in the size of uterine leiomyomas". *The Journal of reproductive medicine* 51 (9): 671–674. PMID 17039693.
- [32]. Wallach EE, Vlahos NF (August 2004). "Uterine myomas: an overview of development, clinical features, and management". *Obstet Gynecol* 104 (2): 393–406. doi:10.1097/01.AOG.0000136079.62513.39. PMID 15292018.
- [33]. Richard Cote, Saul Suster, Lawrence Weiss, Noel Weidner (Editor) (2002). *Modern Surgical Pathology* (2 Volume Set). London: W B Saunders. ISBN 0-7216-7253-1.
- [34] Nicolaije K.A. et al. Follow-up practice in endometrial cancer and the association with patient and hospital characteristics: A study from the population-based PROFILES registry, *Gynecologic Oncology*, 129 (2), May 2013, page 324–331, PMID 23435365.
- [35] Oldenburg C.S. et al. The relationship of body mass index with quality of life among endometrial cancer survivors: a study from the population-based PROFILES registry. *Gynecologic Oncology*, 129 (1), April 2013, page 216–21, PMID 23296262.
- [36] Hoffman, Barbara L. (2012). *Williams Gynecology: Chapter 33, Endometrial Cancer* (2nd ed.). New York: McGraw-Hill Medical. ISBN 978-0071716727.

- [37] Schorge, John O. et al (2008). *Williams Gynecology*. New York: McGraw-Hill Medical. ISBN 9780071472579.
- [38] Palter S (2005). "High Rates of Endometriosis in Patients with Intrauterine Synechiae (Asherman's Syndrome)". *Fertility and Sterility* 86 (null): S471–S471.
- [39] Jane A. Bates (1997). *Practical Gynaecological Ultrasound*. Cambridge, UK: Cambridge University Press. ISBN 1-900151-51-0.
- [40] "Uterine polyps". *MayoClinic.com*. 2006-04-27.
- [41] Sternberg, Stephen S.; Stacey E. Mills, Darryl Carter (2004). *Sternberg's Diagnostic Surgical Pathology*. Lippincott Williams & Wilkins. p. 2460. ISBN 0-7817-4051-7.
- [42] Dysmenorrhea: Menstrual abnormalities at Merck Manual of Diagnosis and Therapy Professional Edition
- [43] "Endometrial Polyp". *GPnotebook*. Retrieved 2007-10-20.
- [44] DeCherney, Alan H.; Lauren Nathan (2003). *Current Obstetric & Gynecologic Diagnosis & Treatment*. McGraw-Hill Professional. p. 703. ISBN 0-8385-1401-4.
45. Debra L. Berridge, MD, Thomas C. Winter, MD, Saline Infusion Sonohysterography, Technique, Indications, and Imaging Findings, *J Ultrasound Med* 23:97–112, 2004
- [46] <http://www.ultrasound-images.com/carcinoma.htm>
- [47] Brian D. Sydow, MD, and Evan S. Seigelman, MD, Uterine MRI: A review of technique and diagnosis, October 2008, *Applied Radiology*
48. Eisen GM, Kim CY, Fleischer DE, et al. High-resolution chromoendoscopy for classifying colonic polyps: a multicenter study. *Gastrointest Endosc* 2002;55:687-94
- [49] C. Balas "Review of biomedical optical imaging—a powerful, non-invasive, non-ionizing technology for improving in vivo diagnosis," *Meas. Sci. Technol. IoP*, vol. 20, no. 10, 2009
- [50] C. Balas, G. Epitropou and C. Pappas: "Multi/Hyper-Spectral Imaging," in *Handbook of Biomedical Optics*, Taylor&Francis Books, Inc, USA, 2011
- [51] K. Kuznetsov, R. Lambert and J. F. Rey, "Narrow-band imaging: potential and limitations," *Endoscopy*, vol. 38, pp. 76-81, 2006.
- [52] I. K. Gono "Multifunctional Endoscopic Imaging System for Support of Early Cancer Diagnosis" *IEEE Journal of Selected Topics in Quantum Electronics*, vol. 14, no. 1, pp 62-69, 2008
- [53] L. M. Song, et al., "Narrow band imaging and multiband imaging," *Gastrointestinal Endoscopy*, vol. 67, no. 4, pp. 581, 2008.
- [54] C. Farquhar, A. Ekeroma, S. Furness and B. Arroll, "A systematic review of transvaginal ultrasonography, sonohysterography and hysteroscopy for the investigation of abnormal uterine bleeding in premenopausal women," *Acta Obstetrica et Gynecologica Scandinavica*, vol. 82, no. 6, pp. 493-504, 2003.
- [55] T. J. Clark, et al., "Accuracy of hysteroscopy in the diagnosis of endometrial cancer and hyperplasia," *JAMA: The Journal of the American Medical Association*, vol. 288, no. 13, pp. 1610-1621, 2002.
- [56] I. Kisu, et al., "Narrow band imaging hysteroscopy: a comparative study using randomized video images," *International Journal of Oncology*, vol 39, no. 5, pp. 1057-1062, 2011.

- [57] Tordoff, B; Murray, DW. "Guided sampling and consensus for motion estimation." European Conference in Computer Vision, 2002
- [58] D. Mattes, D.R. Haynor, H. Vesselle, T. Lewellen, and W. Eubank. "Non-rigid multimodality image registration." (Proceedings paper). Medical Imaging 2001: Image Processing. SPIE Publications, 3 July 2001. pp. 1609–1620
- [59] [1-14] references from Erturk, A. and Erturk, S., "Unsupervised Segmentation of Hyperspectral Images Using Modified Phase Correlation," IEEE Geosciences and Remote Sensing Letters Papers 3(4), 527-531 (2006).
- [60] Keshava, N., "Distance metrics and band selection in hyperspectral processing with applications to material identification and spectral libraries," Geoscience and Remote Sensing, IEEE Transactions on , vol.42, no.7, pp. 1552- 1565, July 2004
- [61] Arthur, D. and Vassilvitskii, S. (2007). "k-means++: the advantages of careful seeding". Proceedings of the eighteenth annual ACM-SIAM symposium on Discrete algorithms. pp. 1027–1035
- [62] A. K. Jain, R. Dubes. Algorithms for clustering data. Prentice-Hall. 1988
- [63] J. Han, M. Kamber. Data Mining: Concepts and Techniques. Morgan Kaufmann. 2006
- [64] L. Kaufman, P. Rousseeuw. Finding Groups in Data: An Introduction to Cluster Analysis. Wiley. 1990.
- [65] A. Ben-Hur, A. Elisseeff, I. Guyon. A stability based method for discovering structure in clustered data. In Aetman, R.B. (Ed.), et al. Pacific Symposium on Biocomputing. New Jersey World Scientific Publishing Co. 2002.
- [66] T. Lange, V. Roth, M. Braun. Stability-based validation of clustering solutions. Neural Computation. 16:1299–1323. 2004
- [67] Van den Boomgard, R, and R. van Balen, "Methods for Fast Morphological Image Transforms Using Bitmapped Images," Computer Vision, Graphics, and Image Processing: Graphical Models and Image Processing, Vol. 54, Number 3, pp. 254-258, May 1992.
- [68] Silverthorn, Dee Unglaub (2013). Human Physiology: An Integrated Approach (6th ed.). Glenview, IL: Pearson Education, Inc. pp. 850–890. ISBN 0-321-75007-1.
- [69] Sherwood, Laurelee (2013). Human Physiology: From Cells to Systems (8th ed.). Belmont, CA: Cengage. pp. 735–794. ISBN 1-111-57743-9.
- [70] Klump KL, Keel PK, Racine SE, et al. (February 2013). "The interactive effects of estrogen and progesterone on changes in emotional eating across the menstrual cycle". J Abnorm Psychol 122 (1): 131–7. doi:10.1037/a0029524. PMID 22889242.
- [71] Kobus Barnard, Brian Funt. "Camera Characterization for Color Research". COLOR research and application, Volume 27, Number 3, June 2002.